



January 2019

Predicting Flame Stability, Ash Deposition And Radiative Heat Transfer Characteristics During Oxy-Fuel Combustion Of Pulverized Coal Using Different Multiphase Modeling Frameworks

Trevor Lee Seidel

[How does access to this work benefit you? Let us know!](#)

Follow this and additional works at: <https://commons.und.edu/theses>

Recommended Citation

Seidel, Trevor Lee, "Predicting Flame Stability, Ash Deposition And Radiative Heat Transfer Characteristics During Oxy-Fuel Combustion Of Pulverized Coal Using Different Multiphase Modeling Frameworks" (2019). *Theses and Dissertations*. 2585.
<https://commons.und.edu/theses/2585>

This Thesis is brought to you for free and open access by the Theses, Dissertations, and Senior Projects at UND Scholarly Commons. It has been accepted for inclusion in Theses and Dissertations by an authorized administrator of UND Scholarly Commons. For more information, please contact und.common@library.und.edu.

PREDICTING FLAME STABILITY, ASH DEPOSITION AND RADIATIVE HEAT
TRANSFER CHARACTERISTICS DURING OXY-FUEL COMBUSTION OF PULVERIZED
COAL USING DIFFERENT MULTIPHASE MODELING FRAMEWORKS

by

Trevor Lee Seidel

Bachelor of Science, University of North Dakota, 2017

A Thesis

Submitted to the Graduate Faculty

of the

University of North Dakota

In partial fulfillment of the requirements

For the degree of

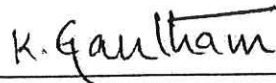
Master of Science

Grand Forks, North Dakota

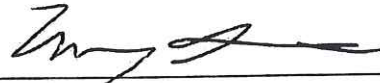
August
2019

Copyright © 2019 Trevor Lee Seidel

This thesis, submitted by Trevor Seidel in partial fulfillment of the requirements for the Degree of Master of Science from the University of North Dakota, has been read by the Faculty Advisory Committee under whom the work has been done and is hereby approved.



Dr. Gautham Krishnamoorthy, Chairperson



Dr. Wayne Seames, Co-Chairperson



Dr. Michael Mann

This thesis is being submitted by the appointed advisory committee as having met all of the requirements of the School of Graduate Studies at the University of North Dakota and is hereby approved.



Chris Nelson
Associate Dean of the School of Graduate Studies



Date

PERMISSION

Title: Predicting Flame Stability, Ash Deposition, and Boiler Chamber Radiation using Computational Fluid Dynamic (CFD) Modeling during Oxy-fuel combustion of Pulverized Coal.

Department: Chemical Engineering

Degree: Master of Science

In presenting this thesis in partial fulfillment of the requirements for a graduate degree from the University of North Dakota, I agree that the library of this University shall make it freely available for inspection. I further agree that permission for extensive copying for scholarly purposes may be granted by the professor who supervised my thesis work, or in his absence, by the Chairperson of the department or the dean of the School of Graduate Studies. It is understood that any copying or publication or other use of this thesis or part thereof for financial gain shall not be allowed without my written permission. It is also understood that due recognition shall be given to me and the University of North Dakota in any scholarly use which may be made of any material in my thesis.

Trevor Lee Seidel

August 2019

TABLE OF CONTENTS

LIST OF FIGURES	vii
LIST OF TABLES	x
NOMENCLATURE	xi
ACKNOWLEDGEMENTS	xvi
ABSTRACT	xviii
CHAPTER 1 – INTRODUCTION	1
1.1. Motivation	1
1.2. Objectives	2
1.3. Thesis Outline.....	3
CHAPTER 2 – ASH DEPOSITION: MECHANISMS AND IMPACTS	4
2.1. Ash Deposition in Coal and Coal/Biomass Systems	4
2.1.1 Ash Particle Formation.....	4
2.1.2 Ash Particle Transport.....	8
2.1.3 Ash Particle Stickiness.....	10
2.2. Ash Deposition Modeling.....	11
2.3. Particle Size Distribution Impact on Radiative Heat Transfer	17
2.3.1 Radiation Modeling.....	20
CHAPTER 3 – BACKGROUND: MULTIPHASE MODELING FRAMEWORKS	23
3.1. Dispersed, Multiphase Flows	23
3.1.1 Lagrangian Tracking	23
3.1.1.1 Overview.....	23
3.1.1.2 Conservation of Mass for Continuous Phase	24
3.1.1.3 Conservation of Momentum for Continuous Phase	24
3.1.1.4 Conservation of Species Mass for Continuous Phase	25
3.1.1.5 Conservation of Energy for Continuous Phase.....	25
3.1.1.6 Governing Equations for Discrete Phase.....	26
3.1.1.7 Advantages/Disadvantages of Lagrangian Tracking	27

3.1.2	<i>Two-Fluid Model</i>	28
3.1.2.1	<i>Overview</i>	28
3.1.2.2	<i>Conservation of Mass</i>	28
3.1.2.3	<i>Conservation of Momentum</i>	29
3.1.2.4	<i>Conservation of Energy</i>	29
3.1.2.5	<i>Drag Law</i>	29
3.1.2.6	<i>Advantages/Disadvantages of Two-Fluid Model</i>	30
CHAPTER 4 – NON-SWIRLING OXY-COAL FLAMES	31
4.1.	Problem Overview and Methods	31
4.2.	Results	39
4.2.1.	<i>Inert Particle Simulations</i>	39
4.2.2.	<i>Flame Stand-off Predictions Using DPM Framework</i>	41
4.2.3.	<i>Flame Stand-off Predictions Using TFM Framework</i>	44
4.2.4.	<i>Influence of Other Operational Parameters on Flame Stand-off</i>	47
4.2.5.	<i>A Closer Examination of TFM and DPM Predictions</i>	49
CHAPTER 5 – SWIRLING OXY-COAL FLAMES	58
5.1.	Problem Overview and Methods	58
5.2.	Results	65
5.2.1.	<i>Particle Dispersion Differences</i>	65
5.2.2.	<i>Temperature and Velocity Profile Comparison</i>	66
5.2.3.	<i>Summary of Measured and Predicated Boiler Variables</i>	71
5.2.4.	<i>Radiative Characteristics</i>	72
CHAPTER 6 - SUMMARY	75
6.1.	Conclusions	75
6.1.1	<i>2D, Non-Swirling Oxy-Coal Flame Stand-off Study</i>	75
6.1.2	<i>2D, Swirling Oxy-Coal Flame Study</i>	76
6.2.	Future Work.....	77
REFERENCES	79

LIST OF FIGURES

Figure		Page
2.1	Inorganic constituents in the coal matrix and their occurrence [4].....	5
2.2	Major physical transformations of ash components during combustion [14].....	7
2.3	Ash deposition mechanisms on a superheater tube [4].....	9
4.1	Utah’s experimental oxy-fuel combustor (OFC).....	34
4.2	2D, axisymmetric geometry designed to replicate Utah’s experimental OFC.....	35
4.3	Simulated wall temperature profile in the furnace in the non-swirling study.....	35
4.4	Coal particle size distributions and Rosin-Rammler curve fit for parent coal particles in the non-swirling study.....	36
4.5	Particle volume fractions in the inert simulations of 85-micron particles using DPM and TFM modeling frameworks.....	39
4.6	Axial temperature profiles in the non-swirling inert particle simulations: (a) Particle temperature; (b) Gas temperature; (c) Temperature difference (Gas temperature – Particle temperature).....	40
4.7	Axial velocity profiles in the non-swirling inert particle simulations: (a) Particle velocity; (b) Velocity difference (Gas velocity – Particle velocity).....	41
4.8	Carbon monoxide mole fraction (a) and char burnout (b) in the Rosin-Rammler DPM simulations for the non-swirling study. Mean experimentally measured stand-off distance locations indicated by vertical line.....	42
4.9	Carbon monoxide mole fraction (a) and char burnout (b) in the 35-micron DPM simulations for the non-swirling study. Mean experimentally measured stand-off distance locations indicated by vertical line	43

4.10	Carbon monoxide mole fraction (a) and char oxidation rate (kmol/m ³ -s) (b) in the 85-micron TFM simulations for the non-swirling study. Mean experimentally measured stand-off distance locations indicated by vertical line.....	44
4.11	Carbon monoxide mole fraction (a), char oxidation rate (kmol/m ³ -s) for 0% O ₂ scenario (b) and char oxidation rate (kmol/m ³ -s) for 20.9% O ₂ scenario (c) in 2-phase TFM simulations for the non-swirling study. Mean experimentally measured stand-off distance locations indicated by vertical line.....	46
4.12	(a) Devolatilization rate (kmol/m ³ -s) and (b) Char oxidation rate (kmol/m ³ -s) along the centerline axis during simulations of the 14.4% O ₂ flames (under different operating conditions) simulated using the TFM framework.	48
4.13	The fraction of total flux attributed to radiative heat transfer in the oxy-coal flames (a) with gas radiation and (b) without gas radiation for the non-swirling study.....	50
4.14	Contours of gas temperature (in K) in the non-swirling oxy-coal flames: (a) DPM framework; (b) TFM framework.....	51
4.15	Contours of particle volume fractions in the non-swirling oxy-coal flames: (a) DPM framework; (b) TFM framework.....	52
4.16	Contours of turbulence variables in the 20.9% O ₂ non-swirling oxy-coal flames: (a) Turbulent kinetic energy (m ² /s ²); (b) Turbulent dissipation rate (m ² /s ³).....	53
4.17	Contours near the flame recirculation zone in the non-swirling oxy-coal flames: (a) Gas temperature (The colors/regions corresponding to 1200 K – 1300 K indicated by arrows for brevity); (b) Oxygen mole fractions.....	55
4.18	The fraction of total flux attributed to radiative heat transfer in the oxy-coal flames in Rosin-Rammler DPM simulations in the 0% O ₂ scenario for the non-swirling study.....	56
4.19	The fraction of total flux attributed to radiative heat transfer in the oxy-coal flames in 2-phase TFM simulations in the 0% O ₂ scenario for the non-swirling study.....	57
5.1	Utah’s experimental oxy-fuel combustor (OFC).....	59
5.2	2D, axisymmetric geometry designed to replicate Utah’s experimental OFC.....	60
5.3	Simulated wall temperature profile in the furnace in the swirling study.....	61
5.4	Particle size distributions and Rosin-Rammler curve fit for the SUFCO sub-bituminous coal in the swirling study.....	65

5.5	Particle distribution in the DPM simulations for the swirling study.....	66
5.6	Particle distribution in the TFM simulations for the swirling study.....	66
5.7	Contours of temperature in the DPM and TFM frameworks in the (a) Oxy27 and (b) Oxy70 scenarios for the swirling study. Arrows indicate peak combustion temperatures.....	67
5.8	Experimental Data, DPM, and TFM axial temperature profiles in the (a) Oxy27 and (b) Oxy70 scenarios for the swirling study.....	68
5.9	Contours of gas velocity in the DPM and TFM frameworks in the (a) Oxy27 and (b) Oxy70 scenarios for the swirling study.....	69
5.10	Experimental Data, DPM, and TFM axial velocity profiles in the (a) Oxy27 and (b) Oxy70 scenarios for the swirling study.....	70
5.11	The fraction of total flux attributed to radiative heat transfer in the oxy-coal flames for the Oxy27 (a) and the Oxy70 (b) DPM simulations for the swirling study.....	73
5.12	The fraction of total flux attributed to radiative heat transfer in the oxy-coal flames for the Oxy27 (a) and the Oxy70 (b) TFM simulations for the swirling study.....	74

LIST OF TABLES

Tables	Page
2.1	CFD-based predictions of ash deposition in boilers [29]..... 12
2.2	Radiation models utilized in oxy-fuel combustion CFD modeling work..... 18
2.3	Coal radiative property variations utilized in this thesis [51]..... 22
4.1	Proximate and ultimate analysis of Utah Bituminous coal..... 35
4.2	Primary and secondary oxidizer stream specifications for both non-swirling combustion scenarios..... 37
4.3	A summary of reaction and kinetic parameters modeled in the non-swirling study..... 38
4.4	A summary of modeling options invoked in the non-swirling study..... 38
5.1	Proximate and ultimate analysis of SUFCO coal..... 61
5.2	CCSEM and ash chemistry analysis of SUFCO coal..... 61
5.3	Primary and secondary oxidizer stream specifications for both swirling combustion scenarios..... 62
5.4	A summary of reaction and kinetic parameters modeled in the swirling study..... 63
5.5	A summary of modeling options invoked in the swirling study..... 64
5.6	A summary of measured and predicted environmental and ash variables in the Oxy27 scenario for the swirling study..... 71
5.7	A summary of measured and predicted environmental and ash variables in the Oxy70 scenario for the swirling study..... 72

NOMENCLATURE

A	surface area
A_1	pre-exponential factor
c_p	specific heat
C	Carbon content of particle
d, D	diameter, m
E	activation energy
f_{pn}	scattering factor
\vec{F}	external body force vector
g, \bar{g}	gravitational force, m/s^2
\vec{g}	gravitational force vector
G	incident radiation, W/m^2
h	specific enthalpy
I	radiative intensity, $W/m^2 \cdot Sr$
I_b	black body emissive power
\bar{J}	diffusive flux
k	thermal conductivity
k_a	absorption coefficient, m^{-1}
k_{eff}	effective conductivity
k_t	turbulent thermal conductivity
K_{th}	thermophoretic coefficient

m	mass, kg
\dot{m}_{ab}	mass transfer between the a th phase and the b th (where a and b can be any phase subscript)
OFS	oxygen-to-fuel stoichiometry
p, P	pressure
PCT	peak combustion temperature
q	incident radiative flux, W/m ²
Q_{abs}	absorption efficiencies
Q_{scat}	scattering efficiencies
R	net rate of production
Re	Reynolds number
R_g	universal gas constant
S	volumetric source term
S_e	volumetric heat source term
S_h	volumetric source term that includes heat of chemical reaction
S_m	volumetric source term to represent mass addition
STP	standard temperature and pressure
t	time, s
T	temperature, K
T_{ref}	reference temperature, K
T_{∞}	temperature of bulk fluid
TEs	trace elements
u, \bar{u}	velocity, m/s
ν	kinematic viscosity

\vec{v}	velocity vector
\vec{v}_{dr}	drift velocity vector
V	volume, m ³
We	Weber number
x, r, θ	cylindrical coordinate system
Y	moles

Greek Symbols

α	volume fraction
ε	emissivity
θ	radiation temperature
λ	bulk viscosity
μ	viscosity
ρ	density, kg/m ³
σ	scattering coefficient, m ⁻¹
σ_{SB}	Stefan-Boltzmann constant ($5.67 \cdot 10^{-8}$ W/m ² ·K ⁴)
σ_{sp}	particle surface tension when solid particle is molten or wall is wet
$\vec{\tau}$	stress tensor vector
Φ	scattering phase function
ψ	correction factor for particles that disobey Stokes' law

Subscripts

c	denotes tube
g	denotes gas
i, j	denotes arbitrary species

k, l, q denotes phase
 ℓ denotes liquid
 m denotes mixture
 o denotes initial value
 p denotes particle
 s denotes solid
 v denotes vapor
 x, r, θ denotes cylindrical coordinate system

Elements and Compounds

Al aluminum
 Al_2O_3 aluminum oxide
 C elemental carbon
 Ca calcium
 CaO calcium oxide
 Cl chloride
 CO carbon monoxide
 CO_2 carbon dioxide
 Fe iron
 Fe_2O_3 ferric oxide
 H elemental hydrogen
 H_2O water
 K potassium
 K_2O potassium oxide

Mg magnesium
MgO magnesium oxide
Mn manganese
MnO manganese oxide
N elemental nitrogen
N₂ nitrogen
Na sodium
Na₂O sodium oxide
NO_x nitrous oxides (where *x* can range from 1-3)
O elemental oxygen
O₂ oxygen
P phosphorous
P₂O₅ phosphorus pentoxide
S elemental sulfur
Si silicon
SiO₂ silicon dioxide
SO₂ sulfur dioxide
SO₃ sulfur trioxide
Ti titanium
TiO₂ titanium dioxide
Zn zinc

ACKNOWLEDGEMENTS

I would first like to express my deepest appreciation to my graduate academic advisor for the past three years, Dr. Gautham Krishnamoorthy. Dr. Krishnamoorthy was the first to encourage me to do the combined BS/MS degree program. Throughout the combined degree program, he has shared with me invaluable insight into the research process, practical suggestions on how to better my research, and extensive knowledge in the topic areas of this thesis. Over the last three years, he has become a very much appreciated mentor, both for personal and career decisions, and I will ever be indebted to him for that.

I would also like to extend sincere thanks to co-chair committee member Dr. Wayne Seames. Throughout both my undergraduate and graduate experiences at UND, he has provided me with constructive criticism, extensive knowledge in a variety of topics, and many enjoyable research opportunities. He has been helpful in reviewing my thesis, setting up my defense date, and offering any advice.

I would also like to extend sincere thanks to my undergraduate academic advisor and committee member Dr. Michael Mann. He has provided much appreciated career guidance and has been helpful in reviewing my thesis, setting up my defense date, and offering any advice.

I would also like to express my gratitude to my fellow undergraduate and graduate students at UND, as well as the remaining Chemical Engineering department faculty. Not only have I learnt a great deal from them, but many have provided insightful suggestions and constructive advice to both my education and career.

This work was funded by the National Science Foundation (Grant Number: 1603249). Any opinions, findings, and conclusions or recommendations expressed in this material are those of the author and do not necessarily reflect the views of the National Science Foundation.

I am deeply indebted to my parents and family for their continual support and interest in my education as well as their encouragement throughout my education.

I am also sincerely thankful for my dear friend Caleb who has exemplified and continually reminded me of the fact that if you can dream it, you can do it.

Last of all, I am extremely grateful for my lovely wife Olivia. I would not be where I am today without her. She provided unwavering support and care throughout many health issues I faced throughout my graduate experience. She also continually reminded me of her profound belief in my work and in my abilities to finish what I had started.

ABSTRACT

Oxy-fuel combustion processes are promising technologies for power generation that allow CO₂ recovery and sequestration using essentially conventional equipment. Although oxy-fuel combustion has been well researched over the years, there are fundamental issues related to the associated ash deposition processes and their subsequent impact on radiative heat transfer that need to be understood before oxy-fuel combustion can be fully scaled up to a commercial scale. Ash formation and deposition is a complex physio-chemical process consisting of: vaporization, condensation, melting, fragmentation, nucleation and coagulation of the mineral matter and organically bound metals in the parent fuel that results in a distinct tri-modal distribution of the ash particles within the combustor. Recent experimental evidence from the University of Utah has shown that a correlation exists between the rate of deposition of the tightly bound “inner” ash deposit layer adjacent to the heat transfer surfaces (which is difficult to remove) and the concentrations of the submicron aerosols in the flue gas. However, predicting these time-dependent particle size distribution characteristics during combustion as the parent fuel transitions to ash using the commonly employed Lagrangian tracking based particle simulation methodologies in Computational Fluid Dynamics (CFD) frameworks is extremely challenging. Further, Lagrangian tracking methods assume isotropic turbulence near the walls (that can impact deposition characteristics) as well as optically thin radiative losses from particles and exhibit low parallelization efficiencies. On the other hand, Eulerian particle tracking methods, like the population balance framework, are more amenable to capturing the nucleation, fragmentation and

coagulation characteristics of ash. In addition, near-wall turbulence characteristics and radiative heat losses can potentially be modeled more rigorously. The overall goal of the research reported in this thesis was to examine the oxy-fuel combustion simulation characteristics of two multiphase modeling frameworks (Lagrangian and Euler-Euler) with the goal of evaluating their potential to simulate ash formation and deposition processes. Consistent and identical phenomenological laws for the interphase interactions were utilized across all three frameworks by implementing user-defined (add-on) subroutines to model the diffusional and kinetic resistances associated with the heterogeneous char oxidation, non-grey effects of gas radiation and the variations in the radiative properties of the solid phase during combustion. Prediction accuracies of the different frameworks were assessed by comparisons against measurements of: (1) flame stand-off, (2) temperature and velocity at different axial locations, (3) radiative heat transfer and (4) ash deposition rates of a non-swirling and a swirling oxy-coal flames (burning an Utah Bituminous and Sub-Bituminous coal, respectively) carried out at the University of Utah.

Only the Euler-Euler model was able to capture the experimental observed trends for flame stand-off as a function of oxygen concentration in the primary burner. Non-swirling flame temperature and velocity predictions were in reasonable agreement with measurements across both multiphase modeling frameworks. Swirling flame temperature and velocity predictions were not in reasonable agreement with measurements. Radiation was the dominant mode of heat transfer with the radiative heat loss fraction (Radiative heat loss/Total chemical heat release) determined to be 0.6 for both non-swirling flames and 0.7-0.9 for both swirling flames. Radiation from the participating gases accounted for 75% of the radiative heat transfer. The incident radiative flux predictions were in good agreement with measured values from similar flames in this furnace. The predicted relative concentrations of the submicron aerosols in flue gas in two flames (Oxy27 and

Oxy70) were in reasonable agreement with measurements for the Oxy27 flame but not the Oxy70 flame.

CHAPTER 1

INTRODUCTION

1.1. Motivation

Oxy-fuel combustion processes represent a promising suite of technologies for power generation with CO₂ capture using essentially conventional equipment. In oxy-fuel combustion, a fuel (e.g. coal) is oxidized using O₂ without nitrogen as the primary diluent. Most commonly, O₂ is generated in an oxygen/nitrogen separation system and blended with recycled flue gas in order to control the temperature in the combustion zone of the boiler. By removing the nitrogen prior to combustion, a nearly pure CO₂ gas stream is produced which can be more easily captured and reused or sequestered prior to emission. This technology also has the potential to reduce the cost of other commonly used pollutant emission control technologies such as those to abate the emission of NO_x [1].

As noted by Chen et al., although oxy fuel combustion for coal and coal/biomass systems are well researched, both by experimentation and modeling, there are notable challenges that still need to be overcome before oxy-fuel combustion can be fully scaled up to a commercial scale [2]. Chen et al. divides these challenges into three fundamental issues that remain uninvestigated: oxy-coal system design issues, large scale demonstration, and computational fluid dynamic (CFD) modeling of oxy-coal combustion issues [2]. Of these fundamental issues, the research herein provides advancements in the third of these areas, specifically the use of CFD modeling for characterizing flame stability, further characterizing ash deposition (building a framework to determine ash deposit growth rate with respect to time) and determining the impact of radiative heat transfer in oxy-fuel combustion environments.

The University of Utah has completed multiple experimental studies of oxy-fuel combustion scenarios in their downflow laboratory combustor (oxyfuel furnace or OFC). Two of these studies were chosen as the target of research for this thesis: a non-swirling oxy-coal flame stand-off study and a swirling oxy-coal flame ash deposition study.

Dispersed, multiphase flows, like those modeled in this thesis, can be modeled in differing frameworks (*see Chapter 4*). Currently, most CFD simulations of particle combustion utilize a Lagrangian tracking method for the particle phase while employing an Eulerian framework for the fluid phase. This is known as the Euler-Lagrange approach. While this approach has been well-established, in the context of ash deposition modeling, it has some shortcomings including an inability to model particle break-up/fragmentation, coagulation, and the assumption of isotropic turbulence assumption near the walls. To alleviate these shortcomings, a few studies have explored the utilization of an Euler-Euler approach. While being more rigorous in overcoming the aforementioned modeling limitations, this approach has difficulty in converging simulations when employed in a steady-state fashion. The analyses in this thesis were completed from a fresh perspective by using two multiphase hydrodynamic frameworks, Euler-Lagrange and Euler-Euler, to explore the oxy-fuel combustion characteristics. This is the first work that we are aware of that rigorously assesses the efficacies of the different modeling frameworks through comparisons against experimental measurements.

1.2. Objectives

The focus of this research was to assess the prediction accuracies of the three multiphase modeling methodologies by utilizing consistent and identical phenomenological laws for the interphase interactions across all three frameworks. Comparisons were made against experimental measurements of: flame stand-off distance as a function of primary oxygen concentration, radiative

heat fluxes, axial temperatures and velocities, and ash deposition rates. Additionally, the individual contributions of particle, gas and wall to the radiative fluxes during oxy-fuel combustion were quantified.

The overall goal of these objectives was to properly describe oxy-fuel combustion environments and establish a framework to predict the growth of ash deposit with time. Accurately characterizing: (1) particle size distribution, (2) particle composition, and (3) wall emissivities throughout the furnace were all seen as key players impacting ash deposition rates and wall radiative fluxes.

1.3. Thesis Outline

This thesis utilizes experimental measurements from two distinct oxy-fuel combustion campaigns carried out at the University of Utah. The first campaign utilized a non-swirling burner (burning an Utah Bituminous coal as fuel) and was aimed at studying flame stand-off while the second study utilized a swirling burner (burning an Utah Sub-Bituminous coal as fuel) with the aim of studying ash deposition rates. In this chapter, the motivation behind this thesis was presented. Chapter 2 provides an overview of ash deposition mechanisms and their subsequent impacts. Chapter 3 outlines various multiphase modeling frameworks in detail. Chapter 4 presents the project overview, methods, and results from the non-swirling oxy-coal combustion study. Chapter 5 presents the project overview, methods, and results from the swirling oxy-coal combustion study. Finally, Chapter 6 examines the conclusions of the thesis and provides a detailed description of future work.

CHAPTER 2

ASH DEPOSITION: MECHANISMS AND IMPACTS

2.1. Ash Deposition in Coal and Coal/Biomass Systems

Ash deposition in coal systems during combustion processes has a number of consequences:

1. A reduction in the thermal efficiency of a furnace [3],
2. Affects upon the integrity of the boiler/boiler tubes due to corrosion/erosion [3],
3. Increases in the frequency of power plant shutdowns for maintenance and/or cleaning,
and
4. Increases in soot-blowing requirements [4].

Understanding ash deposition mechanisms is critical in understanding how to model ash deposition. Essentially, the net rate of deposition depends on three criteria: ash particle formation, the rate of transport of particles to the heat transfer surface area, and the particles' propensity to 'stick' to the surface once they reach it [5].

2.1.1 Ash Particle Formation

Ash particle formation is directly related to the mineral content within the coal and the pathways the mineral content takes to form ash. There are three conditions related to mineral content which affects ash formation: nature/distribution mode of minerals/trace elements (TEs), the mineral form, and the mineral particle size distribution (PSD) [6]. There are three distribution modes of minerals/TEs in the coal: organically associated material (incorporated into the organic structure of the coal), inclusions, or exclusions [7]. Figure 2.1 shows a pictorial difference between

each of these regimes. TEs in each of these regimes will experience different conditions, detailed below, that will affect vaporization [7].

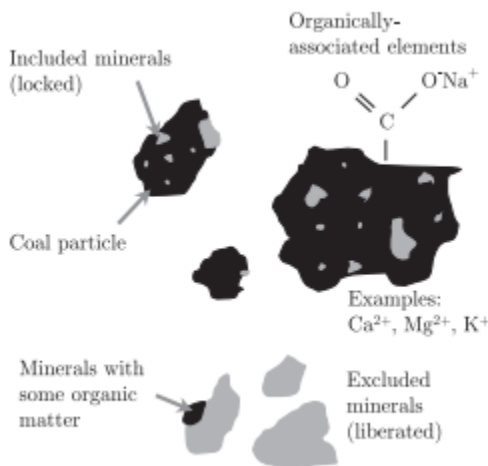


Figure 2.1: Inorganic constituents in the coal matrix and their occurrence [4].

Organically associated minerals/TEs are organic compounds with inorganic elements; these minerals are typically composed of K^+ , Na^+ , Ca^{2+} , Mg^{2+} , Fe^{3+} , and Al^{3+} [4, 7]. There are two reasons organically associated TEs are released into the vapor phase: bond cleavage during carbon oxidation and the very high temperature microenvironment that is strongly reducing [8].

Mineral inclusions are contained within the coal matrix. TEs located within mineral inclusions are associated with a specific mineralogical matrix, primarily pyrite, mono- and disulfides, carbonates, and various alumina-silica minerals [7]. The inorganic mineral content in coal varies depending on the region/mine it is acquired from but are primarily composed of Na, Mg, Al, Si, P, S, Cl, K, Ca, Ti, Mn, Fe, and Zn [9, 10]. TEs in mineral inclusions are surrounded by the burning carbon matrix, which may interact with the TEs as included minerals begin to melt allowing volatile and semi-volatile TEs to vaporize [8, 11]. The high temperature microenvironment inclusions are exposed to will commonly be reducing due to the rapid consumption of oxygen by the surrounding carbon oxidation [7]. Excluded minerals in forms similar to included minerals will be exposed to lower temperatures and a more neutral/oxidizing

environment [8]. James et al. showed TE release is proportional to the elemental concentration in the original inclusions and excluded pyritic minerals as well as the temperature profiles of the related coal particles and their respective initial sizes [12].

Mineral matter form affects how well the minerals are vaporized. Kleinhans et al. points out that most minerals within the coal matrix are in their crystalline form, with few in their amorphous phases [4]. Gupta et al. provides examples of how mineral matter mode of occurrence can affect vaporization. For example, silica can take the form of quartz, illite, and kaolinite. In the form of quartz, it is relatively least reactive, but in the form of illite, it will coalesce with other minerals rapidly [6]. Similarly, calcium illite and magnesium illite will react rapidly, but while in calcite and ankerite forms, they increase the viscosity of the molten phase by large mineral grain fragmentation [13].

Gupta et al. shows that the mineral PSD affects evaporation; intuitively, large mineral grains are less reactive than smaller gains since the center of the larger mineral grain will not participate in the ash reactions [6].

When a fuel containing mineral matter/TEs/organically bound elements is burned, inorganic matter will either vaporize within or near the burning fuel particle or will melt and coalesce to form larger particles that are released as the residual char is fragmented [4]. There are several physical transformation pathways these inorganic minerals can take during this devolatilization and char conversion process as presented in Figure 2.2.

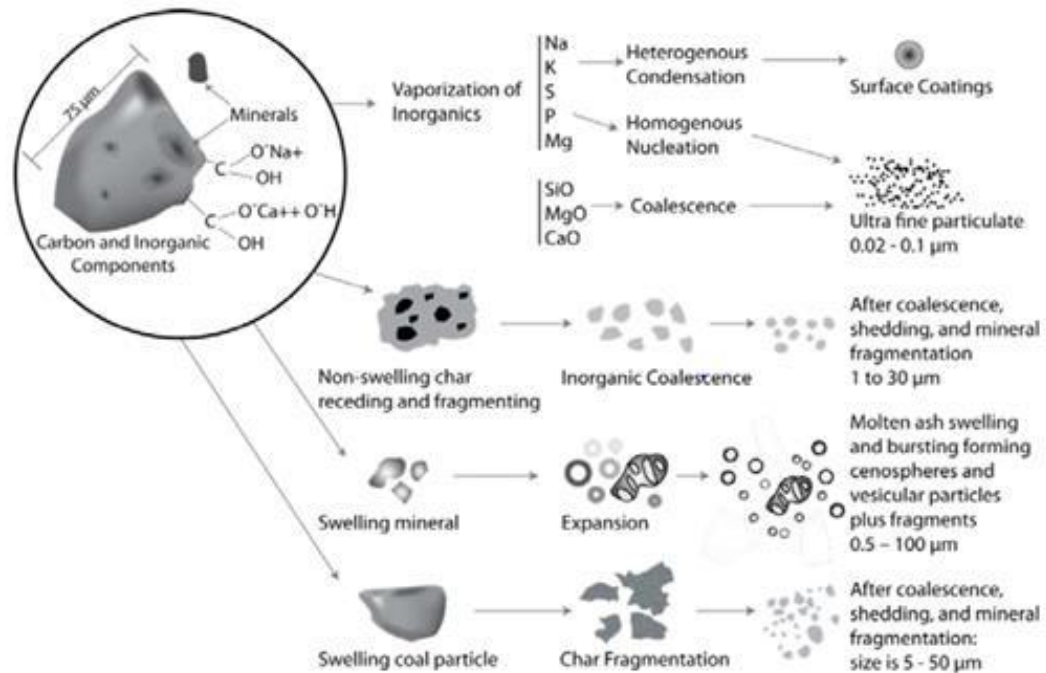


Figure 2.2: Major physical transformations of ash components during combustion [14].

Notable work on coal ash fine-fragmentation mode mechanisms, summarized here, has been generated by my co-advisor Dr. Seames and his colleagues. Jassim et al. investigated the influence of fragmentation on pyrite particle thermal history and sulfur release rate [15]. They concluded that fragmentation produces smaller particles which heat up faster (allowing particles to reach their melting point faster), undergo more rapid oxidation, and release sulfur more quickly [15]. Fix et al. investigated the effect of oxygen-to-fuel stoichiometry (OFS) and combustion temperature on coal ash fine-fragmentation mode formation mechanisms [16, 17]. They reported that a larger coarse ash particle mode seems to be unaffected by the OFS while, for the smaller ultrafine ash particle mode, a 1.05 OFS ratio lowered the fraction of ultrafine ash when compared to the 1.20 and 1.35 OFS ratios; a 1.05 OFS ratio appeared to increase the portion of the fine-fragmentation mode [16]. Also, based on a detailed qualitative analysis of fine fragmentation mode ash particles, they concluded that formation mechanisms may depend upon peak combustion temperature [17]. In an initial study of the fine fragmentation fly ash particle mode, Seames found

that the fine fragmentation region appears to be more reactive with oxy-anion trace elements than the supermicron fly ash region indicating that the fine fragmentation region may be important in the partitioning of semi-volatile trace elements [18].

Depending on the fuel type, most of the inorganic minerals will vaporize while the remaining inorganic minerals will decompose, transform to ash, melt, and coalesce [4].

Vaporized inorganic minerals, depending on their volatility, will nucleate and coagulate to form ash particle, condensate onto ash particles, or remain the gas phase reacting into less volatile forms. For example, mineral elements in coal, such as Na, K, S, are highly evaporable while some of them have low volatility, such as Si, Al, Fe, Ca and Mg [9]. Vaporized metals, depending on their volatility and concentration when compared to saturation, can oxidize, nucleate, condense, or be absorbed onto particles both in the micro-environment surrounding the burning fuel and in the macro-environment of the combustion zone [19]. It was observed experimentally that during the vaporization and condensation portion of the ash formation process, inorganic, refractory oxides like SiO_2 , CaO , MgO , and Fe_2O_3 are large contributors to the amount of submicron ash generated [20-22]. Additionally, KCl , K_2SO_4 , and $\text{K}_2\text{O}\cdot\text{SiO}_2$ were noted the main inorganic minerals generated during the combustion of biomass [23].

Additionally, the formation process is influenced by the combustion environment (i.e. air firing as opposed to oxy-combusiton) [6].

2.1.2 Ash Particle Transport

Particle transport is indirectly related to the particle (mineral) size distribution [6]. Two major mechanisms define the transport of the particles: inertial impaction and thermophoresis [24]. Other notable mechanisms that define the transport of the particle include adsorption, condensation, surface reactions, Fick's diffusion (vapors) and eddy deposition.

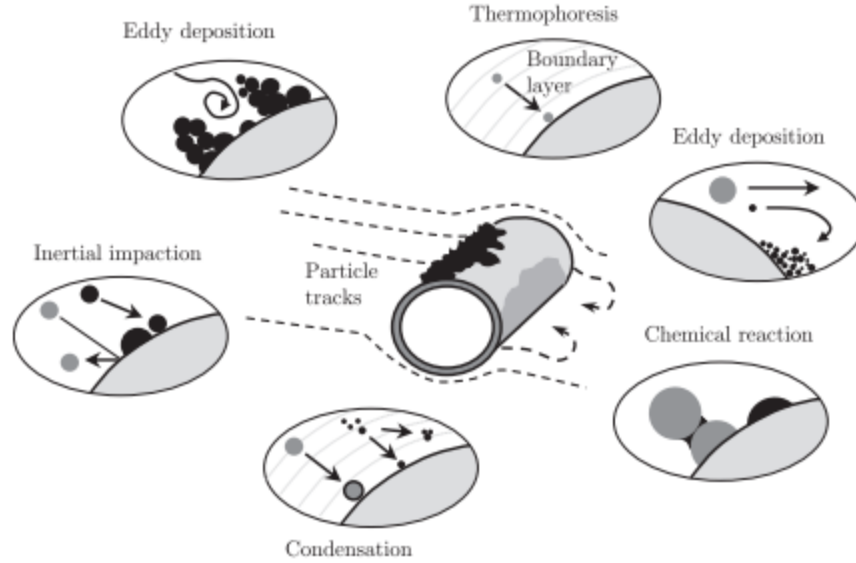


Figure 2.3: Ash deposition mechanisms on a superheater tube [4].

Inertial impaction of fragmentation mode particles is a process that depends on the local aerodynamics in the region of the heat transfer surface area, target geometry, and particle size and density. Thus, inertial impaction mainly affects the larger ash particles [9, 25]. This mode of transportation is considered the dominant ash deposition mechanism due to its quick deposit build up on superheater tubes [4]. Inertial impaction rate is positively correlated with the stokes number which is the ratio of the characteristic time of a particle to come to rest when injected into a stagnant fluid to a characteristic time of the flow to pass over a distance equal to the tube radius [26]. The stokes number is defined by equation 2.1:

$$Stk = \frac{\rho_p d_p^2 u_p}{9\mu_g d_c} \psi \quad (2.1)$$

where ρ_p is particle density, d_p is particle diameter, u_p is particle velocity, μ_g is gas viscosity, d_c is tube diameter, and ψ is a correction factor for particles that disobey Stokes' law.

Thermophoresis affects intermediate sized particles (particle sizes less than 10 microns) and is due to the macroscopic temperature gradient between the particle and the heat transfer

surface area. This force acts from the hot gas towards the cold gas essentially drawing particles closer to the superheater tubes [4]. Intuitively, thermophoresis would be less effective once large ash deposits are in place due largely to a lower temperature gradient [9].

Adsorption of TEs to particle surfaces of inorganic compound occurs in the gas phase.

Condensation of inorganic vapors, as Kleinhans et al. defines it, occurs during cooling when the flue gas is supersaturated, and gas temperature falls beneath the vapor dew point [4].

Surface reactions of inorganic vapors is yet another contributing ash deposition mechanism. The most influential of these surface reactions are sulfation, alkali absorption, oxidation, reduction, and carbonation [4, 27].

Eddy deposition, as shown in Figure 1.3, transfers ash particles to the tube surface via turbulent eddies. This ash deposition mechanism has a much larger effect on bringing smaller particles to the tube surface than inertial impaction [9].

Fick's diffusion is a concentration gradient force for inorganic vapors to reach the tube surface [24].

2.1.3 Ash Particle Stickiness

Particle stickiness has a direct relationship between the particle properties and the targeted tube/wall surface. Kleinhans et al. briefly summarizes factors that influence particle stickiness [4]:

1. Particle properties (i.e. melt fraction, viscosity, surface tension, etc...)
2. Particle kinetic energy
3. Particle shape
4. Particle surface roughness
5. Angle of impaction
6. Surface roughness

7. Surface geometry
8. Surface properties (i.e. melt fraction, viscosity, surface tension, etc...)
9. Forces between particles and surface (i.e. van der Waals forces, etc...)

2.2. Ash Deposition Modeling

Computational Fluid Dynamics (CFD) methodologies are currently utilized to predict the performance of boilers and to help operators and engineers anticipate and resolve ash-related problems [24, 28]. Currently, CFD-codes detect boiler areas susceptible to ash deposit formation by relating the location of the ash particles to the deposition surface [29]. In order to compute the arrival rate of the ash particles to the deposition surface, the localized flow near the surface must be characterized in great detail [29]. Weber et al. [29] suggest that by combining CFD-predictions with an advance fuel characterization, ash depositions issues can be resolved.

Cai et al. [30] has performed an extensive review of ash formation and deposition in coal and biomass boilers tabulating up to date experimental, simulated, and mechanical work done on these topics. Of these works, Table 2.1 displays some notable publications in which CFD computations have been used to model ash deposition. The mathematical models described in Table 2.1 are discussed below in order of sub-model type.

It's important to note that many publications on slagging and fouling emphasize the key role of inertial impaction when related to thermophoresis, eddy diffusion or vapor condensation due largely to the prerequisite that a particle that does not impact does not form a deposit [29]. Additionally, when modeling ash deposition, two concepts are often over-looked or over-estimated: predicting the impaction efficiency and the rate of the particles arrival to the deposition surface [29].

Table 2.1: CFD-based predictions of ash deposition in boilers [29].

Work	Boiler/Fuel	Mathematical Model/Numerical Simulations Results
Wang et al. 1997 [24]	Utility boiler Fuel: Wyoming and Oklahoma coal	PCGC-3 code, Ash deposition submodel included, Predicted influence of deposit growth on heat flux, Predicted elemental composition of deposits, Ash transported through inertial impaction and thermophoresis, Ash sticking propensity determined by physical characteristics (viscosity).
Fang et al. 2010 [31]	300 MW down-fired boiler Fuel: Slagging-tendency coals	Slagging model coupled with gas-solid two phase flow, Eulerian description for continuum phase, Particle transport modeled by stochastic trajectory model, predicted slagging mainly on side walls in lower furnace.
Fan et al. 2001 [3]	Pulverized coal-fired boiler Fuel: Coal Deposit region considered: boiler walls	Gas-solid two-phase flow model (Lagrangian/Eulerian approach), Model simulates deposit growth under slagging conditions, Stochastic separated flow (SSF0 model describes particle impaction rates, Ash sticking propensity determined by critical viscosity model. Deposits grow rapidly where particles' impacting probability and temperature of the wall surface are high.
Ma et al. 2007 [32]	512 MW tangentially-fired boiler Fuel: Powder River Basin (PRB) coal Deposit region considered: boiler walls	AshPro tool (integrates ash behavior models), Predicts deposit thickness, chemical composition, physical properties and heat transfer properties in furnace wall or convective pass regions.
Lee et al. 1999 [5]	Single-burner pilot scale rig Fuel: UK coals Deposit region considered: combustion chamber walls	CINAR code (utilizes Eulerian conservation equations for gas phase), Predicts slagging potential and deposition patterns, Particle trajectories found by equation of motion for a single particle, Ash sticking propensity determined by the Urbain viscosity model.
Beckmann et al. 2016 [28]	15 kW pulverized coal jet flame Down-fired combustion chamber Fuel: Bituminous coal	Fluent CFD code, Predicted deposition rates, Ash transported through inertial impaction, thermophoresis and eddy diffusion, Ash sticking propensity determined by five well-known models (based on viscosity, ash softening temperature)
Kaer et al. 2006 [33]	Grate-fired, Combined Heat&Power Plant, Masnedo, Denmark Fuel: Straw Deposit regions considered: free-board; platen superheaters and tube banks	Fluent CFD code; Ash formation model for grate combustion of straw, Ash transport through inertial impaction and thermophoresis, Ash sticking propensity determined using melting curves for potassium salts and silica-rich particles

Table 2.1 (cont): CFD-based predictions of ash deposition in boilers [29].

Work	Boiler/Fuel	Mathematical Model/Numerical Simulations Results
Forstner et al. 2006 [34]	Grate-fired 440 KW _{th} boiler Fuel: waste wood Deposit regions considered: combustion chamber walls, fire tube walls	Fluent CDF code, Ash release model for grate combustion of wood, Ash release model for ash forming vapours, Ash transport through inertial impaction and condensation of vapours, Ash sticking propensity determined using Urbain viscosity model
Epple et al. 2005 [35]	330 MW boiler of Meliti Achlada Florina, Greece Fuel: Lignite Deposit regions considered: furnace walls	FLOREAN code of TU Braunschweig, Fly ash properties predicted using a coal combustion model, Ash transport through inertial impaction, Ash sticking propensity based on ash fusion temperature
Mueller et al. 2003 [36]	105 MW fluidized bed boiler Fuel: Wood Deposit regions considered: Free-board, secondary combustion chamber, boiler walls	Fluent CFD code, Ash formation model includes fly ash and bottom ash fractions which are determined using chemical fractionation analysis, Ash transport through inertial impaction, Ash sticking propensity determined using melting curves for the fly ash; sticking temperature corresponds to 15 wt.% of molten phase in the fly ash
Eddings et al. 2001 [37]	900 MW tangentially-fired boiler Fuel: Bituminous coal Deposit regions considered: boiler walls	GLACIER code of Reaction Engineering International, Fly ash properties predicted using a coal char combustion model, Separate treatment of extraneous and included pyrite, Ash transport by inertial impaction, turbulent eddy transport and thermophoresis, Ash sticking propensity based on the critical particle temperature T ₂₅₀ of the fly ash
Schell et al. 2001 [38]	450 MW German Boiler Fuel: Brown coal Deposit regions considered: boiler walls	AIOLOS code of IVD of Stuttgart, Fly ash amount and size distribution are model inputs, Ash transport through inertial impaction, turbulent eddy transport and thermophoresis, Ash sticking propensity determined using a linear dependence of the sticking probability with temperature, Effects of the deposit on heat transfer rates are determined
Bernstein et al. 1999 [39]	800 MW boiler Fuel: Brown coal Deposit regions considered: boiler walls	Fluent CFD code, Fly ash properties predicted using a coal char combustion model, Ash transport by inertial impaction, Ash sticking propensity expressed as a product of three terms: melting temperature function, particle concentration function and oxygen concentration function

When calculating the ash particle sticking propensity, the viscosity of the ash particles has been conventionally used as an important parameter [29]. To find the fraction of ash particles that deposits, the actual viscosity is typically compared with a critical viscosity [40]. Additionally, an assumption for viscosity-based models is made: the sticking propensity of particles during inertial impaction is determined by the effective viscosity of the deposition surface and the ash particle's viscosity (which is a complex function of oxygen partial pressure, chemical composition, and temperature in boilers) [30]. However, there is a lack of consistency when choosing a critical viscosity. Values as low as 1 Pa·s and as high as 10 Pa·s have been used [29].

In a shortened approach for ash deposition modeling, Lee et al. [5] utilized the Urbain viscosity model to calculate sticking probability by estimating particle viscosity, arbitrarily chosen to be 105 Pa·s, and comparing it with a critical velocity [41]. In their set up, the sticking probability was one for particle viscosities less than the critical value, while the sticking probability was the ratio of critical viscosity to the actual viscosity for viscosities higher than the critical value, [41].

Costen et al. [42] applied the Kalmanovitch and PSI viscosity model to calculate ash particle viscosity. They choose a critical viscosity of 105 Pa·s (the Kalmanovitch model applies for high temperature and low viscosity particles while the PSI model is vice versa). Other ash particle sticking models use temperature and ash softening as sticking criteria [28-30].

An extensive review provided by Weber et al. [29] showed that the char burnout kinetics for the last 20% of carbon were deemed critical for temperature dependent sub-models.

When the particle or deposition surface is not sticky and the Weber number is less than the critical value of 1, an ash/char particle capture sub-model can be utilized. This sub-model is known as the Weber number criteria [43]. The Weber number (We) is defined as the ratio of particle kinetic energy and slag surface tension energy between as shown in equation 2.2:

$$We = \frac{\text{particle kinetic energy}}{\text{surface tension energy}} = \frac{\rho_p u_p^2 d_p}{\sigma_{sp}} \quad (2.2)$$

where ρ_p is particle density, u_p^2 is particle velocity, d_p is particle diameter, and σ_{sp} is the particle surface tension when a solid particle is molten or when the wall is wet [44].

Coagulation and fragmentation modeling were determined to be critical in correctly predicting the ash particle size distribution. Baxter [45] and Syred et al. [46] have performed an extensive particle fragmentation review. Both Beckmann et al. [28] and Weber et al. [29] introduced an ad hoc correction function:

$$\frac{D}{D_0} = \left(\frac{C}{C_0}\right)^{0.7} \quad (2.3)$$

where D is the particle diameter, D_0 is the initial particle diameter, C is the carbon content of the particle, and C_0 is the initial concentration of carbon in the particle. When implemented, the “ad hoc” correction aided in good PSD agreement between measure values and CFD calculations [29].

There are many models used to predict the movement of ash particles toward the deposition surface. Generally, these models incorporate the two main modes of transportation: inertial impaction and thermophoresis. Table 2.1 shows inertial impaction modeling in many works [24, 28, 33-39]. Most modeling of inertial impaction involves using a particle tracking procedure (an equation for the motion of the particle depending on the frame of reference) and an impaction efficiency as defined by the stokes number [29]. Table 2.1 also presents thermophoresis modeling in many works [24, 28, 33, 37-38]. Costen et al. [42] presents a general model of how a thermophoretic force is modeled:

$$F_{th} = -\frac{v}{t_p} \frac{K_{th}}{T} \left(\frac{dT}{dy}\right) \quad (2.4)$$

where ν is the gas kinematic viscosity, T is the mean gas temperature in the vicinity of gas and particle, and dT/dy is the temperature gradient. K_{th} is a thermophoretic coefficient determine from an interpolation formula [47, 48].

In tangential fired boilers, Balakrishnan et al. [49] suggested that thermophoresis is probably more important than inertial impaction.

Other notable modeling works include a predictive scheme for ash deposition modeling based on CCSEM fly-ash data and CFD developed by Costen et al. [42]. The improved accuracies in their modeling were associated with taking into account the mode of association of ash in the particle; something that is not done with the Lagrangian modeling approach.

Overall, when it comes to ash deposition modeling, Weber et al. [29] noted that for CFD-codes to accurately predict particle impaction efficiency, the flow field around the deposition surface must be accurately characterized.

Ash deposition processes impact the combustor radiative heat transfer in two distinct ways. First, the PSD and compositions of the particles impact the incident radiative fluxes to the walls. The extent of this influence depends on the relative contributions of the particle radiation to the gas radiation and the background wall radiation. Second, and more importantly, the characteristics of the deposited ash alter the surface emissivity/absorptivity and impact the net radiative heat fluxes (and effectively the heat absorbed at the steam side of the boiler). While a deposit free surface may have a total emissivity/absorptivity of 0.8, ash deposits may reduce this value to as low as 0.3 [50]. In addition, ash deposits reduce the thermal conductivity of surfaces.

2.3. Particle Size Distribution Impact on Radiative Heat Transfer

Particle properties (i.e. size, shape, composition, etc...) have a direct impact on the radiative properties of particles. During combustion processes, the parent fuel, char, fly ash, and soot all have varying radiative properties as suggested by their differing compositions [51]. Table 2.2 displays some notable publications in which CFD computations have been used to model radiative heat transfer during oxy-coal combustion. This table contains the type of radiation models, particle radiation models, and particle bin number (i.e., the number of discrete particle sizes resolved in the simulations). The vast majority of CFD computations have used constant values (experimental values) for particle radiation values, while some have used codes based on Mie theory. It is important to note that ash particle radiative values vary with particle properties; consequently, using constant values for particle radiation values is incorrect.

Characterization of particle size distribution throughout the boiler has been carried out as exemplified by Beckmann et al. [28]. However, as discussed earlier, characterizations like this one have not accounted for coagulation and fragmentation behavior. Additionally, most studies do not have an adequate resolution (diameter intervals) for their particle size distributions. In order to get detailed PSD and concentration data for comparisons against experiments, a large number of particle tracks are needed. Krishnamoorthy and Wolf [51] showed that to get accurate radiative fluxes, 40 diameter bins are needed. Although this is feasible in small scale geometries, it becomes computationally expensive in large-scale 3D simulations.

Table 2.2: Radiation models utilized in oxy-fuel combustion CFD modeling work.

Author	Modeling approaches				Conclusions
	Radiation	Particle Radiation	Reaction mechanism	# Particle Bins	
Wall et al. 2009 [52]	4-grey gas model by Gupta et al. [60] and Hottel's Charts [61] for gaseous emissivities	Constant, tabulated emissivity values	Volatile combustion and char reactivity	...	Emissivity of the gases predicted by new 4-grey gas model.
Yang Et al. 2018 [53]	FSCk property model and Smith's WSGG model	Mie theory based data and constant values	Two-step reaction mechanism	10	Refined radiative property models show higher gas radiation source term, lower particle radiation source term in the flame region, and higher flame temperatures. Predicted heat transfer is closer to experimental data by employing refined methods.
Guo et al. 2015 [54]	Adapted WSGG model by HUST [62]	Constant gaseous/particulate absorption coefficient	Three-step global mechanism	...	Peak temperature and peak wall heat flux decreases as a result from the physical and chemical effects CO ₂ and water.
Al-Abbas et al. 2012 [55]	WSGG model of Smith et al. [63]	Constant Values	Three-step global mechanism	...	Noted similarities and difference between gas temperature levels and radiative heat transfer between air and oxy-combustion cases.
Habermehl et al. 2012 [56]	Non-gray implementation EWB model	Constant Values	Volatile Combustion [65], CO burning [66] and H ₂ burning	...	Changes in the radiative heat flux to the wall of the boiler is significantly influenced by change in optical properties of the flues gas when comparing air-firing to oxy-combustion
Black et al. 2013 [57]	Standard WSGG model	Constant Values	Volatile combustion and CO burning	...	Noted difference in air-biomass and oxy-biomass conditions. When firing with biomass, lower total heat transfer to the tubes was observed and contributed to the effects of large biomass particles.
Yin et al. 2011 [58]	WSSG model by Yin et al. [64]	Constant Values	Redefined WD 2-step mechanism by Andersen et al. [67]	...	Newly used WSGGM model highly recommended over conventional WSGGM model for more accurate results and scale-up issues.
Nikolopoulos et al. 2011 [59]	Simplified EWB model	Constant Values	Volatile combustion [68] and CO burning [69]	...	Simulation results indicate increase in predicted total and radiation heat fluxes in furnace at oxy-fuel conditions which is expected due to the higher emissivity of the flue gas.

Table 2.2 (cont.): radiation models utilized in oxy-fuel combustion CFD modeling work.

Author	Modeling approaches				Conclusions
	Radiation	Particle Radiation	Reaction mechanism	# Particle Bins	
Nakod et al. 2013 [70]	Gray [75-76]] and non-gray [77] WSGG model	UDF/tabulated emissivity values for coal, char, and ash	Volatile combustion and CO burning	...	Confirms the temperature and wall radiative flux profiles seen during air firing can be replicated in both dry and wet FGR scenarios through an appropriate selection of CO2 and water/oxygen molar ratios in the oxidizer stream. (Further conclusions listed)
Hu et al. 2013 [71]	Two weighted-sum-of-gray-gas (WSGG models) [63-64]]	Constant Values	Volatile combustion and CO burning	...	WSGG-Y in model made an adequate predication of radiation intensity while the radiation intensity was underestimated by WSGG-Smith model. The radiation intensity increases with the increase of effective O2 concentrations or the decrease of FGR ratio, and the peak position moves toward to the burner.
Edge et al. 2011 [72]	WSGGM coupled with DOM. FSK used in addition during oxy-tests	Constant Values, grey particle values	Volatile combustion and CO burning	...	Suggest large eddy simulations (LES) offer improvements over Reynolds average Navier-Stokes (RANS) in predicting recirculation zone and flame properties. LES surface incident radiation predictions differ slightly from RANS.
Clements 2016 [73]	FCK model with five-point Gaussian quadrature. Compared to WSGG model and narrow band CK model	Mie Theory	Volatile combustion and CO burning	...	FCK and non-grey WSSG models recommended for modelling radiation. Non-grey particle radiative properties had little impact on the narrow band calculations; however these calculations were undertaken with band-averaged properties in uncoupled calculations, and further calculations without any spectral averaging or with fully coupled calculations may identify different results.
Johansson et al. 2013 [74]	Statistical-Narrow-Band (SNB) model	Mie Theory	Results show particle radiation dominates the total radiation. Scattering of the particles would have a large effect on the radiative transfer; the non-scattering assumption in this study leads to significantly larger wall fluxes than isotropic scattering.

2.3.1 Radiation Modeling

The variables of interest in most radiative transfer analysis are the distributions of radiative heat flux vectors ($\mathbf{q}(\mathbf{r})$) and the radiative source terms ($-\nabla \cdot \mathbf{q}(\mathbf{r})$). Distributions of the radiative heat flux vectors are necessary to perform accurate energy balances on any solid/liquid interfaces within the solution domain and at the boundaries. The radiative source term describes the conservation of radiative energy within a control volume and goes into the energy balance equation associated with the fluid flow. Therefore, these variables couple radiation with the other physical processes that occur in a combustion simulation. To determine the distributions of these quantities, a transport equation describing the radiative transfer needs to be solved first. If “ I ” represents the directional intensity, k_a the absorption coefficient (which is due to the gases as well as the particulates in the combustion media), σ the scattering coefficient (due to the particulates alone), I_b the black body emissive power and Φ the scattering phase function (assumed to be forward scattering for the bubbles), then the differential equation governing the radiative transfer can be written as [78]:

$$\begin{aligned} \nabla \cdot (I_i(\vec{r}, \hat{s})\hat{s}) = & -(k_{a,g,i} + k_{a,p} + \sigma_p)I_i(\vec{r}, \hat{s}) \\ & + k_{g,i}w_{g,i}I_{bg}(\vec{r}, \hat{s}) + k_{p}w_{p}I_{bp}(\vec{r}, \hat{s}) + \frac{\sigma_p}{4\pi} \int_0^{4\pi} I_i(\vec{r}, \hat{s}') \Phi(\hat{s}, \hat{s}') d\Omega' \end{aligned} \quad (2.5)$$

In equation 2.5, the subscripts “ g ” and “ p ” correspond to the gas-phase and particulate phase, respectively. The subscript “ i ” corresponds to the “gray gas” employed to estimate the gas radiative properties and “ w ” corresponds to the weighting factor associated with the blackbody emissive power.

The gas radiative property modeling methodology adopted in this thesis falls under the category of weighted-sum-of-gray-gases (WSGG) models where the emissivities of gas mixtures

are expressed in a functional form consisting of temperature independent absorption coefficients (k_i) and temperature dependent weighting fractions $w_i(T)$. The WSGG model parameters employed in this thesis have been validated previously through comparisons against benchmark/line-by-line (LBL) data for prototypical problems that are representative of compositions, H₂O/CO₂ ratios, and temperatures encountered during combustion in air and oxy-combustion [77, 79]. For further details on the WSGG modeling methodology and the gas radiative property models employed in this study, the reader is directed to references 79-80. In this study, the particle radiative properties were assumed to be “gray” (i.e. maintained constant across all gray gases (i)), and the particle temperature was assumed to be equal to the surrounding gas temperature (i.e., I_{bg} and I_{bp} were equal at all spatial locations) [81].

The radiative heat fluxes within the domain or at a surface and the radiative flux divergence are determined by integrating over the solid angles (Ω) surrounding a point as [80]:

$$\mathbf{q}(\mathbf{r}) = \sum_i \int_0^{4\pi} I(\mathbf{r}, \hat{\mathbf{s}}) \hat{\mathbf{s}} d\Omega \quad (2.6)$$

$$\nabla \cdot \mathbf{q}(\mathbf{r}) = \sum_i (k_{a,g,i}(\mathbf{r}) + k_{a,p,i}(\mathbf{r})) (4\pi I_b(\mathbf{r}) - G_i(\mathbf{r})) \quad (2.7)$$

G , the incident radiation, is calculated as:

$$\mathbf{G}(\mathbf{r}) = \sum_i \int_0^{4\pi} I(\mathbf{r}, \hat{\mathbf{s}}) d\Omega \quad (2.8)$$

The particle absorption and scattering coefficients of the particles in equation 2.5 were computed as:

$$k_p = \lim_{V \rightarrow 0} \sum_N \varepsilon_{pn} \frac{A_{pn}}{V} = \lim_{V \rightarrow 0} \sum_N Q_{abs} \frac{A_{pn}}{V} \quad (2.9)$$

$$\sigma_p = \lim_{V \rightarrow 0} \sum_N (1 - \varepsilon_{pn})(1 - f_{pn}) \frac{A_{pn}}{V} = \lim_{V \rightarrow 0} \sum_N Q_{scat} \frac{A_{pn}}{V} \quad (2.10)$$

In equations 2.9 and 2.10, the summation is over N particles within the control volume V , ε_{pn} is the particle emissivity, A_{pn} is the projected area of the n th particle, and f_{pn} is the scattering factor

associated with the n th particle. Q_{abs} and Q_{scat} correspond to the absorption and scattering efficiencies, respectively.

In this thesis, Q_{abs} and Q_{scat} were assumed to vary as the combusting particle transitions from the parent fuel to char to an ash particle. This variation is shown in Table 2.3. The variation in the coal radiative properties is according to Kuehlert [82]. These values indicate that the effective “extinction efficiency factors” are in the range 1.75 to 2.43 which compares well with the effective extinction factors reported by Menguc” et al. [83] for different sized particles.

In order to avail computational savings, the radiation calculations were performed once every 20 fluid/energy iterations. This approach has no bearing on the final results reported in this thesis and is justified by the fact that the radiation field does not change as rapidly between iterations as the fluid/temperature field. Furthermore, since the results reported in this study correspond to steady state calculations, the convergence in the radiation calculations was assessed at the end by ensuring radiative energy balance throughout the furnace. This was done by confirming that the volume integral of the radiative source term was equal to the surface integral of the net radiative flux through all the domain boundaries.

Table 2.3: Coal radiative property variations utilized in this thesis [51].

Coal	Absorption efficiency	Scattering efficiency	Scattering/absorption efficiency
Parent fuel	1.13	1.3	1.15
Char	0.59	1.5	2.54
Ash	0.05	1.7	34.00

CHAPTER 3

BACKGROUND: MULTIPHASE MODELING FRAMEWORKS

3.1. Dispersed, Multiphase Flows

Dispersed, multiphase flows occur when at least one phase in the form of particles, droplets, or bubbles is contained within a continuous carrier phase (liquid or gas). In this thesis, the dispersed, multiphase flow under investigation is a particle phase (the fuel) laden in the continuous carrier phase (the oxidizing gas mixture). There are two approaches to model these types of flows: a Euler-Euler approach and a Euler-Lagrange approach. This thesis examined two oxy-coal combustion studies from both approaches. A detailed explanation of these approaches is contained within the following sections.

3.1.1 Lagrangian Tracking

3.1.1.1 Overview

Lagrangian tracking (discrete phase model or DPM) was originally developed by Smoot and Smith 1985 [84]. ANSYS Fluent follows a Euler-Lagrange approach for this tracking procedure. In this approach, the fluid phase is treated as a continuum by approximating the solution to the Navier-Stokes equations while a discrete phase is tracked in the Lagrangian frame of reference throughout the calculated flow field [78]. Additionally, the particle dispersion is determined by turbulent velocity fluctuations. It is worth noting that the Lagrangian approach is closely related to the MPPIC-TFM framework in MFiX [85] when accounting for inter-particle collisions and becomes the TFM-DEM approach when individual particles are resolved. A detailed explanation of the general equations used to model the continuum and discrete phase is contained below.

3.1.1.2 Conservation of Mass for Continuous Phase

The conservation of mass (continuity equation) for the fluid phase, which describes the time rate of change of density at a specific point in space, is as follows [78]:

$$\frac{\partial \rho}{\partial t} + \nabla \cdot (\rho \vec{v}) = S_m \quad (3.1)$$

where ρ is the fluid density, $\rho \vec{v}$ is a mass flux vector, and S_m is a source term to represent the mass added to the continuous phase from the dispersed second phase (i.e. oxidation of carbon into carbon monoxide).

3.1.1.3 Conservation of Momentum for Continuous Phase

The conservation of momentum for the fluid phase, which describes the motion of species in the continuum, is as follows [78]:

$$\frac{\partial}{\partial t} (\rho \vec{v}) + \nabla \cdot (\rho \vec{v} \vec{v}) = -\nabla p + \nabla \cdot (\vec{\tau}) + \rho \vec{g} + \vec{F} \quad (3.2)$$

where the first term on the left-hand side of the equation is the rate of change in momentum per unit volume, the second term on the left-hand side of the equation is the rate of momentum addition by convection per unit volume, the second term on the right-hand side of the equation is the rate of momentum addition by molecular transport per unit volume where $\vec{\tau}$ is the stress tensor (described below), p is the static pressure, and $\rho \vec{g}$ and \vec{F} are the gravitational body force and external body force, respectively. The \vec{F} term can also contain either model-dependent or user-defined source terms [78]. The stress tensor is given by the following [78]:

$$\vec{\tau} = \mu \left[(\nabla \vec{v} + \nabla \vec{v}^T) - \frac{2}{3} \nabla \cdot \vec{v} I \right] \quad (3.3)$$

where μ is the molecular viscosity, I is the unit tensor, and the second term on the right hand side is the effect of volume dilation.

Under 2D axisymmetric geometry conditions, the $\nabla \cdot \vec{v}$ term can be given as follows [78]:

$$\nabla \cdot \vec{v} = \frac{\partial v_x}{\partial x} + \frac{\partial v_r}{\partial r} + \frac{v_r}{r} \quad (3.4)$$

3.1.1.4 Conservation of Species Mass for Continuous Phase

The conservation of mass for a chemical species in the fluid phase is given as follows [78]:

$$\frac{\partial}{\partial t}(\rho Y_i) + \nabla \cdot (\rho \vec{v} Y_i) = -\nabla \cdot \bar{J}_i + R_i + S_i \quad (3.5)$$

where the first term on the left-hand side of the equation is the rate of change in moles of species i per unit volume, the second term on the left-hand side of the equation is the species transfer due to convection, the first term on the right-hand side of the equation is the species transfer due to diffusion, R_i is the net rate of production of species i by chemical reaction, and S_i is a source term that includes the rate of creation by addition from the disperse phase and any user-define sources. The chemical species equation will be solved for $N - 1$ species where N is the number of species [78].

3.1.1.5 Conservation of Energy for Continuous Phase

The conservation of energy for the fluid phase, in terms of temperature, is as follows [78]:

$$\frac{\partial}{\partial t}(\rho E) + \nabla \cdot (\vec{v}(\rho E + p)) = \nabla \cdot \left(k_{eff} \nabla T - \sum_j h_j \bar{J}_j + (\vec{\tau}_{eff} \cdot \vec{v}) \right) + S_h \quad (3.6)$$

where the first term on the left-hand side of the equation is the rate of change in energy per unit volume, the second term on the left-hand side of the equation is the energy transfer due to convection, k_{eff} is the effective conductivity ($k + k_t$, where k_t is the turbulent thermal conductivity), \bar{J}_j is the diffusion flux of species j , $k_{eff} \nabla T$ is the energy transfer due to conduction, $\sum_j h_j \bar{J}_j$ is the energy transfer due to species diffusion, $(\vec{\tau}_{eff} \cdot \vec{v})$ is the energy transfer due to viscous dissipation, and S_h is a source term that includes the heat of chemical reaction and any other user-define volumetric heat sources.

E is given by the following [78]:

$$E = h - \frac{p}{\rho} + \frac{u^2}{2} \quad (3.7)$$

where h is the sensible enthalpy defined for ideal gases by the following [78]:

$$h = \sum_j Y_j h_j \quad (3.8)$$

and where Y_j is the mass fraction of species j and h_j is given by the following [78]:

$$h_j = \int_{T_{ref}}^T c_{p,j} dT \quad (3.9)$$

where T is temperature, T_{ref} is 298.15 K (for pressure-based solving), and $c_{p,j}$ is the heat capacity of species j .

3.1.1.6 Governing Equations for Discrete Phase

The discrete phase considers both continuum-particle and particle-particle interactions. Essentially, ANSYS Fluent computes the trajectories, the heat transfer to/from, and the mass transfer to/from the discrete phase entities [86].

Discrete phase trajectory in a Lagrangian framework includes discrete phase inertia, hydrodynamic drag, and the force of gravity as shown in equation 3.10 [78]:

$$\frac{d\bar{u}_p}{dt} = F_D(\bar{u} - \bar{u}_p) + \frac{\bar{g}(\rho_p - \rho)}{\rho_p} + \bar{F} \quad (3.10)$$

where \bar{F} is an additional acceleration term, the $F_D(\bar{u} - \bar{u}_p)$ term is the drag force per unit particle mass and F_D is calculated by equation 3.11 [78]:

$$F_D = \frac{18\mu}{\rho_p d_p^2} \frac{C_D Re}{24} \quad (3.11)$$

Here, \bar{u} is the fluid phase velocity, \bar{u}_p is the particle velocity, μ is the molecular viscosity of the fluid, ρ is the fluid density, ρ_p is the particle density, and d_p is the particle diameter. The Reynolds number (Re) is defined by equation 3.12 [78]:

$$Re \equiv \frac{\rho d_p |\bar{u}_p - \bar{u}|}{\mu} \quad (3.12)$$

For modeling the heat and mass transfer of the discrete phase, ANSYS Fluent uses four heat and mass transfer relationships (or laws): inert heating, inert cooling, devolatilization, and surface combustion [78]. The inert heating law is applied when the particle temperature is less than the vaporization temperature while the inert cooling law is applied after the volatile fraction of the particle has been consumed [78]. When using either of these laws, ANSYS fluent utilizes a simplified heat balance to relate the particle temperature $T_p(t)$ to the convective heat transfer and the absorption/emission of radiation at the particle surface as shown in equation 3.13 [78]:

$$m_p c_p \frac{dT_p}{dt} = h A_p (T_\infty - T_p) + \varepsilon_p A_p \sigma_{SB} (\theta_R^4 - T_p^4) \quad (3.13)$$

where m_p is the mass of the particle, c_p is the heat capacity of the particle, h is the convective heat transfer coefficient, A_p is the surface area of the particle, T_∞ is the local temperature of the continuous phase, ε_p is the particle emissivity, σ_{SB} is the Stefan-Boltzmann constant ($5.67 \cdot 10^{-8}$ W/m²·K⁴), and θ_p is the radiation temperature.

In using this simplified heat balance, two assumptions are made: the particle has a uniform temperature throughout and there is a negligible internal resistance to heat transfer.

3.1.1.7 Advantages/Disadvantages of Lagrangian Tracking

The Lagrangian tracking approach has both advantages and disadvantages. The advantages of this approach are that: polydispersity can be easily integrated since the sizes of particles are independent and there is no fundamental limitation on the Stokes number due to the requirement of unique particle velocity and temperature field representations [87]. The shortcomings of the Lagrangian approach are the: difficulties to model coagulation and break-up, change the PSD, low parallelization efficiencies and isotropic turbulence assumption for the particles near the walls.

Furthermore, the Lagrangian tracking approach can be a significant bottleneck in large-scale simulations.

3.1.2 *Two-Fluid Model*

3.1.2.1 *Overview*

The second Euler-Euler modelling approach presented is the two-fluid model (or TFM). This model was utilized in all oxy-fuel combustion scenarios investigated in the work documented in this thesis. Developed by Zhou 1988 and Guo et al. 1998, this model applies comprehensive Eulerian treatments for both the gas and particle phases, again, treating the phases as interpenetrating continua [88-90]. In the TFM framework, the inter-particle collisions and the dispersion of particles are determined by the Kinetic theory of granular flow. Here the frictional stresses are modeled by neglecting the turbulence at the particle level. It is important to note that turbulence modeling may be inaccurate for swirling flows (per-phase versus dispersed phase). Velocity and temperature slips between the particle phase and gas phase are found by solving the momentum and energy equations for both phases [88]. Additionally, a continuity equation is solved for each phase.

Equations of conservation shown below are shown in terms of the q^{th} phase (where the q^{th} phase can be either the particle or gaseous phase).

3.1.2.2 *Conservation of Mass*

The mass conservation equation for the q^{th} phase is as follows [78]:

$$\frac{\partial}{\partial t} (\alpha_q \rho_q) + \nabla \cdot (\alpha_q \rho_q \vec{v}_q) = \sum_{p=1}^n \dot{m}_{kq} - \dot{m}_{qk} + S_q \quad (3.23)$$

where \vec{v}_q is the phase velocity of phase q, \dot{m}_{kq} characterizes the mass transfer from the k^{th} to q^{th} phase, \dot{m}_{qk} characterizes the mass transfer from the q^{th} to k^{th} phase, and S_q is a source term.

3.1.2.3 Conservation of Momentum

The momentum conservation equation for the q^{th} phase is as follows [78]:

$$\begin{aligned} \frac{\partial}{\partial t}(\alpha_q \rho_q \vec{v}_q) + \nabla \cdot (\alpha_q \rho_q \vec{v}_q \vec{v}_q) = & \quad (3.24) \\ -\alpha_q \nabla p + \nabla \cdot \vec{\tau}_q + \alpha_q \rho_q \bar{g} + \sum_{p=1}^n (\bar{R}_{kq} + \dot{m}_{kq} \vec{v}_{kq} - \dot{m}_{qk} \vec{v}_{qk}) + \vec{F} \end{aligned}$$

where $\vec{\tau}_q$ is the q^{th} phase stress-strain tensor defined by equation 3.25:

$$\vec{\tau}_q = \alpha_q \mu_q (\nabla \vec{v}_q + \nabla \vec{v}_q^T) + \alpha_q \left(\lambda_q - \frac{2}{3} \mu_q \right) \nabla \cdot \vec{v}_q I \quad (3.25)$$

Here, μ_q is the shear viscosity of the q^{th} phase, λ_q is the bulk viscosity of the q^{th} phase, \vec{F} is the sum of various forces acting on the q^{th} phase (external body forces, lift force, wall lubrication force, virtual mass force, turbulent dispersion force), \bar{R}_{kq} is the interaction force between phases, and p is the pressure observed by all phases.

3.1.2.4 Conservation of Energy

The energy conservation equation for the q^{th} phase is as follows [78]:

$$\begin{aligned} \frac{\partial}{\partial t}(\alpha_q \rho_q h_q) + \nabla \cdot (\alpha_q \rho_q \bar{u}_q h_q) = & \quad (3.26) \\ \alpha_q \frac{\partial p_q}{\partial t} + \vec{\tau}_q : \nabla \bar{u}_q - \nabla \cdot \bar{q}_q + S_q \sum_{p=1}^n (Q_{kq} + \dot{m}_{kq} h_{kq} - \dot{m}_{qk} h_{qk}) \end{aligned}$$

where h_q is the specific enthalpy of the q^{th} phase, \bar{q}_q is the heat flux, S_q is a source term (sources of enthalpy), Q_{kq} is the intensity of heat exchange between the k^{th} and q^{th} phases, h_{kq} is an interphase enthalpy term.

3.1.2.5 Drag Law

Interphase exchange coefficients can be included to indicate the momentum exchange between the particulate and gaseous phases. In the work documented by this thesis, the Morsi and

Alexander model was chosen to model the solid-fluid drag interactions. The model is as follows [78]:

$$f = \frac{C_D Re}{24} \quad (3.27)$$

where C_D is the function defined below:

$$C_D = a_1 + \frac{a_2}{Re} + \frac{a_3}{Re^2} \quad (3.28)$$

Here, the coefficients a_1 , a_2 , and a_3 have an adjusting function definition over a large range of Reynolds numbers.

3.1.2.6 Advantages/Disadvantages of Two-Fluid Model

The two-fluid model approach has both advantages and disadvantages. The TFM frameworks can efficiently describe all particle history effects: particle mass change due to moisture evaporation, devolatilization, char combustion, particle temperature changes due to convection, and diffusion and heat transfer between the two phases [88]. The two inherent problems in the TFM framework are: particle dispersion due to turbulence and the need to obtain individual particle time-histories. Additionally, Eulerian approaches like the TFM are generally more computationally expensive, especially for polydisperse systems with a wide range of particle sizes [87].

CHAPTER 4

NON-SWIRLING OXY-COAL FLAMES

4.1. Problem Overview and Methods

Flame stability is often measured by the flame stand-off distance which is defined by the distance from the tip of the burner to the ignition position. Flame attachment is defined when this distance equals zero. There are two methods widely used in field boilers today to identify flame ignition positions [91]. First, ignition can be assumed to occur where the temperature (specifically particulate temperature) greatly increases. In the oxidizing environment, particle ignition is determined by heat generation/loss from the particle surface [91]. Factors that play an important role in this heat balance include the heat transfer from the ambient gas, radiative heat transfer from the chamber's walls, heat generated by chemical reaction, and heat loss when the temperature of the particles is higher than the ambient gas and boiler walls [91]. More specifically, the particle ignition is controlled by the following physical and chemical processes: rate of diffusion of gaseous fuel and oxidizer species, coal pyrolysis, diffusion of gaseous products and oxidizer species, and gas phase reaction of pyrolysis products and oxygen [91]. Secondly, ignition can be assumed where CO concentration greatly increases as CO is a direct product of heterogeneous reactions.

Flame stabilization, here defined by stand-off distance, plays an important role in controlling NOX and CO₂ emissions. By controlling flame stability, controlling NOX emissions becomes easier as it increases the size of the fuel-rich flame region where NOX is reduced to nitrogen [92]. Furthermore, flame stability can affect the heat transfer performance of coal thermal power plants [93].

Flame stability measurements were taken in a 40 kW downflow laboratory combustor (oxy-fuel combustor or OFC) by J. Zhang et al. using optical measurements of the flame stand-off distance [94]. They suggested, based on their experimental results, that flame stability is affected by the primary jet O₂ concentration, secondary jet fluid preheat temperature, secondary jet O₂ concentration, and the gaseous diluent choice: CO₂ versus N₂ (here, the pulverized coal is injected into the primary jet stream where the secondary jet stream is a separate oxidizer stream) [94].

Previous attempts to model the oxy-fuel combustion environment in this combustor have been documented [93, 95]. G. Babak et al. used a Eulerian formulation of the one-dimensional turbulence (ODT) model to determine flame stand-off distance by means of detailed kinetic calculations of the gas phase fully coupled to a high-fidelity model (CPD) for devolatilization of coal particles [95]. Their results showed a quantitative agreement with experimental data. They suggested that there may be a kinetic limitation to stand-off distance and that radiative temperature significantly influenced the stand-off distance [95]. Pedel et al. used a large eddy simulation (LES) tool, ARCHES, for modeling combustion [93]. They evaluated the impact of heterogeneous reactions, radiation, primary stream temperature, and wall temperature on flame stability. Their simulations were consistent with the experimental data. Also, their analysis suggests that the flame stand-off distance is mainly controlled by the wall temperature and that the role of primary O₂ is minor [93].

In lieu of these two studies, our motivation for studying flame stand-off using different multiphase modeling frameworks was two-fold: First, it enabled us to investigate the efficacies of the different multiphase modeling frameworks in the absence of significant particle dispersion (these are non-swirling flames), thereby eliminating any prediction variations due to differences in the particle turbulence modeling predictions between the different frameworks. Second, since

radiative heat transfer is expected to play a key role in flame stand-off, this could be investigated more closely in the present study since the Lagrangian approach utilizes an optically thin particle radiation model whereas the Eulerian approaches account for particle radiation more rigorously.

In our attempt to model this system, CFD simulations were carried out for two non-swirling oxy-coal combustion scenarios using the ANSYS Fluent 16.2 commercial software package [78]. The two oxy-fuel combustion scenarios differ only by the concentration of oxygen in the primary burner (0 vol% O₂ and 20.9 vol% O₂, respectively). Simulations for each scenario were run and can be broken into three groups categorized by the framework choice (DPM and TFM). For each framework, a Rosin-Rammler distribution was utilized for the solid phase. Additional simulations with varying particle sizes were carried out to help assess flame stability characteristics.

The experimental oxy-fuel combustion stand-off study was carried out by Zhang et al in the OFC shown in Figure 4.1 (used with permission) [94]. The OFC design allows self-sustained combustion with residence time-temperature histories, gas species and particle concentrations all representative of practical units, while still maintaining sufficient control to allow well defined, systematic experimentation in controlled environments [94]. The OFC is rated at 100 kW and measures 3.8 meters in length. There is a primary and secondary oxidizer inlet with a coal feeder on the primary inlet.

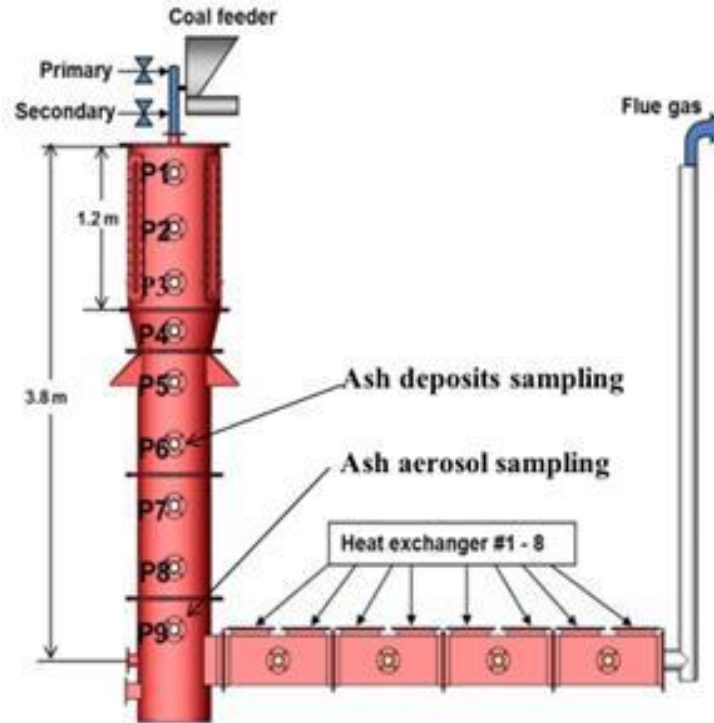


Figure 4.1: Utah's experimental oxy-fuel combustor (OFC).

A 2D, axisymmetric geometry was built in ANSYS Workbench to the specifications of the OFC as shown in Figure 4.2. The length of this geometry was 4.07 meters. The length and width of the ignition zone were 2.2 meters and 0.61 meters, respectively. The length and width of the radiation zone were 1.6 meters and 0.27 meters, respectively. The geometry was populated with 8,144 cells and had a maximum skewness value of 0.667. The results were found to be invariant with any further refinement to the grid.

Thermal boundary conditions were set for the walls in the ignition and radiation zone (also shown in Figure 4.2). The ignition zone walls were set to a temperature of 1283 K. The radiation zone walls were set to a heat transfer coefficient of $5 \text{ W/m}^2\text{-K}$ with a surrounding fluid temperature of 300 K. Figure 4.3 shows the wall temperature profile along the ignition zone wall and radiation zone wall.

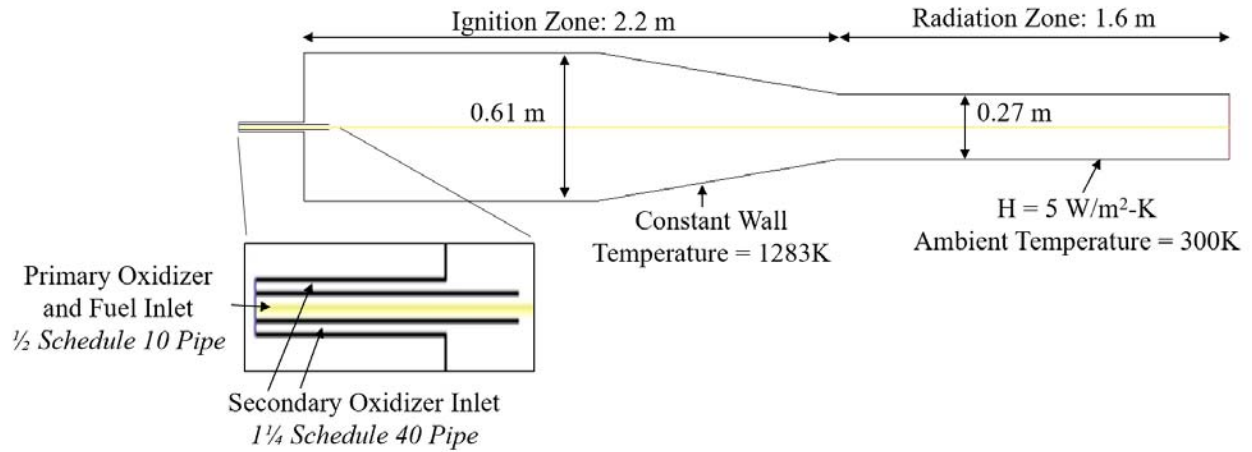


Figure 4.2: 2D, axisymmetric geometry designed to replicate Utah's experimental OFC.

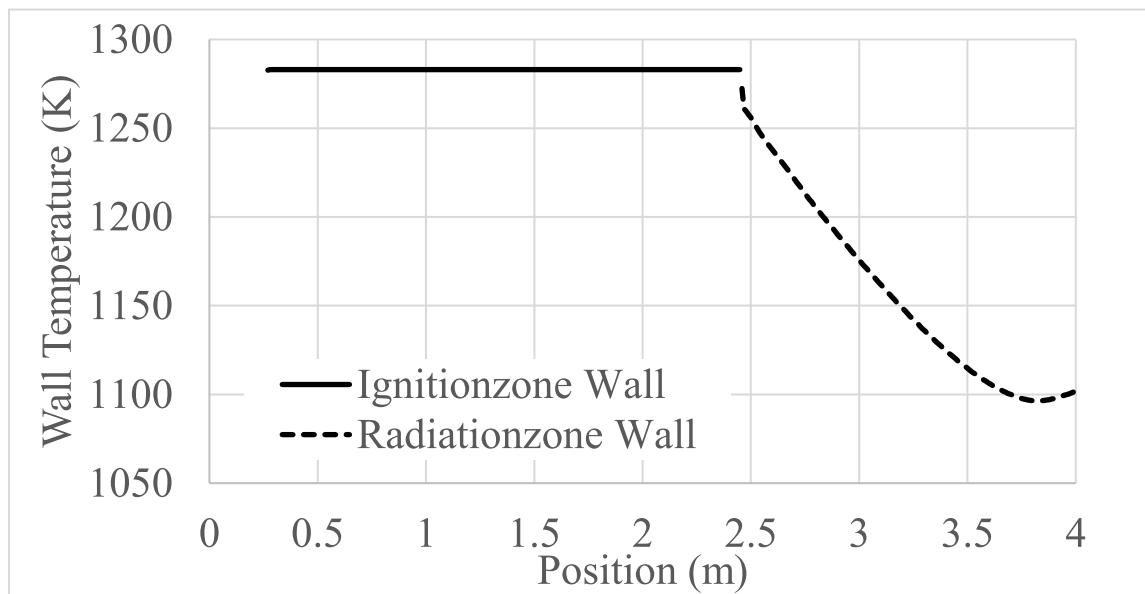


Figure 4.3: Simulated wall temperature profile in the furnace in the non-swirling study.

An Utah Bituminous coal was used as the fuel for oxy-fuel combustion. Table 4.1 contains the proximate and ultimate analysis for this coal.

Table 4.1: Proximate and ultimate analysis of the Utah Bituminous coal.

Proximate Analysis (wt.%)		Element Analysis (wt.%)	
Fixed Carbon	46.44	C	77.75
Volatiles	38.81	H	5.03
Ash	11.72	N	1.44
Moisture	3.03	S	0.45
HHV(kJ/kg)	27,286	O	15.33

Particle size distribution model at the injection point was based on the Rosin-Rammler distribution shown in Figure 4.4 [91].

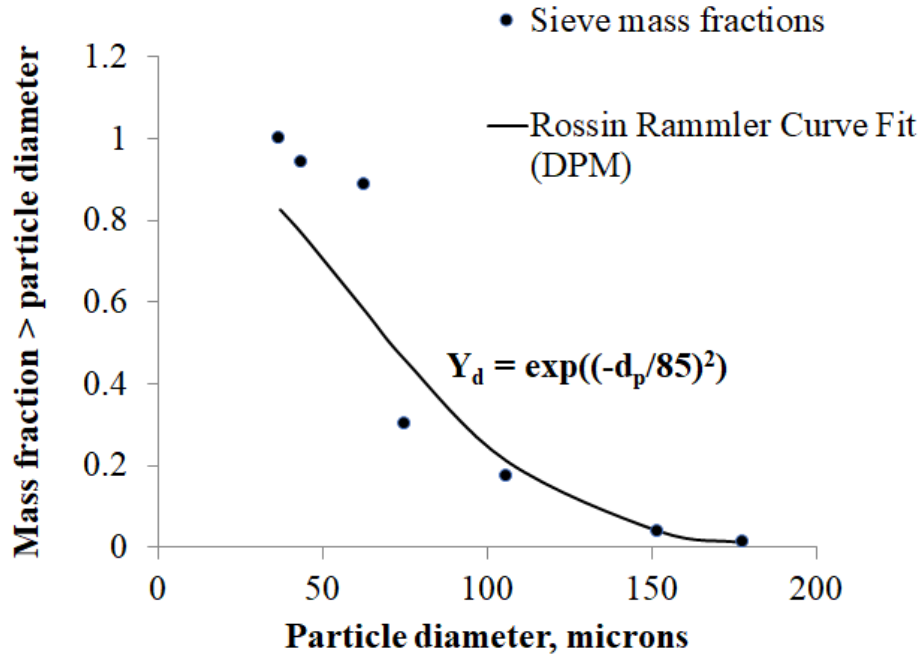


Figure 4.4: Coal particle size distribution and Rosin-Rammler curve fit for parent coal particles in the non-swirling study.

Table 4.2 shows primary and secondary oxidizer stream specifications obtained from the University of Utah that were employed in the simulations to recreate experimental trials.

Table 4.2: Primary and secondary oxidizer stream specifications for both non-swirling combustion scenarios.

	0% O ₂	20.9% O ₂
<i>Velocity Magnitude (m/s)</i>		
Primary	5.40	5.40
Secondary	16.6	16.6
<i>Mass Flow Rate (kg/s)</i>		
Fuel	0.00134	0.00134
<i>Inlet gas temperature (K)</i>		
Primary	305	305
Secondary	544	544
<i>Species concentration of primary inlet (mol%)</i>		
O ₂	0	20.9
H ₂ O	0	0
CO ₂	100	79.1
N ₂	0	0
<i>Species concentration of secondary inlet (mol%)</i>		
O ₂	48.9	44.7
H ₂ O	0	0
CO ₂	51.1	55.3
N ₂	0	0

The single-rate model was chosen to model devolatilization. This model assumes that the rate of devolatilization is first-order with respect to the volatiles [96]. The devolatilization kinetic rate, k , is defined by input of an Arrhenius type pre-exponential factor, A_1 , and an activation energy, E , as shown below [78]:

$$k = A_1 e^{-(E/R_g T)} \quad (4.1)$$

where R_g is the universal gas constant and T is temperature.

After release of the volatiles during the volatile pyrolysis process, the remaining char reacts with the surrounding gas phase. User-defined functions were implemented to model the diffusional and kinetic resistances associated with the heterogeneous char oxidation. Gaseous combustion

between the fuel volatiles and oxidant was simulated using a two-step mechanism. Initially, volatiles were assumed to oxidize and release CO. Then, CO was oxidized to CO₂. The heterogenous and homogenous reactions modeled in these studies are contained in Table 4.3.

Table 4.3: A summary of reactions and kinetic parameters modeled in the non-swirling study.

	A	Ea, J/kmol	Reference
Heterogeneous reactions			
Devolatilization	382000*	7.4e+07	[97]
Char combustion: $2C_s + O_2 \rightarrow 2CO$	0.86**	1.13e+08	[98]
Homogeneous reactions			
Volatile combustion: $vol \rightarrow 1.05CO + 1.96H_2O + 0.0283N_2 + 0.0082SO_2$	2.119e+11*	2.027e+08	[99]
CO oxidation: $2CO + O_2 \rightarrow 2CO_2$	2.239e+12*	1.7e+08	[100]
<i>Pre-exponential factor, A, units: *(1/s) / **(kg/m² s Pa)</i>			

Table 4.4 provides a complete summary of the different modeling options invoked in this study. Interphase interaction terms were modeled employing identical phenomenological laws in all three frameworks. Additionally, non-gray effects of gas radiation and the variations in the radiative properties of the solid phase during combustion were implemented as user-defined functions.

Table 4.4: A summary of modeling options invoked in the non-swirling study.

Physics being modeled	CFD Framework (ANSYS Fluent)
Multiphase hydrodynamics	DPM / TFM
Turbulence	Realizable k-epsilon
Coal devolatilization	Single-rate
Gas-phase chemistry	Finite rate/Eddy dissipation
Heterogenous chemistry	Surface Reactions
Drag law	Morsi-alexander
Radiation transport equation solver	Discrete ordinates method
Particle radiative property	Variable K_{abs} and K_{scat}
Particle scattering phase function	Anisotropic (forward scattering)
Gas-phase radiative property	Perry (5gg) [77]
Solver	Pressure-based

4.2. Results

4.2.1. *Inert Particle Simulations*

In order to ascertain that the same constitutive laws (associated with particle drag and heating) were being utilized in both DPM and TFM frameworks, simulations of inert (non-reacting) coal particles at the mean diameter associated with the Rosin-Rammler distribution (85 microns) were carried out first. Figure 4.5 shows the particle volume fraction and Figures 4.6 and 4.7, show the axial temperature and velocity profiles, respectively (for both phases) in the inert particle simulations carried out using the TFM and DPM frameworks. The close agreement between the profiles indicates that the phenomenological laws for drag and heating were indeed identical between the two frameworks. Figure 4.6c indicates that the gas and particle temperature equilibrate in the radiation zone of the combustor. Likewise, in Figure 4.7c, a uniform “slip velocity” between the particle and gas phase is seen to persist in the radiant zone.

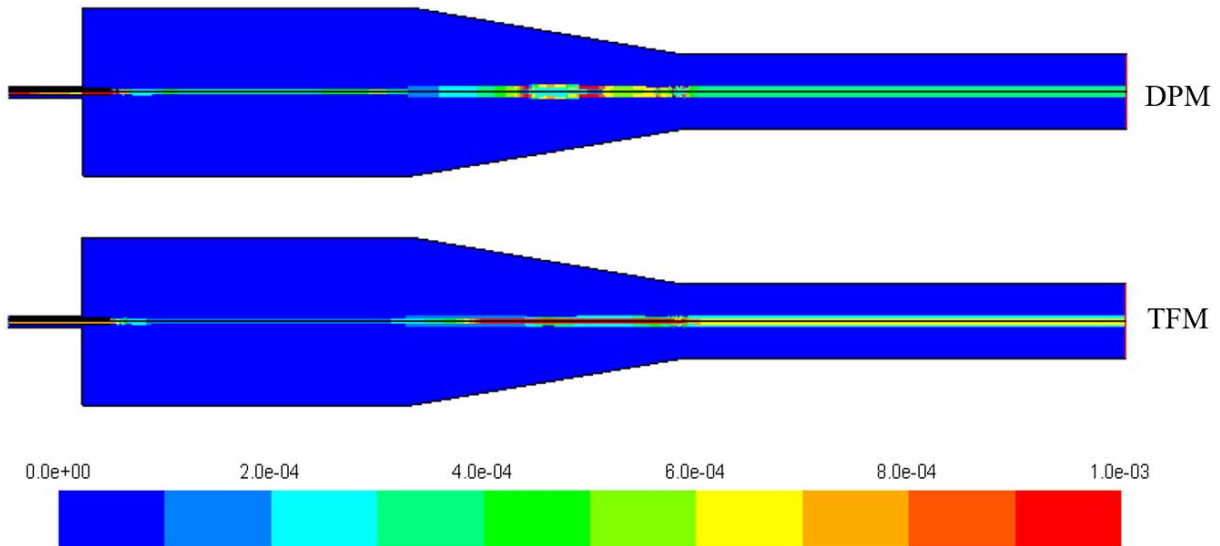
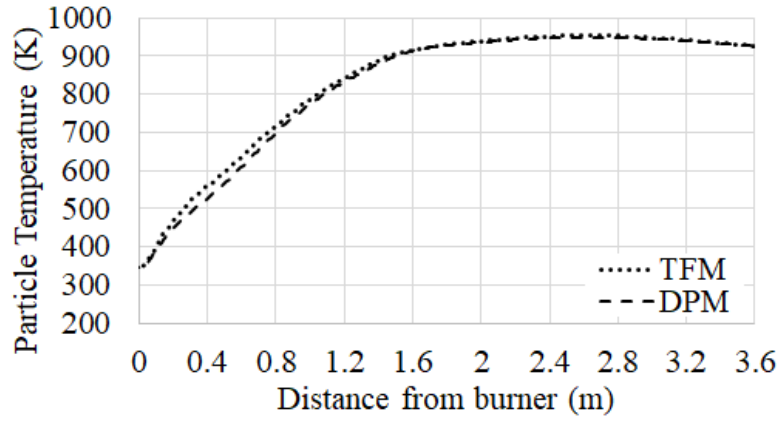
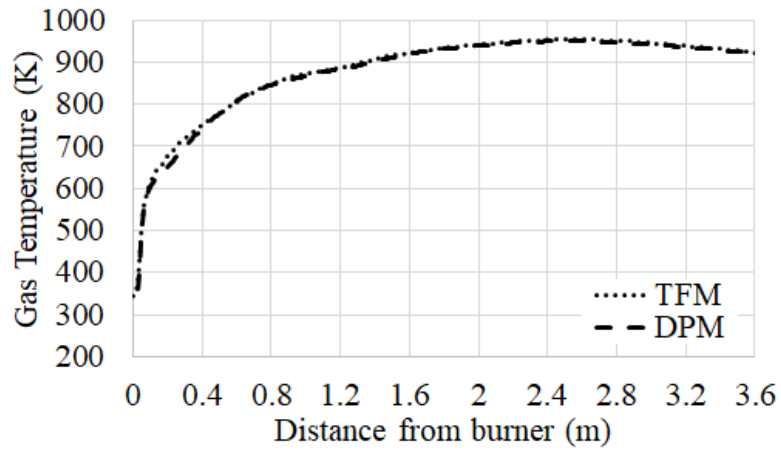


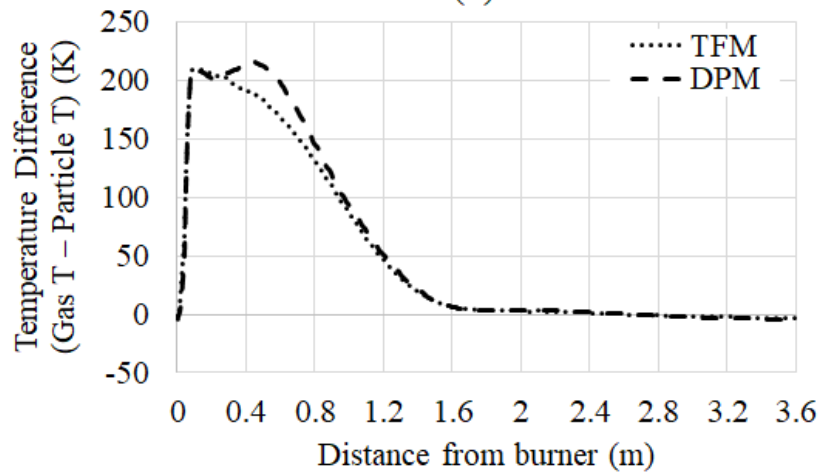
Figure 4.5: Particle volume fractions in the inert simulations of 85-micron particles using DPM and TFM modeling frameworks.



(a)

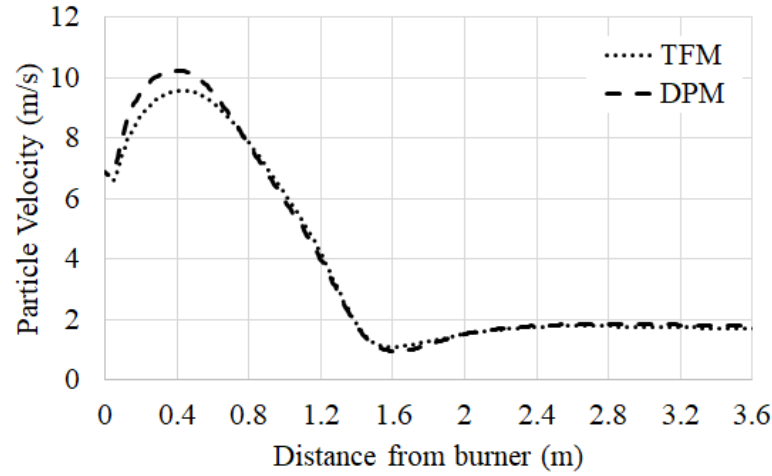


(b)

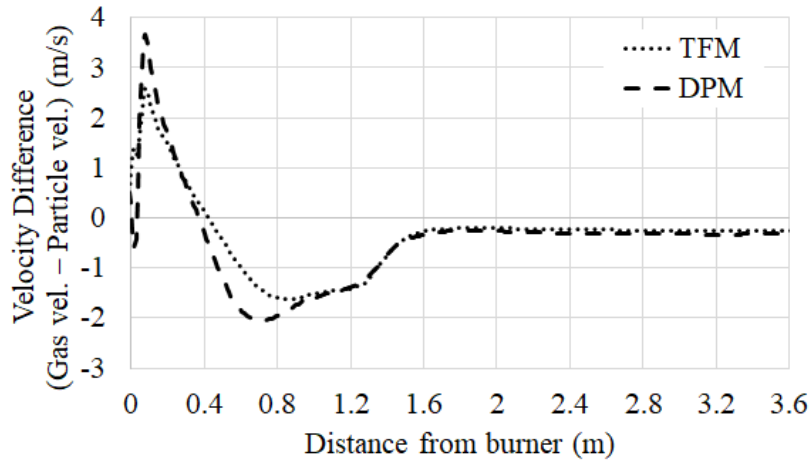


(c)

Figure 4.6: Axial temperature profiles in the non-swirling inert particle simulations: (a) Particle temperature; (b) Gas temperature; (c) Temperature difference (Gas temperature – Particle temperature).



(a)



(b)

Figure 4.7: Axial velocity profiles in the non-swirling inert particle simulations: (a) Particle velocity; (b) Velocity difference (Gas velocity – Particle velocity).

4.2.2. Flame Stand-off Predictions Using DPM Framework

To investigate the stand-off distances using the DPM framework, DPM simulations with a Rosin-Rammler particle size distribution were generated. Figure 4.8 shows the carbon monoxide mole fraction (a) and char burnout (b) in the DPM Rosin-Rammler simulations. Stand-off distances in these simulations were not accurately characterized as a function of oxygen concentration in the primary burner. Experimental measurements show the mean stand-off

distances for the 0% O₂ scenario to be 29.8 cm and the 20.9% O₂ scenario to be 11.9 cm (as denoted by the vertical lines in Figure 4.8). The distance between the burner tip and peak carbon monoxide concentration is approximately triple of what was observed in the experimental 0% O₂ scenario and nearly 8 times what was observed in the experimental 20.9% O₂ scenario. The shorter mean stand-off distances observed in the 20.9% O₂ scenario is likely due to the availability of oxygen in the primary burner. Char burnout is shown here to verify the ignition location.

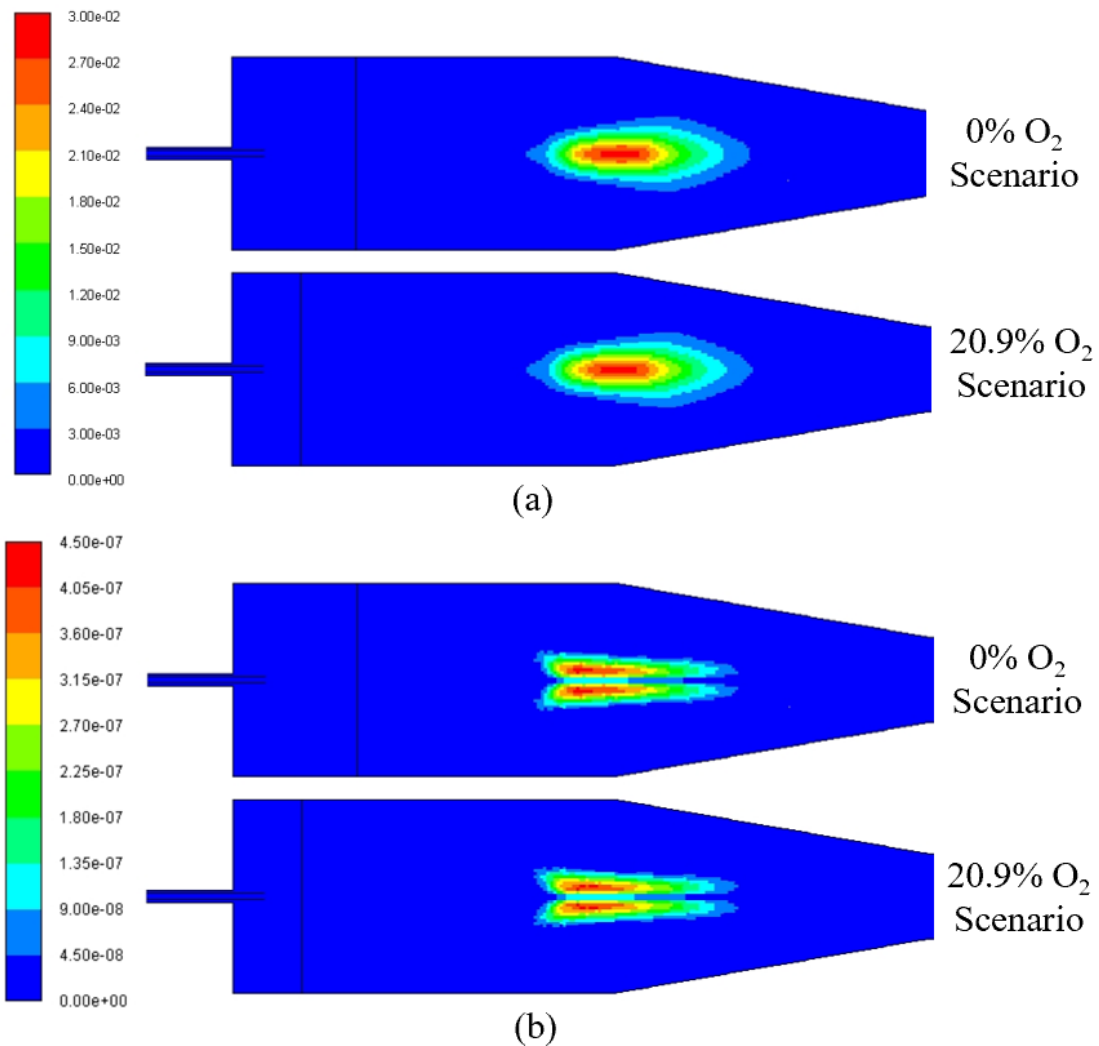


Figure 4.8: Carbon monoxide mole fraction (a) and char burnout (b) in the Rosin-Rammler DPM simulations for the non-swirling study. Mean experimentally measured stand-off distance locations are indicated by vertical line.

Intuitively, by injecting a smaller constant inlet coal particle diameter, combustion should occur closer to the burner. To investigate this, DPM simulations with a constant 35-micron particle size distribution were carried out. Figure 4.9 shows the carbon monoxide mole fraction (a) and char burnout (b) for the 35-micron DPM simulations. However, no improvement in stand-off distances were observed between the Rosin-Rammler and 35-micron diameter DPM simulations. Again, to verify the ignition location in the 35-micron diameter DPM simulations, char burnout contours were generated.

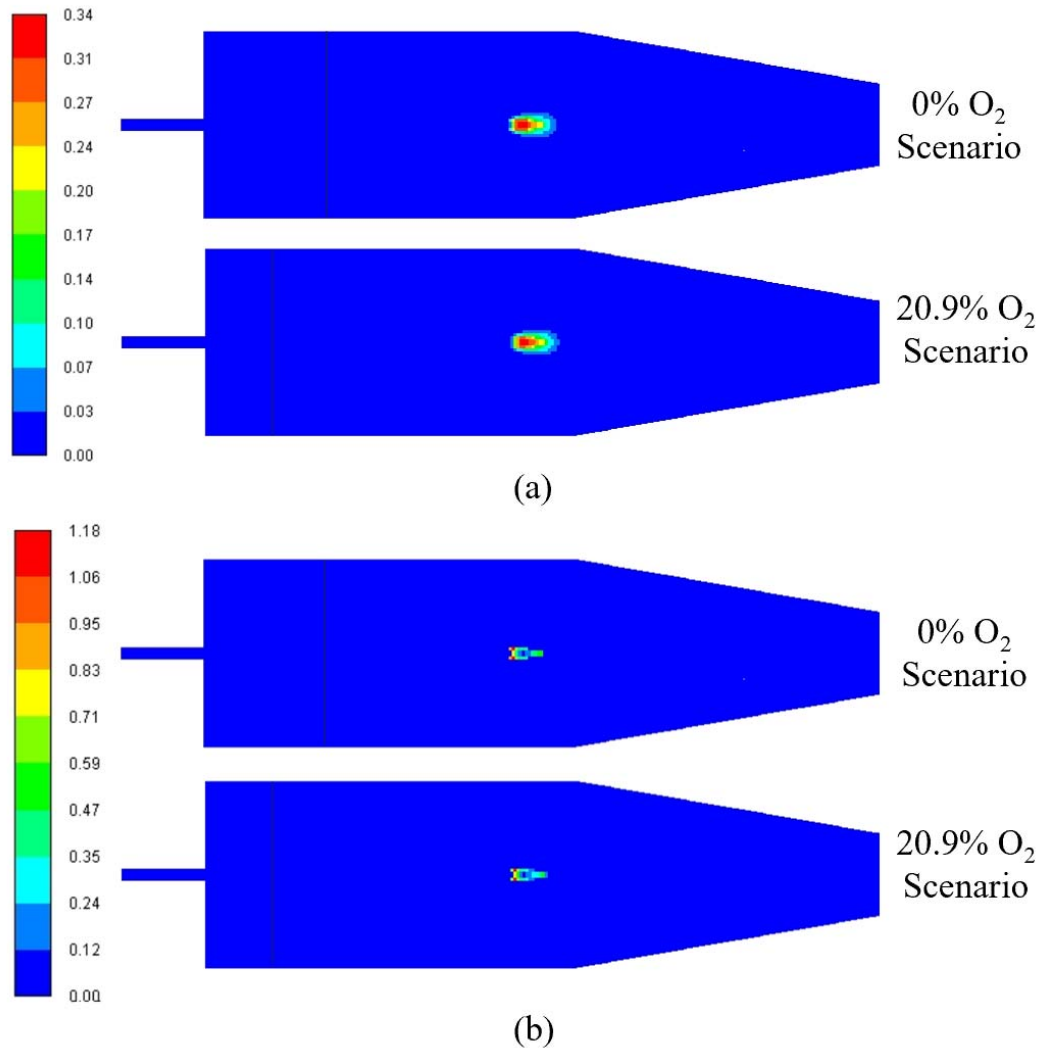


Figure 4.9: Carbon monoxide mole fraction (a) and char burnout (b) in the 35-micron DPM simulations for the non-swirling study. Mean experimentally measured stand-off distance locations indicated by vertical line.

4.2.3. Flame Stand-off Predictions Using TFM Framework

Contrary to the DPM simulations, simulations using the TFM framework were able to capture the experimentally observed trends in flame stand-off as a function of oxygen concentration in the primary burner. TFM simulations using a constant mean Rosin-Rammler distribution particle diameter of 85-microns were carried out. Figure 4.10 shows the carbon monoxide mole fraction (a) and char oxidation rate (b) in the 85-micron TFM simulation. The distance between the burner tip and the increase in CO is near to what was observed experimentally. In addition, the char oxidation rate was also examined for verification of ignition location.

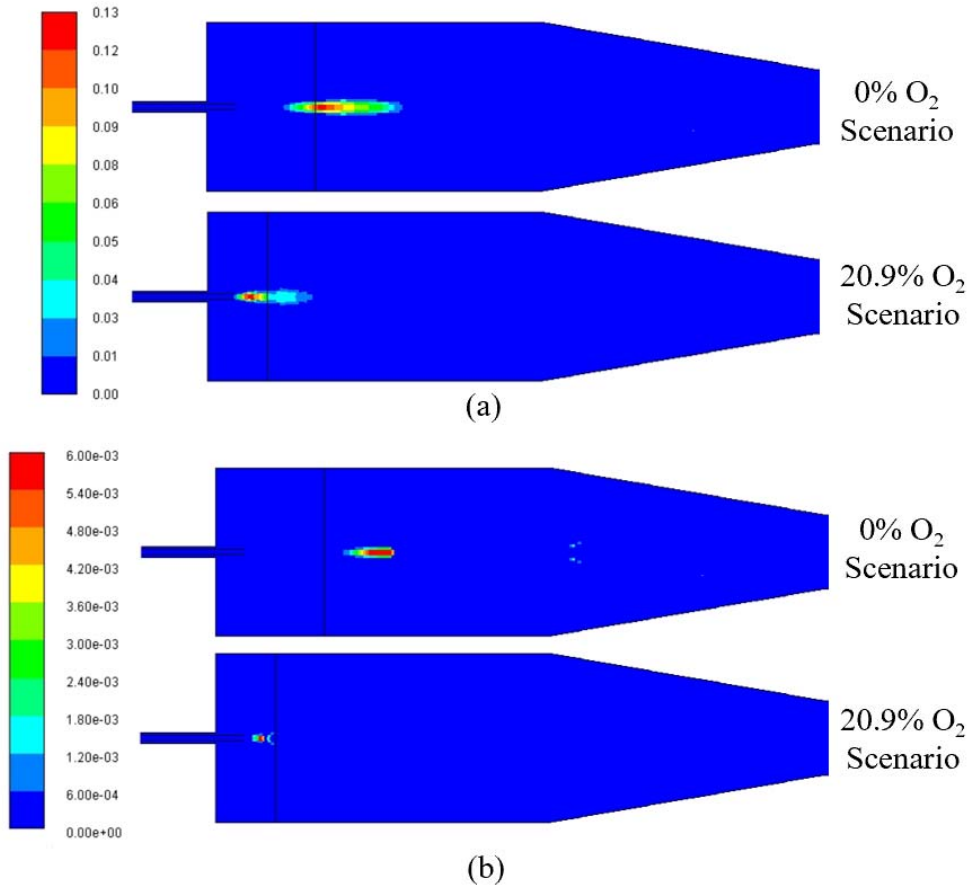


Figure 4.10: Carbon monoxide mole fraction (a) and char oxidation rate (kmol/m³-s) (b) in the 85-micron TFM simulations for the non-swirling study. Mean experimentally measured stand-off distance locations indicated by vertical line.

To investigate the effects of adding an additional particle phase, TFM simulations with two distinct particle sizes (100 microns and 50 microns) were carried out. Figure 4.11 shows the carbon monoxide mole fraction (a), char oxidation rate for the 0% O₂ scenario (b) and char oxidation rate for the 20.9% O₂ scenario (c) for the 2-phase TFM simulations. Again, the distance between the burner tip and the peak in carbon monoxide concentration is near what was observed experimentally. The char oxidation rate was also examined for verification of ignition location. This verification included examining rates of char oxidation for both phases (100 micron and 50 micron particulate phases).

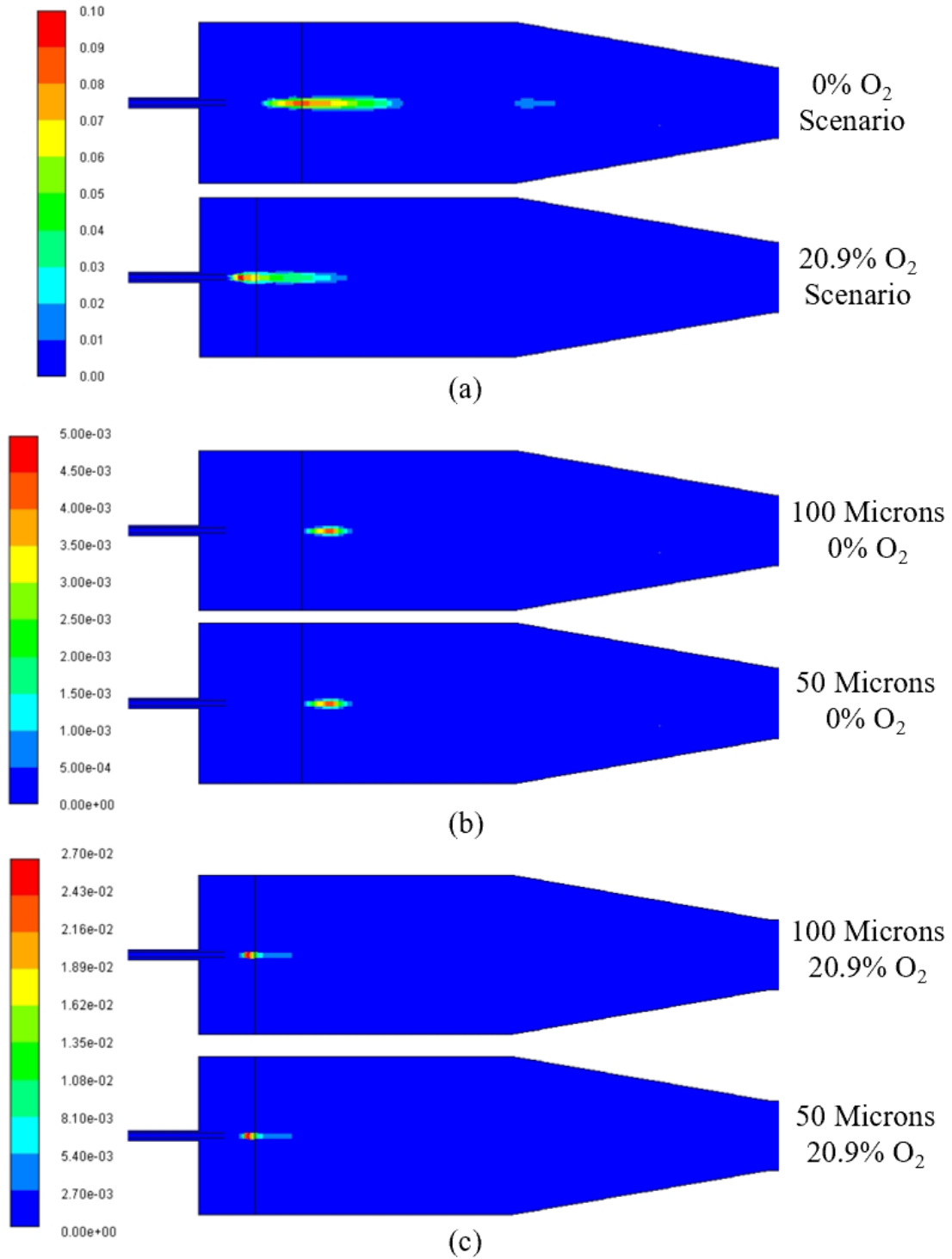
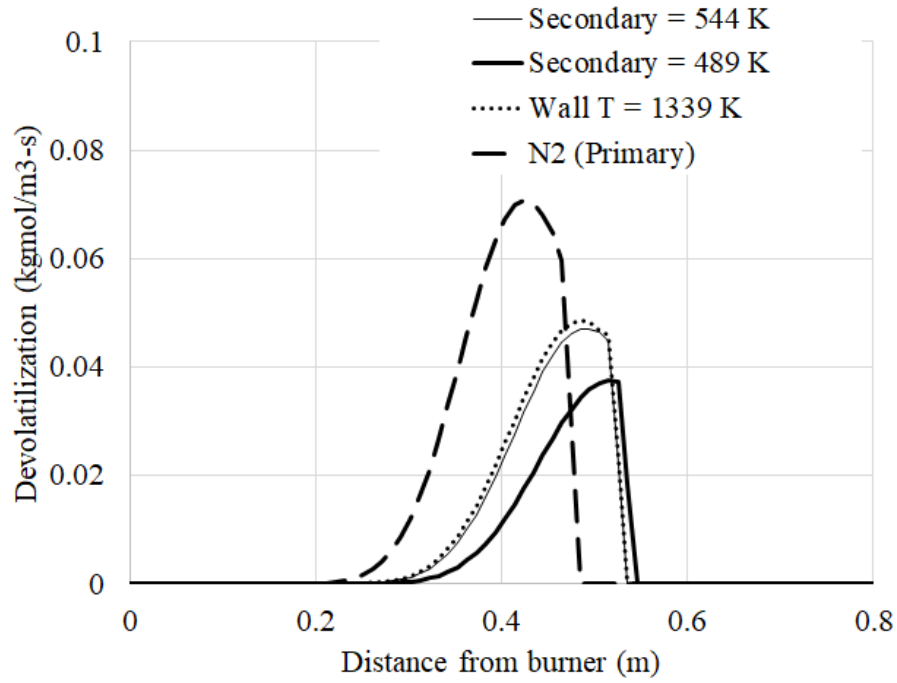


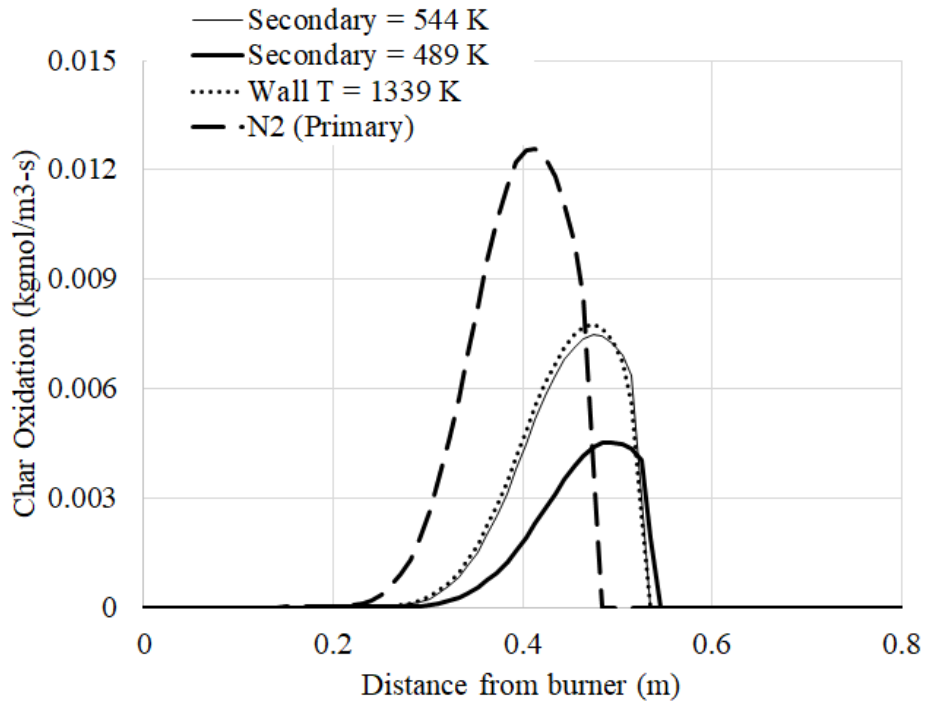
Figure 4.11: Carbon monoxide mole fraction (a), char oxidation rate (kmol/m³-s) for 0% O₂ scenario (b) and char oxidation rate (kmol/m³-s) for 20.9% O₂ scenario (c) in 2-phase TFM simulations for the non-swirling study. Mean experimentally measured stand-off distance locations indicated by vertical line.

4.2.4. Influence of Other Operational Parameters on Flame Stand-off

In addition to the effects of O₂ concentration in the primary burner on flame stand-off, Zhang [91] also experimentally investigated the effects on flame stand-off of: the secondary oxidizer temperature, the wall temperature and replacing the CO₂ in the primary burner with N₂. The most pronounced effect was observed due to CO₂ replacement with N₂ due to the differences in heat capacity of the two diluents. Lower secondary air temperatures also delayed the ignition. Both these effects appeared to increase the flame stand-off location by about 10 cm in a 14.4% O₂ flame. Given our ability to predict flame stand-off with reasonable fidelity using the TFM framework, additional simulations were carried out for the 14.4% O₂ flames. Figure 4.12 shows the devolatilization and char oxidation rates along the centerline axis during simulations of the 14.4% O₂ flames (under different operating conditions) using the TFM framework. These results are in excellent agreement with the experimental observations of Zhang [91].



(a)



(b)

Figure 4.12: (a) Devolatilization rate (kmol/m³-s) and (b) Char oxidation rate (kmol/m³-s) along the centerline axis during simulations of the 14.4% O₂ flames (under different operating conditions) simulated using the TFM framework.

4.2.5. *A Closer Examination of TFM and DPM Predictions*

Figure 4.13 shows the total heat release, ignition zone flux, and radiation zone flux across all Rosin-Rammler studies for both oxy-combustion scenarios. These fluxes are computed by summing the total heat transfer rate (convective and radiative heat transfer) over the respective faces of the boiler boundary. Radiation was the dominant mode of heat transfer with the radiant heat loss fraction (Radiative heat loss/Total chemical heat release) determined to be about 0.6 for both flames. The incident radiative flux predictions were in good agreement with measured values from similar flames in this furnace (between 120 - 150 kW/m² in the ignition zone) [101]. Figure 4.13b shows that radiation from the participating gases accounted for 75% of the radiative heat transfer.

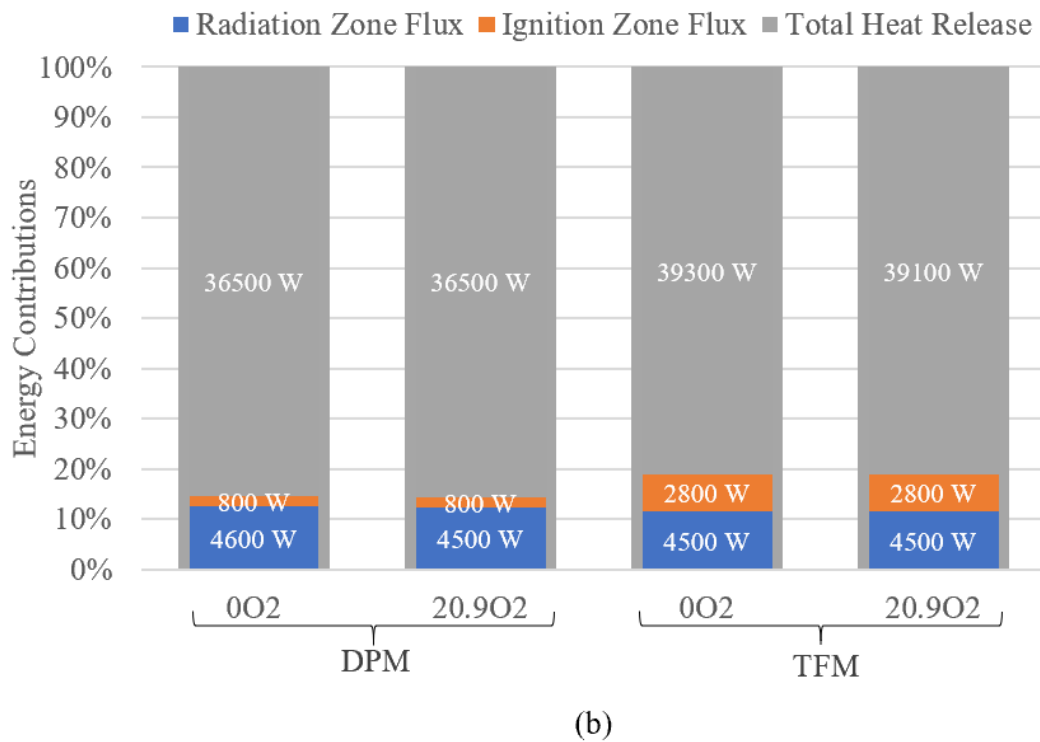
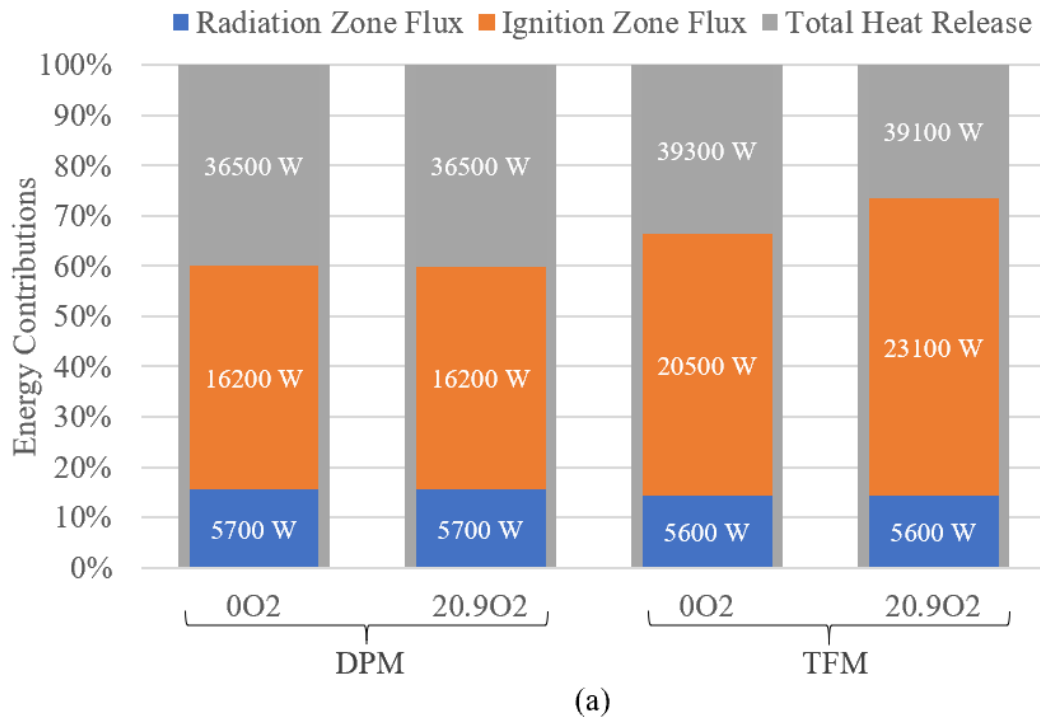


Figure 4.13: The fraction of total flux attributed to radiative heat transfer in the oxy-coal flames (a) with gas radiation and (b) without gas radiation for the non-swirling study.

Figure 4.14 shows contours of gas temperature (in K) in the oxy-coal flames using the DPM and TFM frameworks. Despite flame stand-off prediction differences between the two frameworks, the volume averaged flame temperatures were between 1300 – 1350 K for all the simulations. Since the gas temperatures play a big role in determining the wall radiative fluxes, the radiative flux contributions are seen to be identical in Figure 14.4.

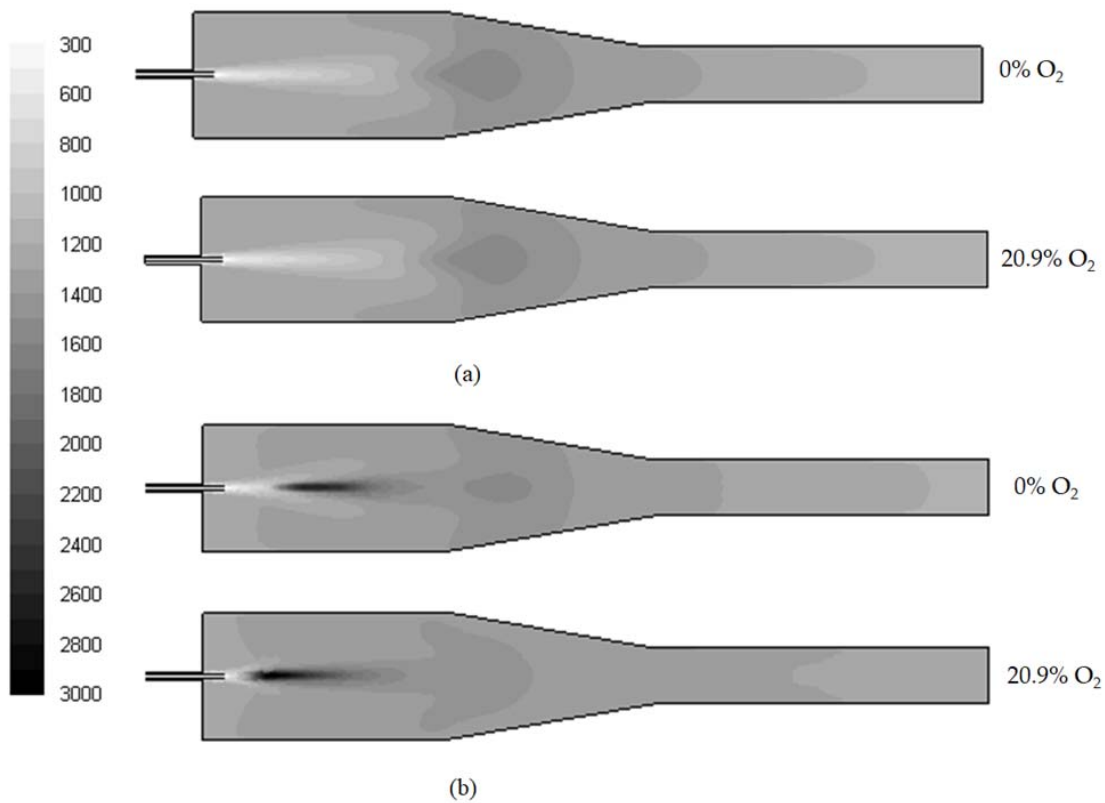


Figure 4.14: Contours of gas temperature (in K) in the non-swirling oxy-coal flames: (a) DPM framework; (b) TFM framework.

Figure 4.15 shows contours of particle volume fractions using the DPM and TFM frameworks. Due to the inherent Stokes number limitation (*see section 2.1.2 for Stokes number explanation*) associated with the TFM framework where the velocities of all particles associated with the dispersed phase (irrespective of their size) are assumed to be equal or follow an equilibrium distribution, the particle dispersion is not as prevalent as seen in the DPM simulations.

While this can have potentially negative implications in highly turbulent systems where eddies over a range of length and time-scales are present, the implications of this equilibrium velocity distribution in these non-swirling flames are likely minimal.

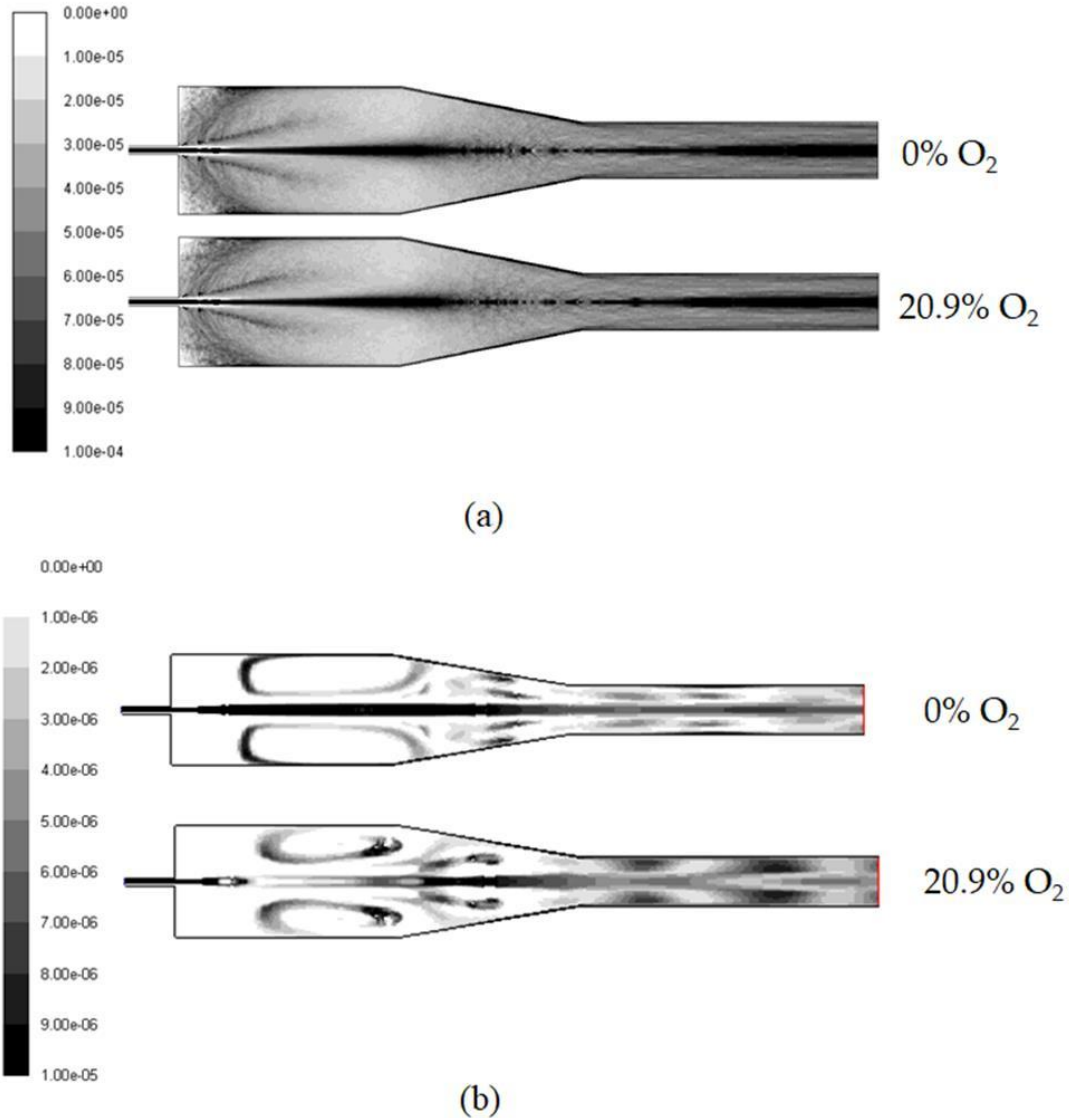


Figure 4.15: Contours of particle volume fractions in the non-swirling oxy-coal flames: (a) DPM framework; (b) TFM framework.

This can be ascertained by looking at the contours of turbulent kinetic energy and turbulent dissipation rates shown in Figure 4.16. The predictions of turbulence from the TFM and DPM

frameworks are seen to be both identical (similar magnitudes) and concentrated around the axial centerline.

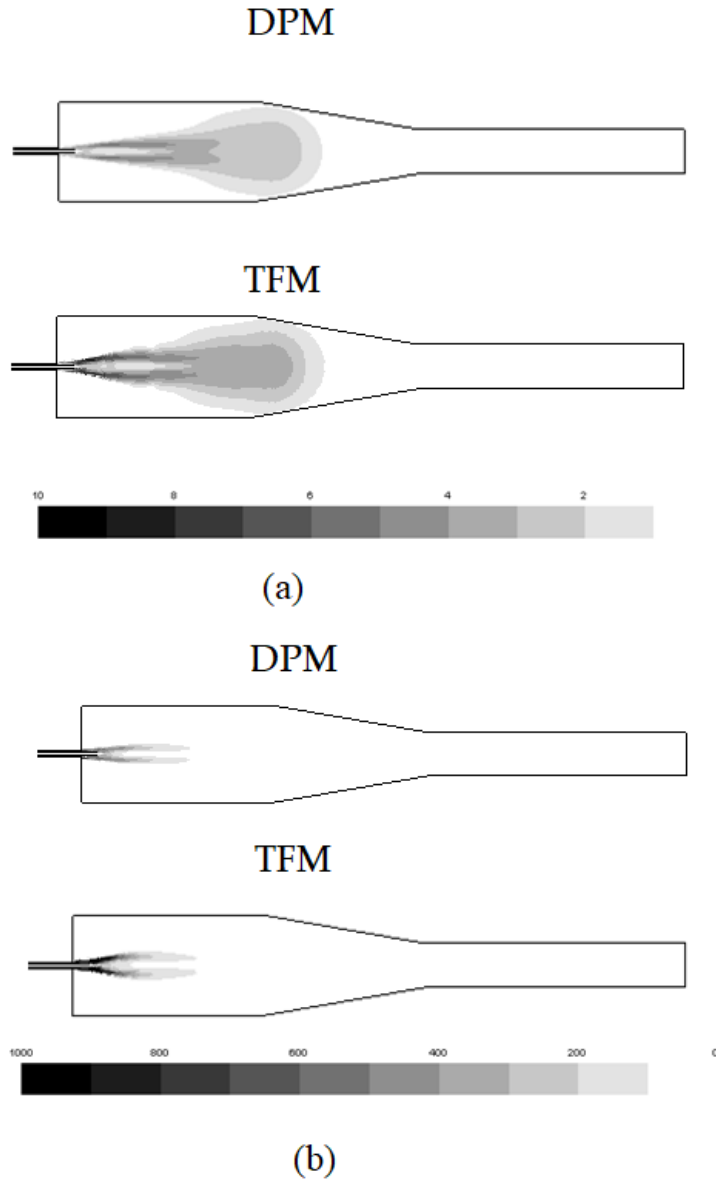


Figure 4.16: Contours of turbulence variables in the 20.9% O₂ non-swirling oxy-coal flames: (a) Turbulent kinetic energy (m²/s²); (b) Turbulent dissipation rate (m²/s³).

The volume averaged particle volume fraction ranged from 2 ppm (for the TFM simulations) to 37 ppm for the DPM simulations in Figure 4.15. The higher particle volume fractions in the DPM simulations is associated with fuel swelling and delayed burnout.

Nevertheless, user-defined functions were employed to modify the fuel emissivities as it transitioned from the parent fuel to ash particles [51]. Since the ash particles have lower emissivities than that of a black body (like soot), the fractional contribution of these gray particles to the net radiative fluxes that is observed in Figure 4.13 at these volume fractions is along the lines of what we would expect, and have generally observed in different pool fires with varying soot volume fractions [102]. The differences in devolatilization and char burnout predictions between the two frameworks also has a minor impact on the characteristics of the hot gases that are brought back to the near burner region through recirculation. These are depicted in Figure 4.17. The average temperature in the recirculation region is about 100 K hotter in the 20.9 % O₂ TFM simulations compared to the DPM simulation and the 0% O₂ TFM simulations. Further, early devolatilization and burnout associated with the TFM simulation depletes the oxygen in the near burner region resulting in lower O₂ mole fractions in the recirculation region in the TFM simulations.

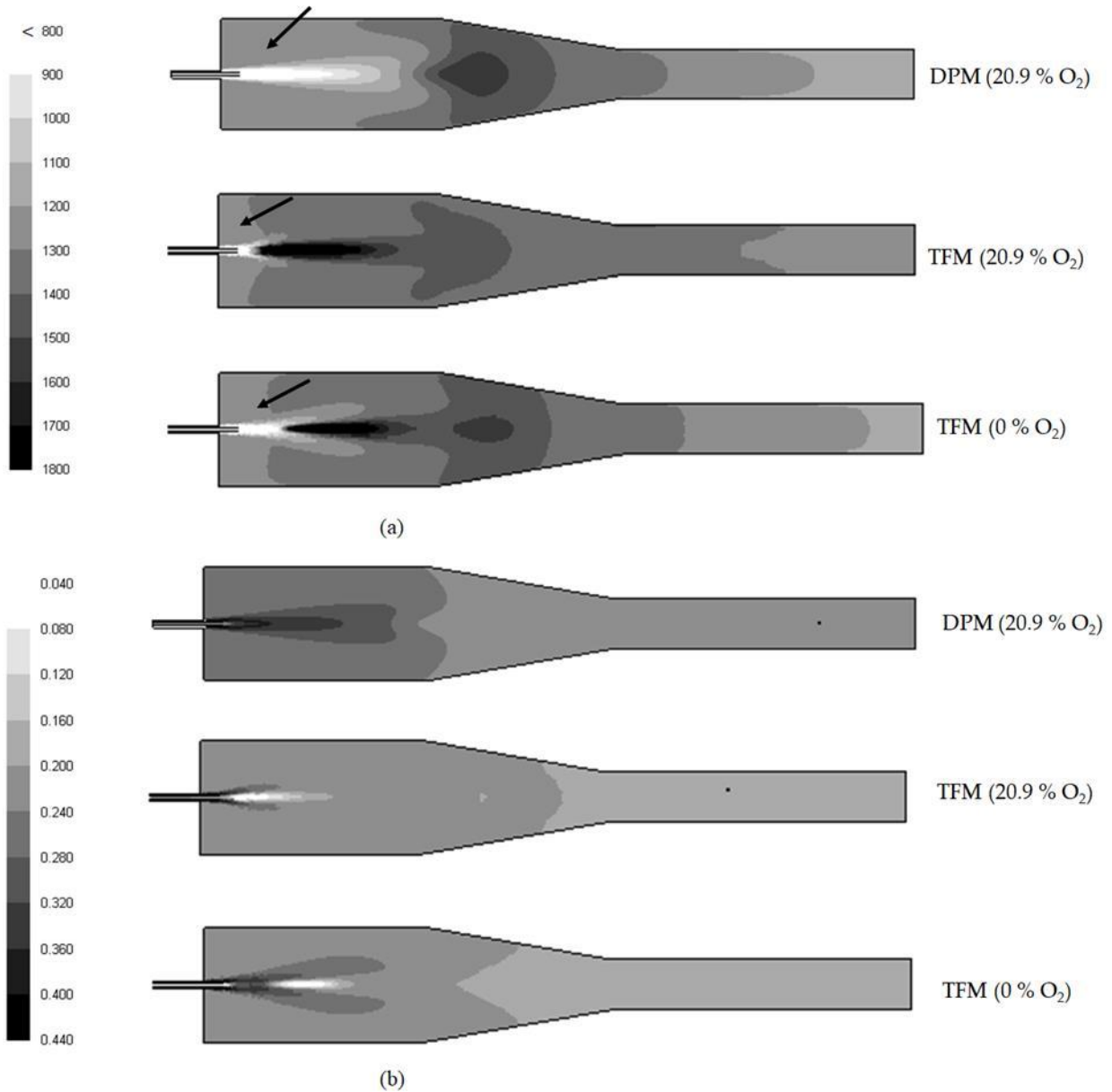


Figure 4.17: Contours near the flame recirculation zone in the non-swirling oxy-coal flames: (a) Gas temperature (The colors/regions corresponding to 1200 K – 1300 K indicated by arrows for brevity); (b) Oxygen mole fractions.

Figures 4.18 and 4.19 show the total heat release, ignition zone flux, and radiation zone flux in the Rosin-Rammler DPM and 2-phase TFM simulations, respectively, for the 0% O_2 scenario. The first bar on the left shows participation of gas, particle, and wall radiation. The middle bar shows just particle and wall radiation participation. The right bar shows just wall

radiation participation. Figures 4.18 and 4.19 indicate that radiation from the participating gases constitute more than 75% of the predicted incident radiative fluxes. Therefore, any changes to the particle/ash PSD during oxy-fuel combustion should not have a significant bearing on the *incident radiative fluxes*. However, differences in ash deposition rates may impact the *net radiative heat fluxes (and heat absorption)* by altering the surface absorptivity and emissivities.

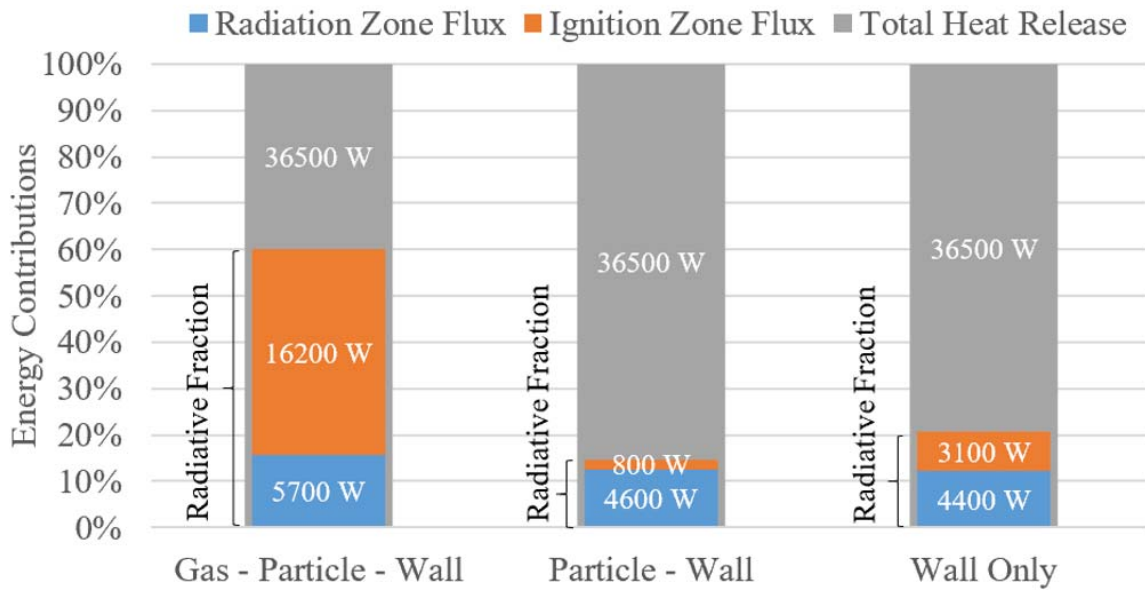


Figure 4.18: The fraction of total flux attributed to radiative heat transfer in the oxy-coal flames in Rosin-Rammler DPM simulations in the 0% O₂ scenario for the non-swirling study.

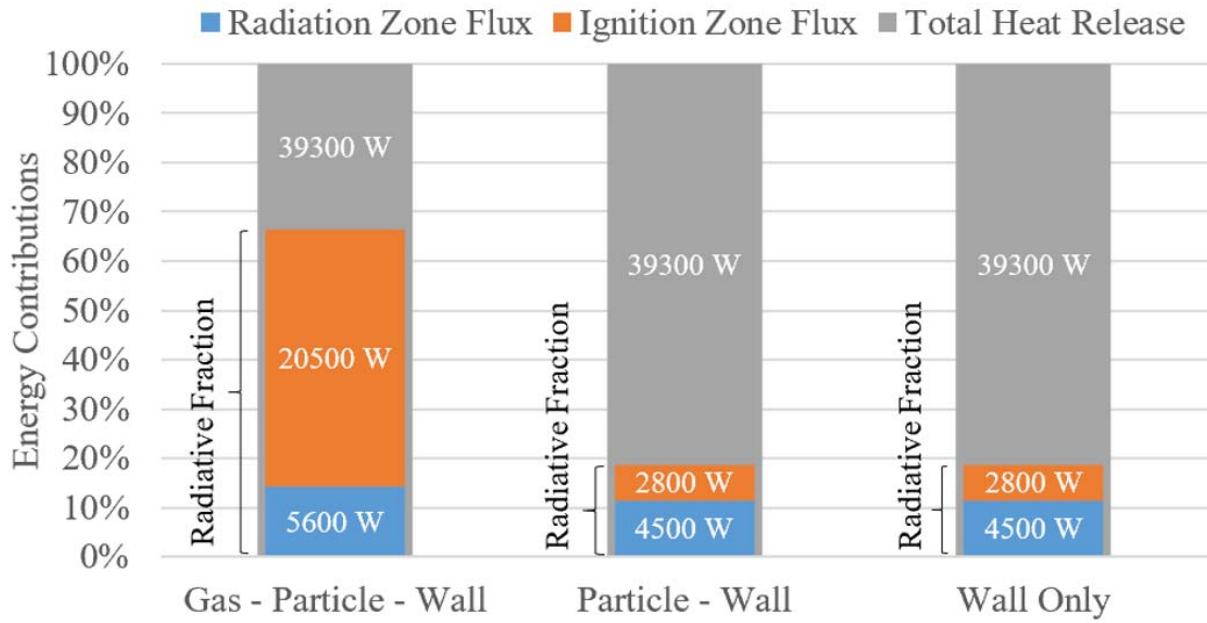


Figure 4.19: The fraction of total flux attributed to radiative heat transfer in the oxy-coal flames in 2-phase TFM simulations in the 0% O₂ scenario for the non-swirling study.

CHAPTER 5

SWIRLING OXY-COAL FLAMES

5.1. Problem Overview and Methods

Ash deposition in coal combustion systems result in several consequences as detailed in previous sections (*see section 2.1*). Ash formation and deposition is a complex physio-chemical process consisting of vaporization, condensation, melting, fragmentation, nucleation and coagulation of the mineral matter and organically bound metals in the parent fuel that results in a distinct tri-modal distribution of the ash particles within the combustor [103]. However, predicting these time-dependent particle size distribution characteristics during combustion as the inlet fuel transitions to ash using the commonly employed DPM based particle simulation methodologies is extremely challenging. Previous work by James et al. employed a Trace Element Partitioning Coal Combustion model to model trace element partitioning from pyritic mineral inclusion; here, the modeling of the coal was undertaken in the DPM framework while the evolution of TEs from the coal particles was calculated outside the CFD idealized environment [12]. Eulerian particle tracking methods (TFM) on the other hand are more amenable to capturing the nucleation, fragmentation and coagulation characteristics of ash. While the ultimate objective of modeling this swirling oxy-coal flame is to compare ash deposition rates against the associated measurements and between modeling frameworks (DPM and TFM), the work done in this thesis was solely to set up a methodology for this comparison to be completed. Hence, no ash deposition rate comparison was carried to completion in this thesis but will be in the future (*see section 6.2*). Creating this modeling methodology consisted of: identifying phenomenological laws and modeling options across the DPM and TFM frameworks, assessing preliminary swirling oxy-coal flame DPM and TFM simulations and an initial radiative flux analysis.

Commercial software ANSYS Fluent 16.2 was used to simulate two oxy-fuel combustion swirling flame scenarios [78]. The two scenarios, entitled Oxy27 and Oxy70, differ only by the overall oxidizer stream composition (27 vol% O₂ and 70 vol% O₂, respectively). Both the Oxy27 and Oxy70 scenario simulations utilized the DPM and TFM frameworks. For each framework, a Rosin-Rammler distribution was utilized for the solid phase.

The experimental oxy-fuel combustion stand-off study was carried out by Zhang et al in the OFC shown in Figure 5.1 (used with permission) [94]. The OFC design is noted for allowing self-sustained combustion with residence time-temperature histories, gas species and particle concentrations all representative of practical units, while still maintaining sufficient control to allow well defined, systematic experimentation in controlled environments [94]. The OFC is rated at 100 kW and measures 3.8 meters in length. There is a primary and secondary oxidizer inlet with a coal feeder on the primary inlet.

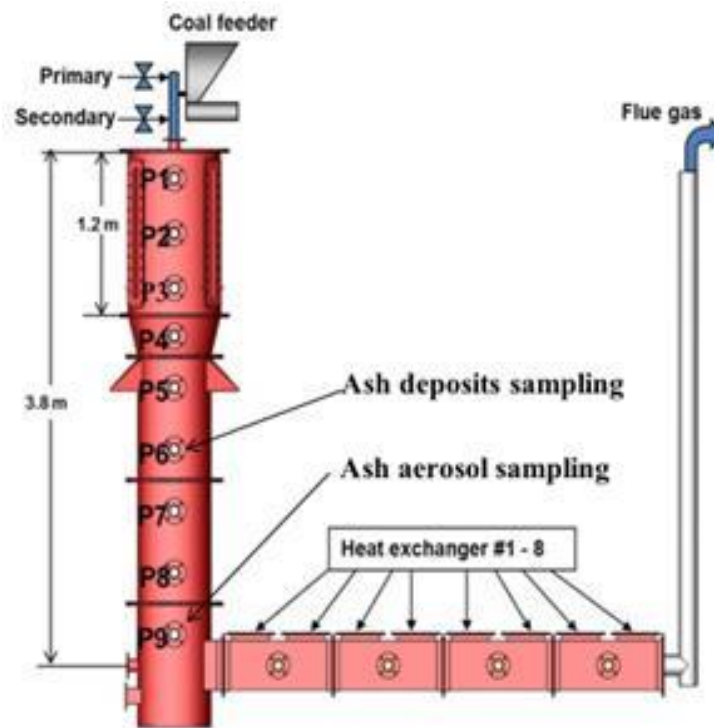


Figure 5.1: Utah's experimental oxy-fuel combustor (OFC).

A 2D, axisymmetric geometry was built in ANSYS Workbench to the specifications of the OFC as shown in Figure 5.2. The length used in this geometry was 4.07 meters. The length and width of the ignition zone was 2.2 meters and 0.61 meters, respectively. The length and width of the radiation zone was 1.6 meters and 0.27 meters, respectively. The geometry was populated with 8,144 cells and had a maximum skewness value of 0.667. The results were found to be invariant with any further refinement to the grid.

Thermal boundary conditions were set for the walls in the ignition and radiation zone. The ignition zone walls were set to a temperature of 1283 K. The radiation zone walls were set to a heat transfer coefficient of $5 \text{ W/m}^2\text{-K}$ and a surrounding fluid temperature of 300 K. Figure 5.3 shows the wall temperature profile along the ignition and radiation zone walls.

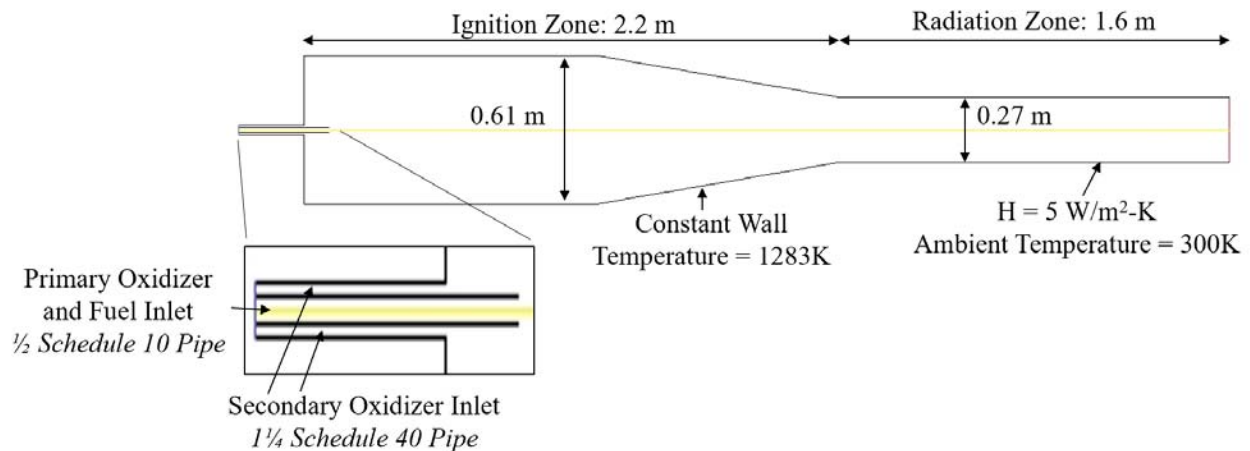


Figure 5.2: 2D, axisymmetric geometry designed to replicate Utah's experimental OFC.

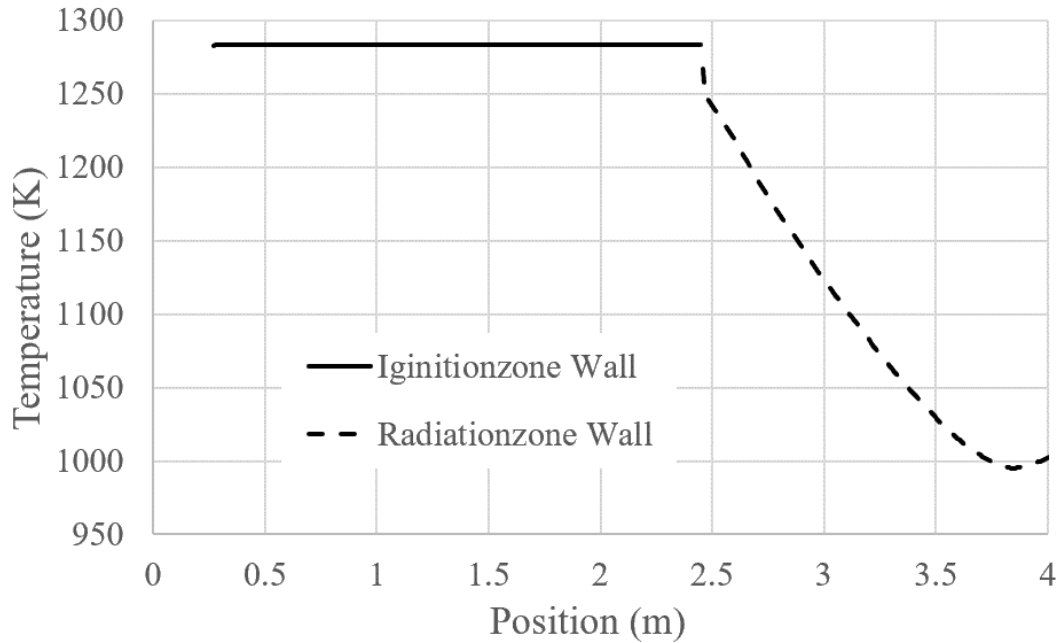


Figure 5.3: Simulated wall temperature profile in the furnace in the swirling study.

Sufco coal, a Utah sub-bituminous coal, was used as the fuel for oxy-fuel combustion.

Table 5.1 contains the proximate and ultimate analysis for this coal.

Table 5.1: Proximate and ultimate analysis of SUFCO coal.

Proximate Analysis (wt.%)		Element Analysis (wt.%)	
Fixed Carbon	47.04	C	67.87
Volatiles	38.49	H	5.45
Ash	8.36	N	1.09
Moisture	6.11	S	0.36
HHV (BTU/lb)	11,899	O (by difference)	16.87

CSSEM data was obtained for this coal and is present in Table 5.2.

Table 5.2: CCSEM and ash chemistry analysis of SUFCO coal.

Al ₂ O ₃	CaO	Fe ₂ O ₃	MgO	MnO	P ₂ O ₅	K ₂ O	SiO ₂	Na ₂ O	SO ₃	TiO ₂
8.34%	18.21%	5.25%	2.84%	0.05%	0.01%	0.33%	48.85%	3.09%	5.96%	0.64%

Table 5.3 shows primary and secondary oxidizer stream specifications obtained from the University of Utah that were employed in the simulations to recreate experimental trials. To

recreate the swirling flame, the primary inlet flow direction was set to have a tangential component of 0.6.

Table 5.3: Primary and secondary oxidizer stream specifications for both swirling combustion scenarios.

	Oxy27	Oxy70
<i>Mass flow rate (kg/h)</i>		
Fuel	3.46	3.46
Primary	6.22	5.26
Secondary	31.8	6.63
<i>Inlet gas temperature (K)</i>		
Primary	480	480
Secondary	480	480
<i>Species concentration of primary inlet (mol%)</i>		
O ₂	21	21
H ₂ O	0	0
CO ₂	79	79
N ₂	0	0
<i>Species concentration of secondary inlet (mol%)</i>		
O ₂	28.2	100
H ₂ O	0	0
CO ₂	71.8	0
N ₂	0	0

The single-rate model was chosen to model devolatilization. This model assumes that the rate of devolatilization is first-order with respect to the volatiles [96]. The devolatilization kinetic rate, k , is defined by input of an Arrhenius type pre-exponential factor, A_1 , and an activation energy, E , as shown below [78]:

$$k = A_1 e^{-(E/R_g T)} \quad (4.1)$$

where R_g is the universal gas constant and T is temperature.

After release of the volatiles during the volatile pyrolysis process, the remaining char reacts with the surrounding gas phase. User-defined functions were implemented to model the diffusional and kinetic resistances associated with the heterogeneous char oxidation. Gaseous combustion

between the fuel volatiles and oxidant was simulated using a two-step mechanism. Initially, volatiles were oxidized and release CO. Then, CO was oxidized to CO₂. The heterogenous and homogenous reactions modeled in these studies are contained in Table 5.4.

Table 5.4: A summary of reactions and kinetic parameters modeled in the swirling study.

	A	Ea, J/kmol	Reference
Heterogeneous reactions			
Devolatilization	382000*	7.4e+07	[97]
Char combustion: $2C_s + O_2 \rightarrow 2CO$	0.86**	1.13e+08	[98]
Homogeneous reactions			
Volatile combustion: $vol \rightarrow 1.05CO + 1.96H_2O + 0.0283N_2 + 0.0082SO_2$	2.119e+11*	2.027e+08	[99]
CO oxidation: $2CO + O_2 \rightarrow 2CO_2$	2.239e+12*	1.7e+08	[100]
<i>Pre-exponential factor, A, units: *(1/s) / **($kg/m^2 s Pa$)</i>			

Table 5.5 provides a complete summary of the different modeling options invoked in this study. Interphase interaction terms were modeled employing identical phenomenological laws in both frameworks. Additionally, non-gray effects of gas radiation and the variations in the radiative properties of the solid phase during combustion were implemented as user-defined functions.

Due to convergence problems in these swirling flames, simulations involving the TFM framework were first run in a steady state fashion to get an estimated solution. After finding a reasonable estimation, the simulations were then carried out in an unsteady state fashion (transient) to find a more accurate prediction.

Table 5.5: A summary of modeling options invoked in the swirling study.

Physics being modeled	CFD Framework (ANSYS Fluent)
Multiphase hydrodynamics	DPM / TFM
Turbulence	SST k-omega
Coal devolatilization	Single-rate
Gas-phase chemistry	Finite rate/Eddy dissipation
Heterogenous chemistry	Surface Reactions
Drag law	Morsi-alexander
Radiation transport equation solver	Discrete ordinates method
Particle radiative property	Variable K_{abs} and K_{scat}
Particle scattering phase function	Anisotropic (forward scattering)
Gas-phase radiative property	Perry (5gg) [77]
Solver	Pressure-based
Discretization Schemes	Quick for Spatial Discretization

5.2. Results

5.2.1. Particle Dispersion Differences

The particle size distribution model at the injection point was based on the Rosin-Rammler distribution shown in Figure 5.4 [91]. For the DPM and TFM simulations, 40 diameter and 1 diameter intervals were used, respectively. The mean Rosin-Rammler distribution particle diameter of 85-microns was chosen as the TFM's 1 diameter size.

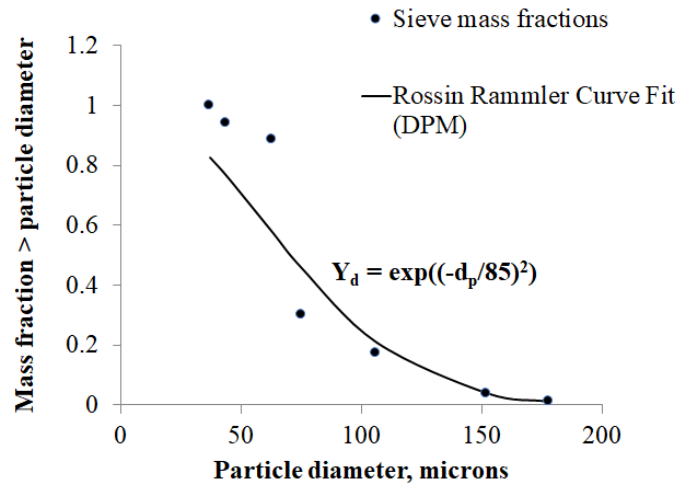


Figure 5.4: Particle size distributions and Rosin-Rammler curve fit for the SUFCO sub-bituminous coal used in the swirling study.

To understand the differences in particle distribution in both DPM and TFM simulations, the volume fraction of particles was plotted in both simulation frameworks. Figure 5.5 shows the particle volume fractions in the DPM simulations for the Oxy27 and Oxy70 scenarios. Figure 5.6 shows the particle volume fractions in the TFM simulations for the Oxy27 and Oxy70 scenarios. Due to the inherent Stokes number limitation (*see section 2.1.2 for Stokes number explanation*) associated with the TFM framework where the velocities of all particles associated with the dispersed phase (irrespective of their size) are assumed to be equal or follow an equilibrium distribution, the particle dispersion is not as prevalent as seen in the DPM simulations.

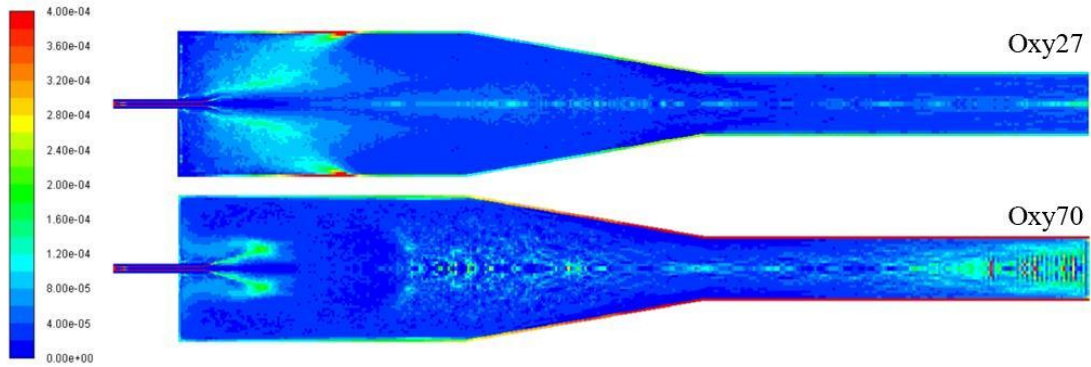


Figure 5.5: Particle volume fractions from the DPM simulations for the swirling study.

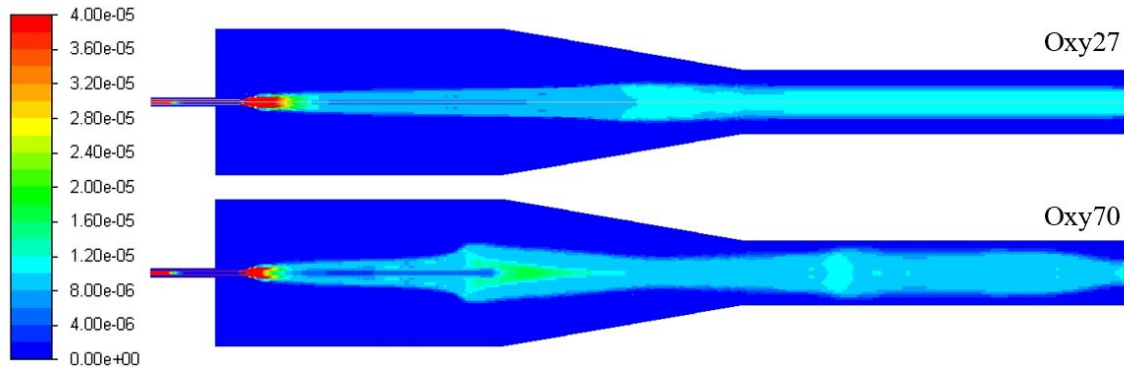


Figure 5.6: Particle volume fractions from the TFM simulations for the swirling study

5.2.2. Temperature and Velocity Profile Comparison

To assess the temperature and velocity characteristics in the swirling oxy-coal combustion environment, contours of gas temperature and velocity were generated. Additionally, axial gas temperature and velocity profiles were plotted against experimental measurements. Figure 5.7 shows the gas temperature contours in the DPM and TFM simulations for the Oxy27 (a) and Oxy70 (b) scenarios, respectively. Arrows indicate peak combustion temperatures (PCT). In the Oxy27 case, the PCT predicted by the TFM framework is about 100 K higher than the DPM framework. PCT predicted in the Oxy70 scenario is much higher than the Oxy27 scenario which is likely due to the availability of the combustion diluent: CO_2 (which acts as a heat sink). In the Oxy70

scenario, the PCT predicted by the TFM framework is about 700 K higher than the DPM framework.

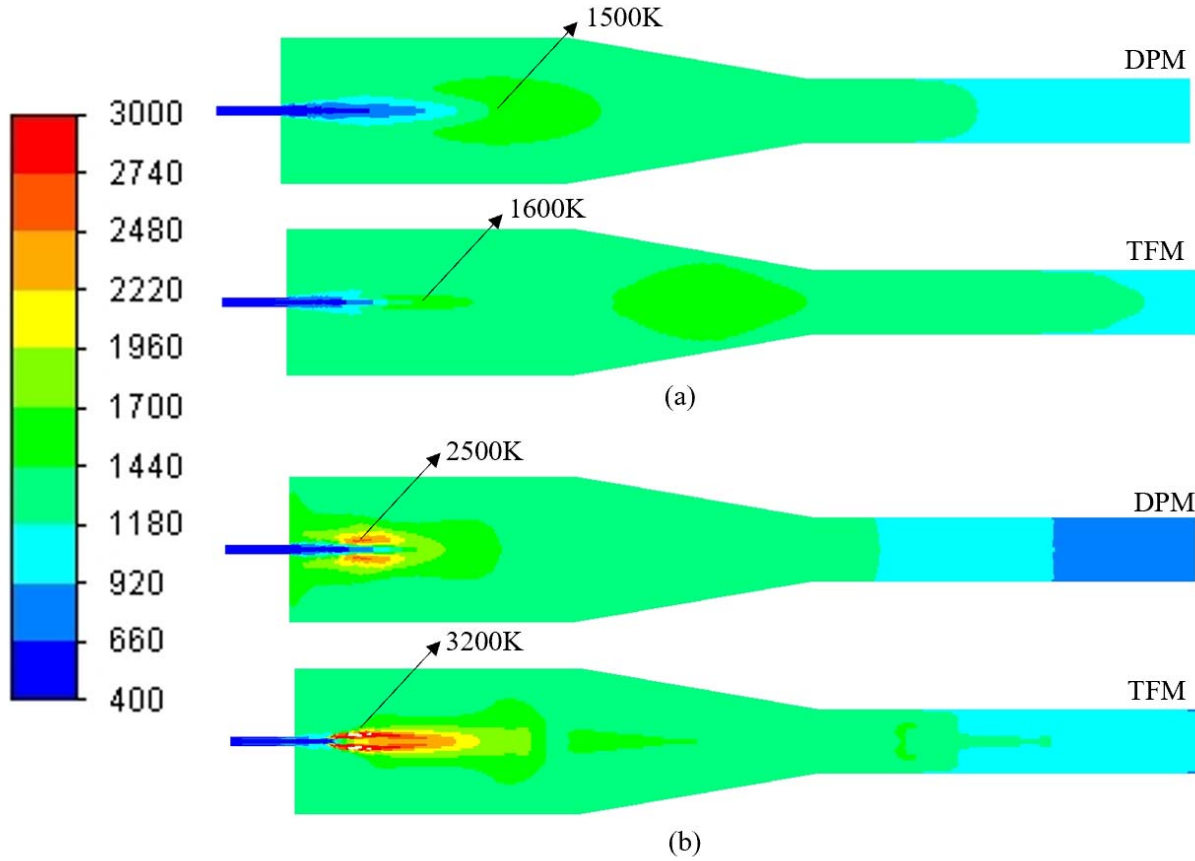
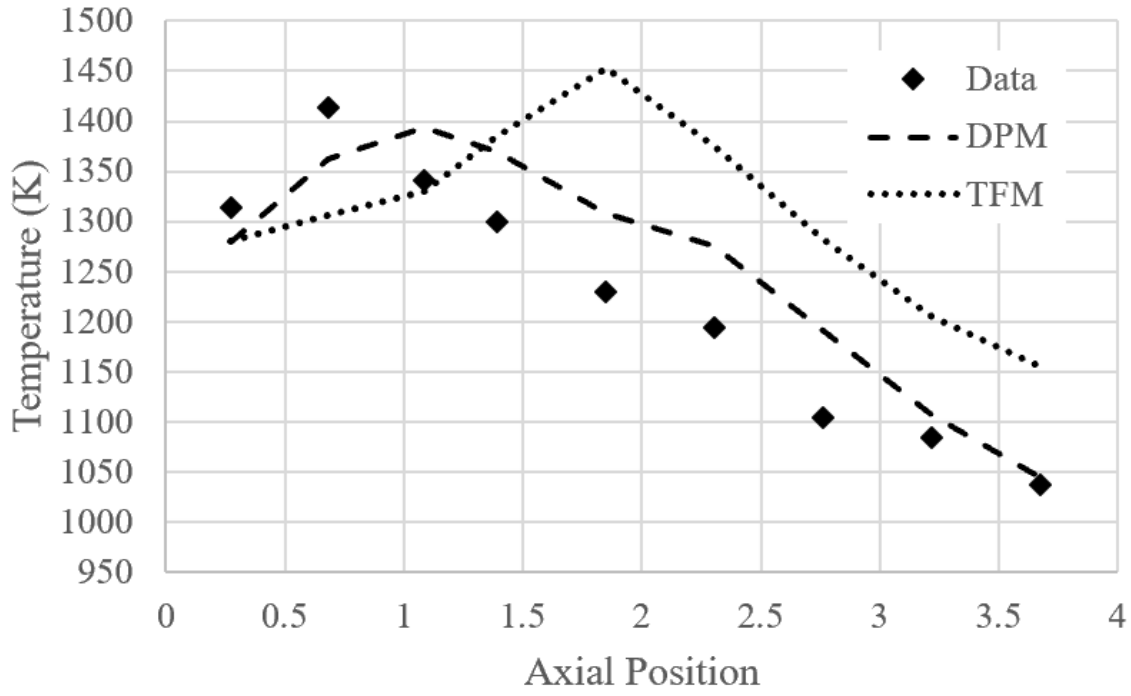
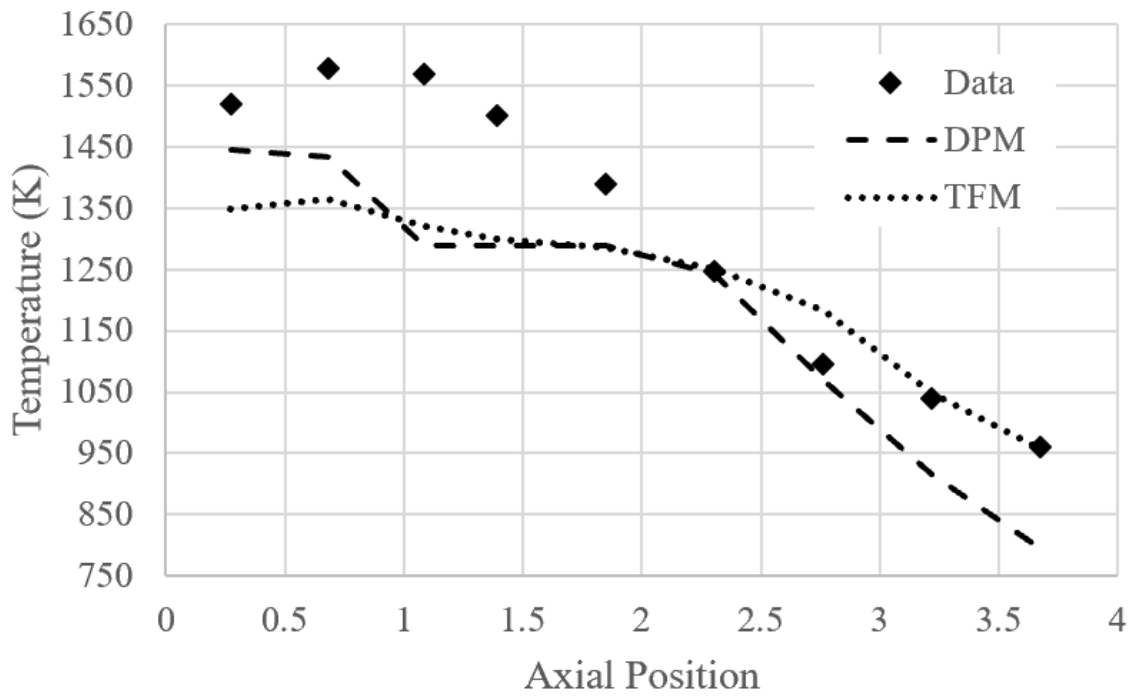


Figure 5.7: Contours of gas temperature in the DPM and TFM frameworks in the (a) Oxy27 and (b) Oxy70 scenarios for the swirling study. Arrows indicate peak combustion temperatures.

Figure 5.8 shows average-weighted temperature profiles from the University of Utah’s experimental work, the DPM simulations, and the TFM simulations. In Figure 5.8a, both the DPM and TFM frameworks show later peak temperatures than the data does. In Figure 5.8b, both the DPM and TFM frameworks predict lower peak temperatures than the data does.



(a)



(b)

Figure 5.8: Experimental Data, DPM, and TFM axial temperature profiles in the (a) Oxy27 and (b) Oxy70 scenarios for the swirling study.

Figure 5.9 shows the gas velocity contours from the DPM and TFM simulations for the Oxy27 (a) and Oxy70 (b) scenarios. Profiles look similar between the frameworks; however, TFM simulations had a higher velocity magnitude prediction near the exit of the burner.

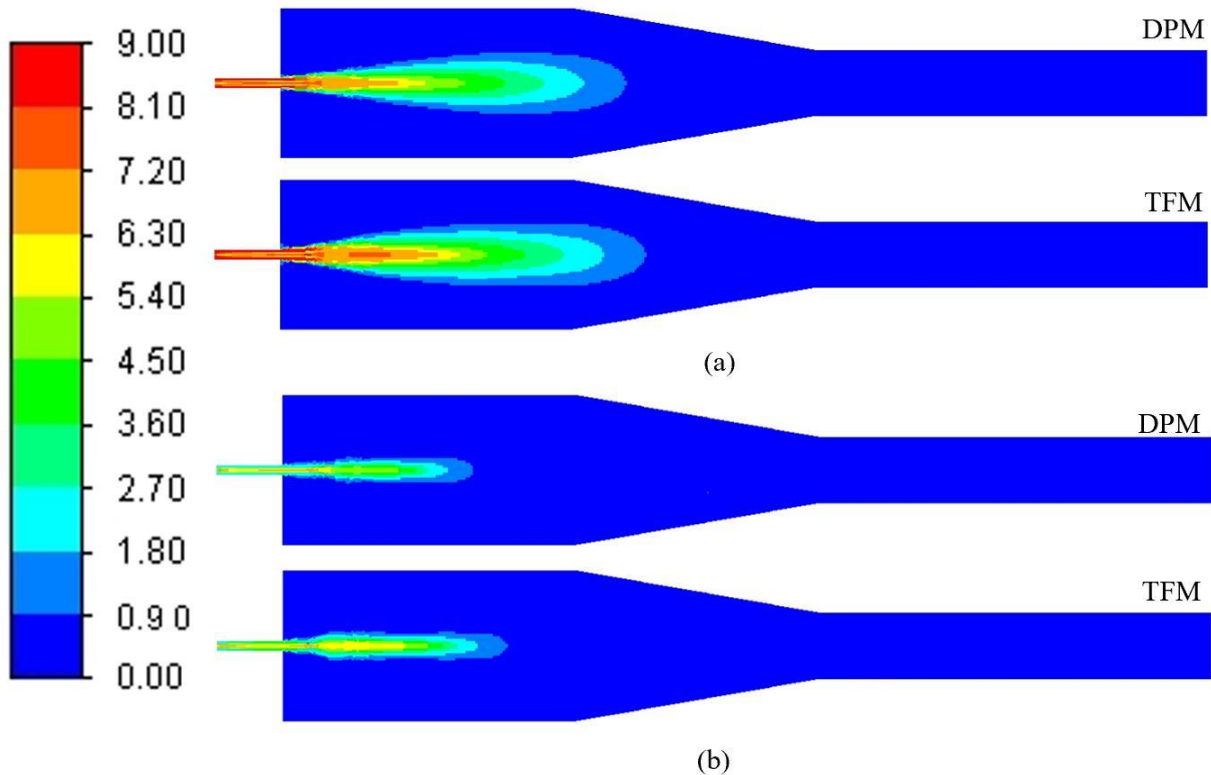
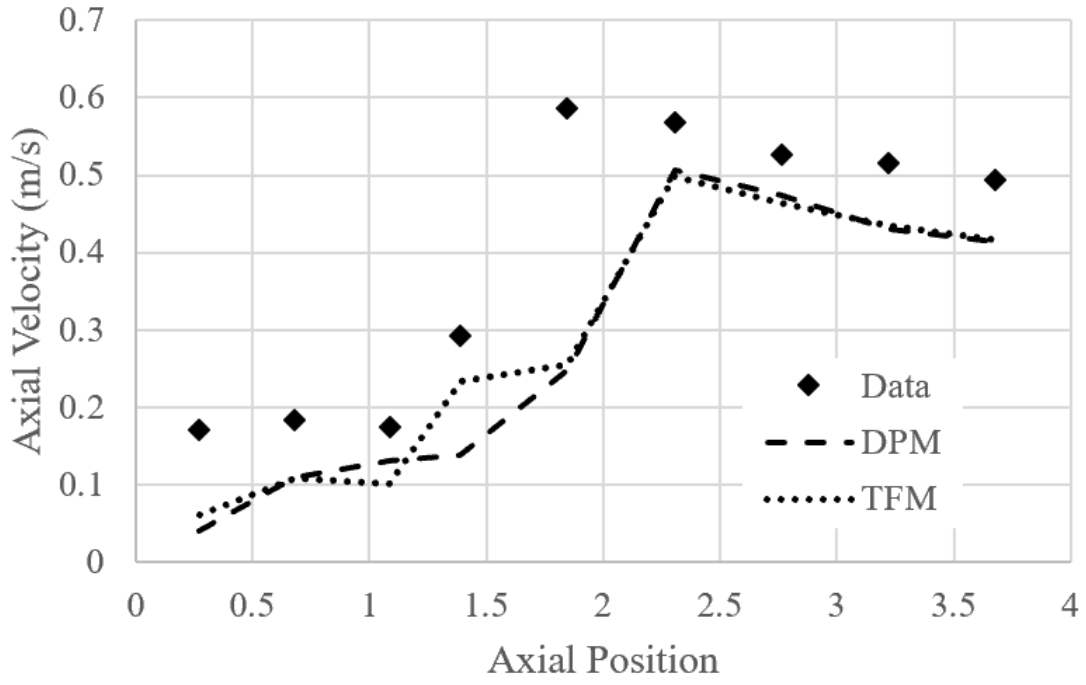
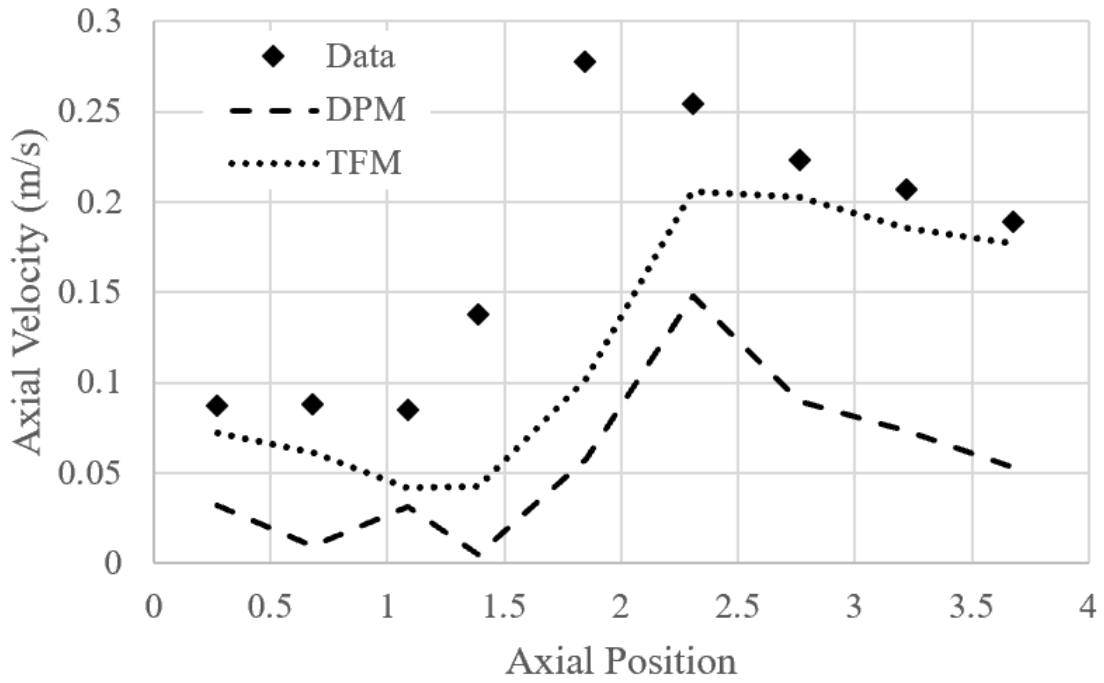


Figure 5.9: Contours of gas velocity in the DPM and TFM frameworks in the (a) Oxy27 and (b) Oxy70 scenarios for the swirling study.

Figure 5.10 show average-weighted velocity profiles from the University of Utah’s experimental work, the DPM simulations, and the TFM simulations. In Figure 5.10a, both the DPM and TFM frameworks show similar data trends; however, both frameworks predicted lower velocities than the data. In Figure 5.10b, frameworks were less capable in capturing data trends. Further refinement to both DPM and TFM models may be needed to accurately represent experimental temperature and velocity trends.



(a)



(b)

Figure 5.10: Experimental Data, DPM, and TFM axial velocity profiles in the (a) Oxy27 and (b) Oxy70 scenarios for the swirling study.

5.2.3. Summary of Measured and Predicated Boiler Variables

Tables 5.6 and 5.7 show a summary of measured and predicted environmental and ash variables in the oxy-fuel combustor (OFC) for the Oxy27 and Oxy70 scenarios, respectively. Predicted variables fell within an accepted range of accuracy for the Oxy27 scenario. However, in the Oxy70 scenario, the predicted and measured values did not compare well; specifically, the TFM framework's oxygen flue gas concentration prediction and the DPM framework's ash concentration predicitions did not compare well with measured values. Further refinement for both frameworks is needed to accurately capture experimental measurements.

Table 5.6: A summary of measured and predicted environmental and ash variables in the Oxy27 scenario for the swirling study.

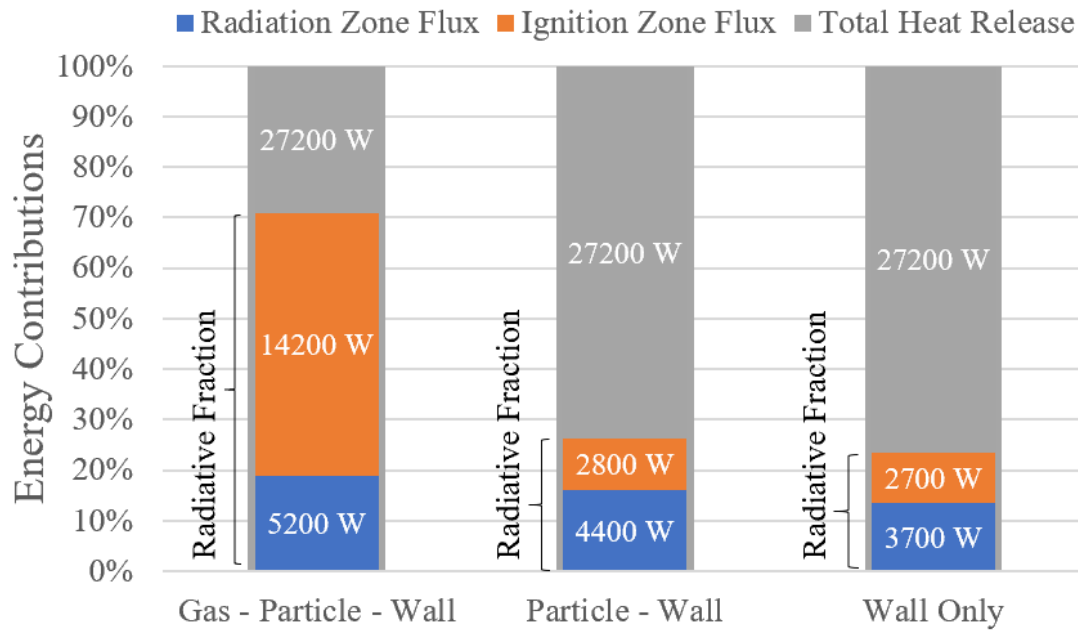
Characteristics	Oxy27 Scenario		
	Measured	DPM Predicted	TFM Predicted
Coal input rate (kg/hour)	3.46	3.46	3.46
Energy input (kW)	26	27	27
O ₂ fraction in dry flue gas (vol.%)	3	2.5	1
Flue gas flow rate (m ³ /hour @ STP)	22.4	24.3	24.1
Ash concentration at outlet (g/m ³ @ STP)	12.9	10.7	13.3
Ash concentration at port 6 (g/m ³)	2.4	2.7	3.5

Table 5.7: A summary of measured and predicted environmental and ash variables in the Oxy70 scenario for the swirling study.

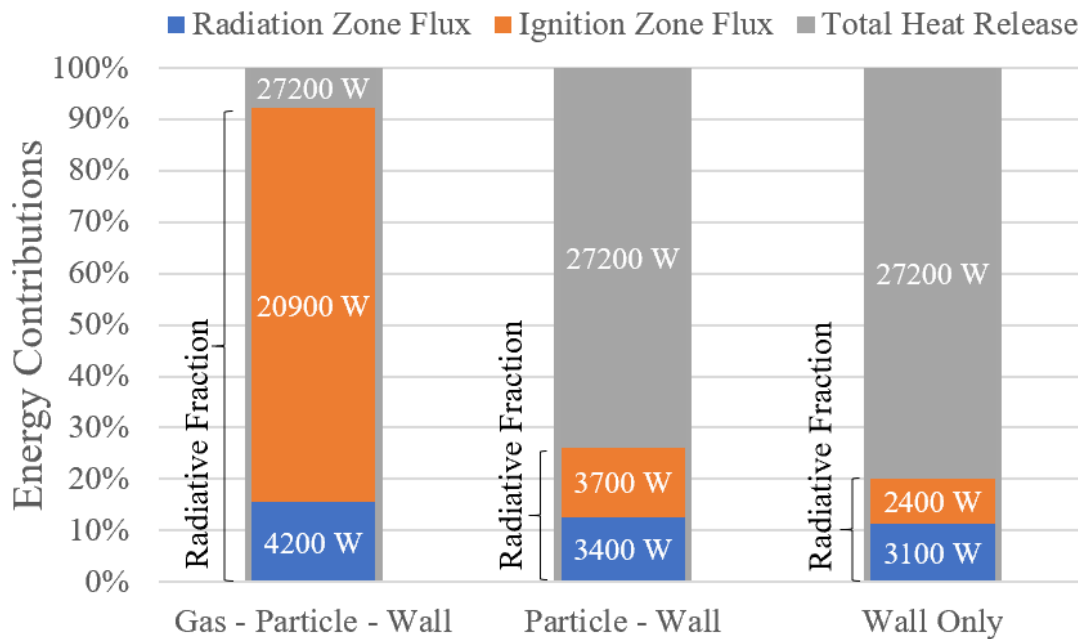
Characteristics	Oxy70 Scenario		
	Measured	DPM Predicted	TFM Predicted
Coal input rate (kg/hour)	3.46	3.46	3.46
Energy input (kW)	26	27	27
O ₂ fraction in dry flue gas (vol.%)	3	3.5	13.3
Flue gas flow rate (m ³ /hour @ STP)	9	9.8	11.6
Ash concentration at outlet (g/m ³ @ STP)	32.3	24.2	37.4
Ash concentration at port 6 (g/m ³)	5.8	1.7	4.4

5.2.4. Radiative Characteristics

Figures 5.11 and 5.12 show the total heat release, ignition zone flux, and radiation zone flux in the DPM and TFM simulations, respectively. In both figures, the first bar on the left shows participation of gas, particle, and wall radiation. The middle bar shows just particle and wall radiation participation. The right bar shows just wall radiation participation. Radiation was the dominant mode of heat transfer with 70% to 90% of the total wall heat transfer due to radiation. Radiation from the participating gases accounted for 75% of the radiative heat transfer. Both modeling frameworks showed similar results.



(a)



(b)

Figure 5.11: The fraction of total flux attributed to radiative heat transfer in the oxy-coal flames for the Oxy27 (a) and the Oxy70 (b) DPM simulations for the swirling study.

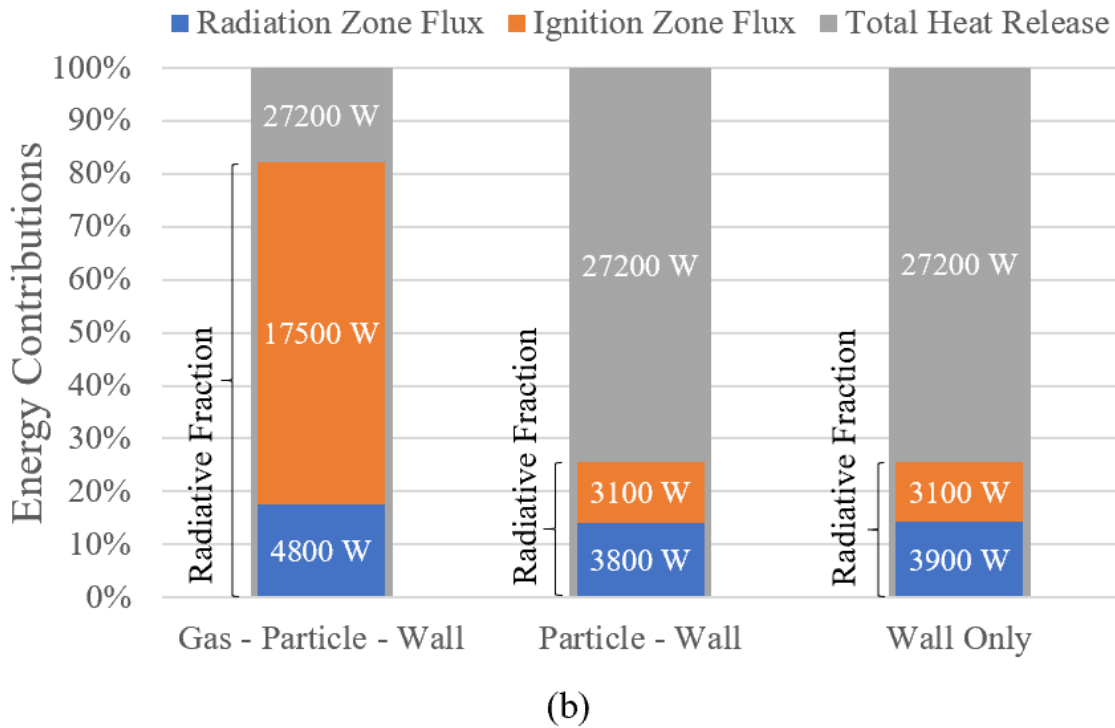
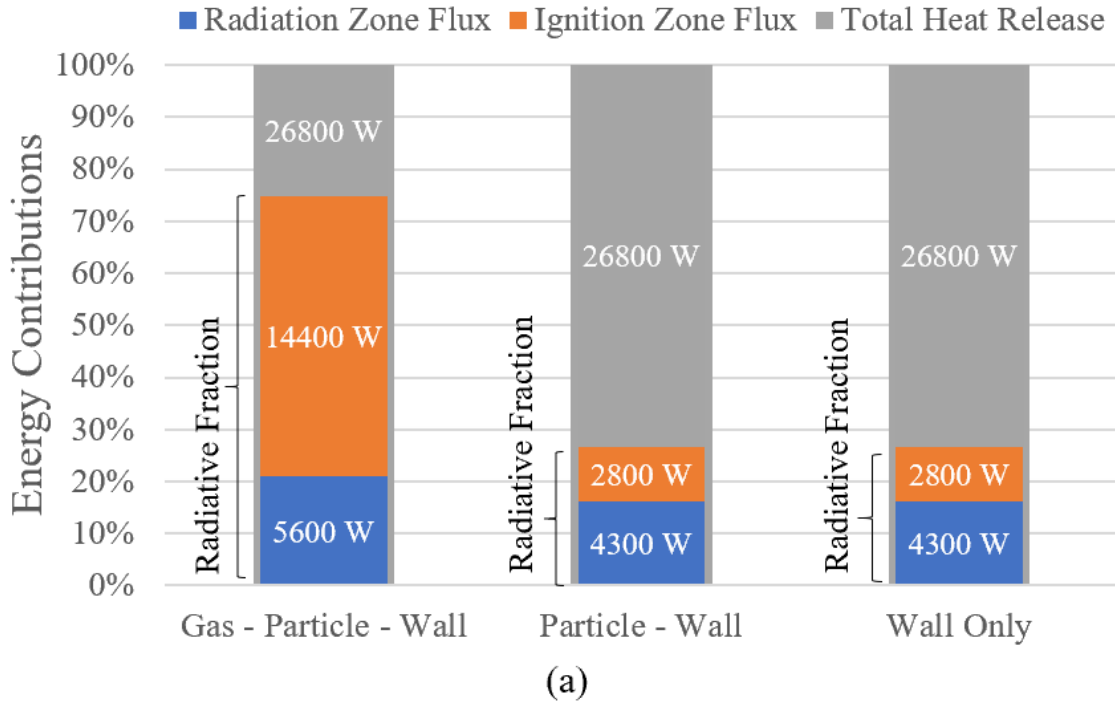


Figure 5.12: The fraction of total flux attributed to radiative heat transfer in the oxy-coal flames for the Oxy27 (a) and the Oxy70 (b) TFM simulations for the swirling study.

CHAPTER 6

SUMMARY

6.1. Conclusions

In conclusion, these studies highlight the importance of model choice when utilizing computational fluid dynamics for characterizing multiphase flows in oxy-fuel combustion environments.

6.1.1 2D, Non-Swirling Oxy-Coal Flame Stand-off Study

The ability of multiphase modeling frameworks (DPM and TFM) to capture the experimentally observed flame ignition/stand-off characteristics in non-swirling oxy-coal flames (measured at the University of Utah) were investigated in this study. The interphase interaction terms were modeled employing identical phenomenological laws across both frameworks. First, simulations of inert particles were carried out and were found to yield identical predictions of particle velocities and heat-up across both frameworks. Next, user-defined functions (UDFs) were utilized in the TFM framework to model the diffusional and kinetic resistances associated with the heterogeneous char oxidation. In the DPM framework, non-gray effects of gas radiation and the variations in the radiative properties of the solid phase during combustion were also implemented as UDFs. Based on the results of this study, the following conclusions can be drawn:

1. The particle, gas temperatures and their velocities reached identical values (equilibrated) at the end of the radiant zone.
2. The DPM approach was unable to capture the experimentally observed trends for flame stand-off as a function of oxygen concentration in the primary burner.
3. The TFM approach was able to capture the experimentally observed trends for flame stand-off as a function of oxygen concentration in the primary burner.

4. Experimentally observed effects of primary air composition, secondary air temperature and wall temperature on flame stand-off were also captured reasonably well by TFM simulations.
5. Radiation was the dominant mode of heat transfer with the radiant heat loss fraction (Radiative heat loss/Total chemical heat release) determined to be 0.6 for both flames.
6. Radiation from the participating gases accounted for 75% of the radiative heat transfer.
7. The incident radiative flux predictions were in good agreement with measured values from similar flames in this furnace.

6.1.2 2D, Swirling Oxy-Coal Flame Study

The ability of multiphase modeling frameworks (DPM, TFM) to capture the experimentally observed temperature, velocities, ash concentrations, and radiative heat transfer characteristics in swirling oxy-coal flames (measured at the University of Utah) were investigated in this study to enable their extension to study ash deposition processes. The interphase interaction terms were modeled employing identical phenomenological laws across both frameworks. User-defined functions (UDFs) were utilized in the TFM framework to model the diffusional and kinetic resistances associated with the heterogeneous char oxidation. In the DPM framework, non-gray effects of gas radiation and the variations in the radiative properties of the solid phase during combustion were also implemented as UDFs. Based on the results of this study, the following conclusions can be drawn:

1. Particle dispersion is not as prevalent in the TFM simulations as seen in the DPM simulations.
2. A preliminary analysis of temperature/velocity profiles and ash concentrations suggests that further refinement may be needed for the TFM and DPM frameworks in these swirling flows.

3. Radiation was the dominant mode of heat transfer with the radiant heat loss fraction (Radiative heat loss/Total chemical heat release) determined to be in the range of 0.7-0.9 for both flames.
4. Radiation from the participating gases accounted for 75% of the radiative heat transfer.

6.2. Future Work

The modeling methodologies and frameworks developed in this thesis can be used to enable investigation into other areas of interest; specifically, an investigation of experimental biomass studies, ash deposition processes in both the DPM and TFM frameworks, and further refinement to the TFM framework.

Coal-biomass oxy-combustion experiments at higher pressures were carried out by partner Chinese Universities. Based on the data collected, a similar analysis to understand deposition and radiative transfer can be carried out.

CCSEM data of the parent fuels in conjunction with Rossin-Rammler curve fits to the size distributions were originally going to be employed to simulate coal combustion using a particle tracking methodology. The CCSEM data is unfortunately not available. However, to provide a rough estimation of this ash deposition process, particle tracks can be post-processed via:

1. An in-house slag model that will employ a particle capture criterion (that is based on the ash particle composition, density, viscosity and surface tension) to capture the ash at the walls. This model will help predict the slag composition and thickness.

2. An ash vaporization model developed at UND that will be employed to predict the PM_{10} compositions and amounts at the outlet.

Additionally, in the TFM framework, coagulation and nucleation models can be implemented to model the ash deposition process.

Finally, further refinement of the TFM model is needed; specifically, particle dispersion models need to be analyzed and improved.

REFERENCES

1. Buhre, B. J. P., L. K. Elliott, C. D. Sheng, R. P. Gupta, and T. F. Wall. Oxy-fuel combustion technology for coal-fired power generation.” *Progress in Energy and Combustion* 2005; 31(4): 283–307.
2. Chen, L., Sze Yong, and Ahmed F. Ghoniem. Oxy-fuel combustion of pulverized coal: characterization, fundamentals, stabilization and CFD modeling. *Progress in Energy and Combustion Science* 2012; 38(2): 156–214.
3. Fan, J. R., X. D. Zha, P. Sun, and K. F. Cen. Simulation of ash deposit in a pulverized coal-fired boiler. *Fuel* 2001; 80(5): 645-654.
4. Kleinhans, Ulrich, Christoph Wieland, Flemming J. Frandsen, and Hartmut Spliethoff. Ash formation and deposition in coal and biomass fired combustion systems: Progress and challenges in the field of ash particle sticking and rebound behavior. *Progress in Energy and Combustion Science* 2018; 68: 65-168.
5. Lee, F. C. C., and F. C. Lockwood. Modelling ash deposition in pulverized coal-fired applications. *Progress in Energy and Combustion Science* 1999; 25(2): 117-132.
6. Gupta, R. P., T. F. Wall, I. Kajigaya, S. Miyamae, and Y. Tsumita. Computer-controlled scanning electron microscopy of minerals in coal implications for ash deposition. *Progress in Energy and Combustion Science* 1998; 24(6): 523-543.
7. Raeva, Anna A., David T. Pierce, Wayne S. Seames, Evguenii I. Kozliak. A method for measuring the kinetics of organically associated inorganic contaminant vaporization during coal combustion. *Fuel Processing Technology* 2011; 92(7): 1333-1339.
8. Raeva, Anna A., Nagaraju Dongari, Anastasia A. Artemyeva, Evguenii I. Kozliak, David T. Pierce, and Wayne S. Seames. Experimental simulation of trace element evolution from

- the excluded mineral fraction during coal combustion using GFAAS and TGA-DSC. *Fuel* 2014; 124: 28-40.
9. Zhan, Zhonghua. Ash deposition and ash aerosol formation mechanisms during oxy-coal combustion. 2015. University of Utah, PhD Dissertation.
 10. Raask, E. Mineral impurities in coal combustion: behavior, problems, and remedial measures. New York: Hemisphere Publishing Corporation; 1985. Print.
 11. Artemyeva, Anastasia A., Wayne Seames, David Pierce, and Evguenii Kozliak. Molecular scale studies of trace element sulfide evaporation and atomization during coal combustion using GFAAS and TGA-DSC. *Fuel* 2017; 188: 544-552.
 12. James, David W., Gautham Krishnamoorthy, Steven A. Benson, and Wayne S. Seames. Modeling trace element partitioning from pyritic mineral inclusions. *Fuel Processing Technology* 2014; 126C: 284-297.
 13. Nowok, J. W., and S. A. Benson. Inorganic transformations and ash deposition during combustion. Engineering Foundation: New York 1991; 10-15: 405-424.
 14. Benson, S. A., T. A. Erickson, R. R. Jensen, and J. D. Laumb. Transformations model for predicting size and composition of ash during coal combustion. *Fuel Chemistry Division Preprint* 2002; 47(2): 796.
 15. Jassim, E., S. A. Benson, F. M. Bowman, and W. S. Seames. Influence of fragmentation on the behavior of pyrite particles during combustion. *Fuel Processing Technology* 2011; 92: 970–976.
 16. Fix, Gregory, W. S. Seames, M. D. Mann, and S. A. Benson. The effect of oxygen-to-fuel stoichiometry on coal ash fine-fragmentation mode formation mechanisms. *Fuel Processing Technology* 2011; 92: 793–800.

17. Fix, Gregory, W. S. Seames, M. D. Mann, S. A. Benson, and D. Miller. The effect of combustion temperature on coal ash fine-fragmentation mode formation mechanisms. *Fuel* 2013; 113: 140-147.
18. Seames, W. S. An initial study of the fine fragmentation fly ash particle mode generated during pulverized coal combustion. *Fuel Processing Technology* 2003; 81: 109-125.
19. Quann, R. J., M. Neville, M. Janghorbani, C. A. Mims, and A. F. Sarofim. Vaporization of minerals during coal combustion. *Environmental Science and Technology* 1982; 16: 776-781.
20. Sheng, C., and Y. Li. Experimental study of ash formation during pulverized coal combustion in O₂/CO₂ mixtures. *Fuel* 2008; 87: 1297–1305.
21. Theis M., B. J. Skrifvars, M. Zevenhoven, M. Hupa, and H. Tran. Fouling tendency of ash resulting from burning mixtures of biofuels; part 2: deposit chemistry. *Fuel* 2006; 85: 1992–2001.
22. Nelson, P. F. Trace metal emissions in fine particles from coal combustion. *Energy Fuels* 2007; 21: 477–84.
23. Frandsen, F. J. Ash formation, deposition and corrosion when utilizing straw for heat and power roduction. 2011. Lyngby, Denmark. Technical University of Denmark, Doctoral Thesis.
24. Wang, Huafeng, and John N. Harb. Modeling of ash deposition in large-scale combustion facilities burning pulverized coal. *Progress in Energy and Combustion Science* 1997; 23(3): 267-282.
25. Zhan, Zhonghua, S. Tian, A. R. Fry, and Jost O. L. Wendt. Formation of ash aerosols and ash deposits of coal blends. *International Symposium on Coal Combustion*, 2015; 121-131.

26. Baxter, L. L. Ash deposit formation and deposit properties: a comprehensive summary of research conducted at sandia's combustion research facility. No. SAND2000-8253. Albuquerque, NM, US, 2000. Web.
27. Fryda, L., Celia Sobrino, M. Cieplik, and W. L. Van de Kamp. Study on ash deposition under oxyfuel combustion of coal/biomass blends. *Fuel* 2010; 89(8): 1889-1902.
28. Beckmann, A. M., M. Mancini, R. Weber, S. Seebold, and M. Müller. Measurements and CFD modeling of a pulverized coal flame with emphasis on ash deposition. *Fuel* 2016; 167: 168-179.
29. Weber, Roman, M. Mancini, Natalia Schaffel-Mancini, and Tomasz Kupka. On predicting the ash behavior using computational fluid dynamics. *Fuel Processing Technology* 2013; 105: 113-128.
30. Cai, Yongtie, Kunlin Tay, Zhimin Zheng, Wenming Yang, Hui Wang, Guang Zeng, Zhiwang Li, Siah Keng Boon, and Prabakaran Subbaiah. Modeling of ash formation and deposition processes in coal and biomass fired boilers: a comprehensive review. *Applied Energy* 2018; 230: 1447-1544.
31. Fang, Qingyan, Huajian Wang, Yan Wei, Lin Lei, Xuelong Duan, and Huaichun Zhou. Numerical simulations of the slagging characteristics in a down-fired, pulverized-coal boiler furnace. *Fuel Processing Technology* 2010; 91(1): 88-96.
32. Ma, Zhanhua, Felicia Iman, Pisi Lu, Rod Sears, Lingbu Kong, A. S. Rokanuzzaman, Donald P. McCollor, and Steven A. Benson. A comprehensive slagging and fouling prediction tool for coal-fired boilers and its validation/application. *Fuel Processing Technology* 2007; 88(11): 1035-1043.

33. Kær, S. K., L. A. Rosendahl, and L. L. Baxter. Towards a CFD-based mechanistic deposit formation model for straw-fired boilers. *Fuel* 2006; 85: 833–848.
34. Forstner, M., G. Hofmeister, M. Jöller, J. Dahl, M. Braun, and S. Kleditzsch. CFD simulation of ash deposit formation in fixed bed biomass furnaces and boilers. *Progress in Computational Fluid Dynamics* 2006; 6(4-5): 248–261.
35. Epple, B., B. Krohmer, A. Hoppe, H. Mueller, and R. Leithner. CRFD studies for boilers fired with high ash containing and slagging lignites. *Clean Air* 2005; 6: 137–155
36. Mueller, C., B.-J. Skrifvars, R. Backman, and M. Hupa. Ash deposition prediction in biomass fired fluidized bed boilers-combination of CFD and advanced fuel analysis. *Progress in Computational Fluid Dynamics* 2003; 3(2-4).
37. Eddings, E.G., K.A. Davis, M.P. Heap, J.R. Valentine, and A.F. Sarofim. Mineral matter transformation during pulverized coal combustion. *Developments in Chemical Engineering and Mineral Processing* 2001; 9(3-4): 313–327.
38. Schell, U., S. Richter, and K. R. Hein. Numerical simulation of slagging and fouling in a pulverized coal-fired utility boiler. *United Engineering Foundation Conference on Heat Exchanger Fouling* 2001. Davos, Switzerland.
39. Bernstein, W., V. Hildebrand, and T. Holfeld. Modellierung der verbrennung und ihre validierung am originalbraunkohledampferzeuger eines 800 MW blokes. *VDI-Report* 1999; 1942: 45–55.
40. Walsh, P. M., A. N. Sayre, D. O. Loehden, L. S. Monroe, J. M. Beer, and A. F. Sarofim. Deposition of bituminous coal ash on an isolated heat exchanger tube: effects of coal properties on deposit growth. *Prog Energy Combust Science* 1990.

41. Lokare, Shrinivas Sadashiv. Mechanistic investigation of ash deposition in pulverized-coal and biomass combustion. 2008. Brigham Young University, PhD dissertation.
42. Costen, P. G., F. C. Lockwood, and M. M. Siddique. Mathematical modeling of ash deposition in pulverized fuel-fired combustors. *Proceedings of the Combustion Institute* 2000; 28(2): 2243-2250.
43. Senda, J., M. Kobayashi, S. Iwashita, and H. Fujimoto. Modeling of diesel spray impinging on flat wall. *JSME International Journal Series B Fluids and Thermal Engineering* 1996; 39(4): 859–866.
44. Chen, L., Sze Yong, and Ahmed F. Ghoniem. Modeling the slag behavior in three dimensional CFD simulation of a vertically oriented oxy-coal combustor. *Fuel Process Technology* 2013; 112: 106–117.
45. Baxter, L. L. Char fragmentation and fly ash formation during pulverized-coal combustion. *Combustion and Flame* 1992; 90: 174–184.
46. Syred, N., K. Kurniawan, T. Griffiths, T. Gralton, and R. Ray. Development of fragmentation models for solid fuel combustion and gasification as subroutines for inclusion in CFD codes. *Fuel* 2007; 86: 2221–2231.
47. Talbot, L., R. K. Cheng, R. W. Schefer, and D. R. Willis. *Journal of Fluid Mechanics* 1980; 101(4): 737–758.
48. Brock, J. R. On the theory of thermal forces acting on aerosol particles. *Journal of Colloid Interface Science* 1962; 17(1): 768–780.
49. Balakrishnan, S., R. Nagarajan, and K. Karthick. Mechanistic modeling, numerical simulation and validation of slag-layer growth in a coal-fired boiler. *Energy* 2015; 81: 462-470.

50. Wall, T. F., S. P. Bhattacharya, D. K. Zhang, R. P. Gupta, and X. He. The properties and thermal effects of ash deposits in coal fired furnaces. *Progression in Energy Combustions Science* 1993; 19: 487-504.
51. Krishnamoorthy, G., and Caitlyn Wolf. Assessing the role of particles in radiative heat transfer during oxy-combustion of coal and biomass blends. *Journal of Combustion* 2015; 2015: 1–15.
52. Wall, Terry, Yinghui Liu, Chris Spero, Liza Elliott, Sameer Chare, Renu Rathnam, Farida Zeenathal, Behdad Moghtaderi, Bart Buhre, Changdong Sheng, Raj Gupta, Toshihiko Yamada, Keiji Makino, and Jianglong Yu. An overview on oxyfuel coal combustion: state of the art research and technology development. *Chemical Engineering Research and Design* 2009; 87:1003-1016.
53. Yang, Xin, Alastair Clements, Janos Szuhanszki, Xiaohong Huang, Oscar Farias Moguel, Jia Li, Jon Gibbins, Zhaohui Liu, Chuguang Zheng, Derek Ingham, Lin Ma, Bill Nimmo, and Mohmaed Pourkashanian. Prediction of the radiative heat transfer in small and large scale oxy-coal furnaces. *Applied Energy* 2018; 211: 523-537.
54. Guo, Junjun, Zhaohui Liu, Peng Wang, Xiaohong Huang, Jing Li, Ping Xu, and Chuguang Zheng. Numerical investigation on oxy-combustion characteristics of a 200 MW tangentially fired boiler. *Fuel* 2015; 140: 660-668.
55. Al-Abbas, A. H., Naser J., and Dodds D. CFD modelling of air-fired and oxy-fuel combustion in a large-scale furnace at Loy Yang a brown coal power station. *Fuel* 2012; 102: 646–665.
56. Habermehl, M., J. Erfurth, D. Toporov, M. Förster, and R. Kneer. Experimental and numerical investigations on a swirl oxycoal flame. *Appl Therm Eng* 2012; 49: 161–169.

57. Black, S., J. Szuhánszki, A. Pranzitelli, L. Ma, P. J. Stanger, D. B. Ingham, and M. Pourkashanian. Effects of firing coal and biomass under oxy-fuel conditions in a power plant boiler using CFD modelling. *Fuel* 2013; 113: 780–786.
58. Yin, C., L. A. Rosendahl, and S. K. Kær. Chemistry and radiation in oxy-fuel combustion: a computational fluid dynamic modeling study. *Fuel* 2011; 90: 2519–2529.
59. Nikolopoulos, N., A. Nikolopoulos, E. Karampinis, P. Grammelisa, and E. Kakarasa. Numerical investigation of the oxy-fuel combustion in large scale boilers adopting the ECO-Scrub technology. *Fuel* 2011; 90: 198–214.
60. Gupta, R., S. Khare, T. Wall, C. Spero, K. Eriksson, D. Lundström, and J. Eriksson. Adaptation of gas emissivity models for CFD based radiative transfer in large air-fired and oxy-fired furnaces. *Proceedings of the 31st International Technical Conference on Coal Utilization & Fuel Systems 2006*. Sakkestad, B.A. (ed). (Coal Technology Association, Sheraton Sand Key, Clearwater, FL, USA).
61. Hottel, H. C., and A. F. Sarofim. *Radiative transfer*. New York: McGraw-Hill: 1967. p. 520. Print.
62. X, Li. Study on the radiation properties of non-isothermal or nonhomogeneous media in one dimensional oxy-fuel system. 2014. Huazhong, China. Huazhong University of Science Technology, PhD Dissertation.
63. Smith, T. F., Z. F. Shen, and J. N. Friedman. Evaluation of coefficients for the weighted sum of gray gases model. *Journal of Heat Transfer* 1982; 104: 602–608.
64. Yin, C., Lars C. R. Johansen, L. A. Rosendahl, and S. K. Kær. New weighted sum of gray gases model applicable to computational fluid dynamics (CFD) modeling of oxy-fuel

- combustion: derivation, validation, and implementation. *Energy Fuels* 2010; 24: 6275–6282.
65. Shaw, D. W., X. Zhu, M. K. Misra, and R. H. Essenhigh. Determination of global kinetics of coal volatiles combustion. *Symposium (International) on Combustion* 1991; 23(1): 1155–1162.
66. Dryer, F. L., and I. Glassman. High-temperature oxidation of CO and CH₄. *Symposium (International) on Combustion* 1973; 14(1): 987–1003.
67. Andersen, J., C. L. Rasmussen, T. Giselsson, and P. Glarborg. Global combustion mechanisms for use in CFD modeling under oxy-fuel conditions. *Energy Fuels* 2009; 23: 1379–1389.
68. Kurose, R., H. Makino, and A. Suzuki. Numerical analysis of pulverized coal combustion characteristics using advanced low-NO_x burner. *Fuel* 2004; 83: 693–703.
69. Smoot, L. A decade of combustion research. *Prog Energy Combust Science* 1997; 23: 202–232.
70. Nakod, P., G. Krishnamoorthy, M. Sami, and S. Orsino. A comparative evaluation of gray and non-gray radiation modeling strategies in oxy-coal combustion simulations. *Appl Therm Eng* 2013; 54: 422–432.
71. Hu, Yukun, and Jinyue Yan. Numerical simulation of radiation intensity of oxy-coal combustion with flue gas recirculation. *International Journal of Greenhouse Gas Control*, 2013; 17: 473–480.
72. Edge, P., S. R. Gubba, L. Ma, R. Porter, M. Pourkashanian, and A. Williams. LES modelling of air and oxy-fuel pulverized coal combustion - impact on flame properties. *Proceedings of the Combustion Institute* 2011; 33: 2709-2716.

73. Clements, A. G. Modelling mercury oxidation and radiative heat transfer in oxy-coal environments. 2016. University of Leeds, Doctoral Thesis.
74. Johansson, Robert, Bo Leckner, Klas Andersson, and Filip Johnsson. Influence of particle and gas radiation in oxy-fuel combustion. *International Journal of Heat and Mass Transfer* 2013; 65: 143-152.
75. Hottel, H. C., J. J. Noble, A. F. Sarofim, D. W. Green, and R. H. Perry. *Perry's chemical engineers' handbook*. New York: McGraw-Hill; 2007. 8th ed. Print
76. Krishnamoorthy, G., M. Sami, S. Orsino, A. Perera, M. Shahnam, and E. D. Huckaby. Radiation modeling in oxy-fuel combustion scenarios. *International Journal of Computational Fluid Dynamics* 2010; 24: 69–82.
77. Krishnamoorthy, G. A new weighted-sum-of-gray gases model for CO₂–H₂O gas mixtures. *International Journal of Energy Research* 2010; 37: 1182–1186.
78. ANSYS, Inc. *ANSYS Fluent Theory Guide*. Release 19.1, 2018. Online Manual Resource.
79. Krishnamoorthy, G. A new weighted-sum-of-gray-gases model for oxy-combustion scenarios. *International Journal of Energy Research* 2013; 37(14): 1752–1763.
80. Modest, M. F. *Radiative heat transfer*. Oxford, UK: Academic Press; 2013. Print.
81. Zhang, J., T. Ito, S. Ito, D. Riechelmann, and T. Fujimori. Numerical investigation of oxy-coal combustion in a largescale furnace: non-gray effect of gas and role of particle radiation. *Fuel* 2015; 139: 87–93.
82. Kuehlert, K. *Modellbildung und Berechnung der Wärmestrahlung in Gas-und Kohlenstaubfeuerungen*. 1998. Aachen, Germany. RWTH Aachen University, PhD Thesis.
83. Menguc, M. P., S. Manickavasagam, and D. A. D'sa. Determination of radiative properties of pulverized coal particles from experiments. *Fuel* 1994; 73(4): 613–625.

84. Smoot, D., and P. Smith. Coal combustion and gasification. New York: Springer US; 1985. Print.
85. Syamlal, M. MFIX documentation: Numerical technique. National Energy Technology Laboratory, U.S. Dept. of Energy, Technical Note No. DOE/MC31346-5824 (1998).
86. ANSYS, Inc. *ANSYS Fluent User Guide*. Release 19.1, 2018. Online Manual Resource.
87. Balachandar, S., and John K. Eaton. Turbulent dispersed multiphase flow. *Annual Review of Fluid Mechanics* 2010; 42: 111–133.
88. Li, Z. Q., F. Wei, and Y. Jin. Numerical simulation of pulverized coal combustion and NO formation. *Chemical Engineering Science* 2003; 58: 5161–5171.
89. Zhou, L. X. A multifluid model of two-phase flows with pulverized-coal combustion. *Coal Combustion* 1988; New York: Hemisphere Publishing: 207–213.
90. Guo, Y., W. Lin, and L. Zhou. Simulation of pulverized coal combustion using a pure two-fluid model. *Journal of Engineering Thermal Physics* 1998; 19(1): 117–120. *In Chinese*.
91. Zhang, Jingwei. Oxy-coal combustion: stability of coaxial pulverized coal flames in O₂/CO₂ environments. 2010. University of Utah, PhD Dissertation.
92. Azuhata, S., K. Narato, H. Kobayashi, N. Arashi, S. Morita, and T. Masai. A study of gas composition profiles for low NO_x pulverized coal combustion and burner scale-up. *Symposium (International) on Combustion* 1988; 21(1): 1199–1206.
93. Pedel, J., J. N. Thornock, and P. J. Smith. Ignition of co-axial turbulent diffusion oxy-coal jet flames: experiments and simulations collaboration. *Combustion and Flame* 2013; 160(6): 1112–1128.

94. Zhang, Jingwei, K. Kelly, E. Eddings, Jost O. L. Wendt. Ignition in 40 kW co-axial turbulent diffusion oxy-coal jet flames. Proceedings of the Combustion Institute 2011; 33(2): 3375–3382.
95. Goshayeshi, Babak, and James C. Sutherland. Prediction of oxy-coal flame stand-off using high-fidelity thermochemical models and the one-dimensional turbulence model. Proceedings of the Combustion Institute 2015; 35(3): 2829–2837.
96. Jovanovic, Rastko, A. Milewska, B. Swiatkowski, A. Goanta, and H. Spliethoff. Sensitivity analysis of different devolatilisation models on predicting ignition point position during pulverized coal combustion in O₂/N₂ and O₂/CO₂ Atmospheres. Fuel 2012; 101: 23–37.
97. Badzioch, S., and P. G. W. Hawksley. Kinetics of thermal decomposition of pulverized coal particles. Industrial & Engineering Chemistry Process Design and Development 1970; 9(4): 521–530.
98. DeSai, P.R., and C. Y. Wen. Computer modeling of the Morgantown Energy Research Center's fixed bed gasifier [theory and development]. 1978. West Virginia University.
99. Borman, G. L., and K. W. Ragland. Combustion engineering. New York: McGraw-Hill; 1998. p. 120–122. Print.
100. Jones, W. P., and R. P. Lindstedt. Global reaction schemes for hydrocarbon combustion. Combust and Flame 1998; 73(3): 233–249.
101. Rezaei, Dadmehr. Co-axial turbulent diffusion flames with directed oxygen injection. 2013. The University of Utah.
102. Krishnamoorthy, G. A comparison of gray and non-gray modeling approaches to radiative transfer in pool fire simulations. Journal of Hazardous Materials 2010; 182(1-3): 570-580.

103. Linak, W. P., C. A. Miller, W. S. Seames, J. O. L. Wendt, T. Ishinamori, Y. Endo, and S. Miyamae. On trimodal particle distributions in fly ash from pulverized coal combustion. Proceedings Combustion Institute 2002; 29: 441-447.